RHODES UNIVERSITY

THIRD GENERATION CALIBRATIONS FOR MEERKAT OBSERVATION OF SARASWATI SUPERCLUSTER

by

Robert Kincaid

Submitted in fulfillment of the
academic requirements for the degree of
Masters
in
Physics
Rhodes University, Grahamstown

Supervised by Prof. O. M. Smirnov & Dr Viral Parekh

June 28, 2022

If you don't find the time, if you don't do the work, you don't get the results.

-ARNOLD SCHWARZENEGGER

Declaration of Non-Plagiarism

I, **Robert Kincaid**, declare that:

1. The research reported in this thesis, except where otherwise indicated, is my original research.
2. This thesis has not been submitted for any degree or examination at any other university.
3. This thesis does not contain other persons' data, pictures, graphs or other information unless specifically acknowledged as being sourced from other persons.
4. This thesis does not contain other persons' writing unless specifically acknowledged as being sourced from other researchers. Where other written sources have been quoted, then:
    (a) Their words have been re-written but the general information attributed to them has been referenced.
    (b) Where their exact words have been used, then their writing has been placed in italics and inside quotation marks, and referenced.
5. This thesis does not contain text, graphics or tables copied and pasted from the Internet, unless specifically acknowledged, and the source being detailed in the thesis and in the references sections.

Signed:

Date:

Preface

The international collaboration of the Square Kilometre Array (SKA), which is one of the largest and most challenging science projects of the 21st century, will bring a revolution in radio astronomy in terms of sensitivity and resolution. The recent launch of several new radio instruments, combined with the subsequent developments in calibration and imaging techniques, has dramatically advanced this field over the past few years, thus enhancing our knowledge of the radio universe. Various SKA pathfinders around the world have been developed (and more are planned for construction) that have laid down a firm foundation for the SKA in terms of science while additionally giving insight into the technological requirements required for the projected data outputs to become manageable. South Africa has recently built the new MeerKAT telescope, which is a SKA precursor forming an integral part of SKA-mid component. The MeerKAT instrument has unprecedented sensitivity that can cater for the required science goals of the current and future SKA era. It is noticeable from MeerKAT and other precursors that the data produced by these instruments are significantly challenging to calibrate and image. Calibration-related artefacts intrinsic to bright sources are of major concern since, they limit the Dynamic Range (DR) and image fidelity of the resulting images and cause flux suppression of extended sources. Diffuse radio sources from galaxy clusters in the form of halos, relics and most recently bridges on the Mpc scale, because of their diffuse nature combined with wide field of view (FoV) observations, make them particularly good candidates for testing the different approaches of calibration.

Abstract

Galaxy clusters are ideal tracers of the large-scale matter distribution in the universe formed as a result of violent processes involving accretion and merging of smaller structures into larger ones. During these merging events, complex interactions involving their multiple-component composition give rise to a variety of multi-wavelength sources. Pilot observations of the core of the *Saraswati* supercluster have been conducted with MeerKAT L-band in order to image the two massive galaxy clusters residing at the centre, namely ZwCl 2341+0000 (hereafter ZwCl 2341) and Abell 2631 (hereafter A2631). In this thesis, firstly, we apply modern third-generation calibration (3GC) techniques implemented by the `CubiCal` and `killMS` software packages to our new MeerKAT L-band observations. We show a significant reduction in the artefacts produced from a select number of bright sources in both clusters. We then quantify these improvements using a few standard statistical parameters. We see clear decreasing trends of root mean square (RMS), maximum pixel values (MAX), mean absolute deviation (MAD) and sum of negative components (SUM NEG) and increasing trends of DR in the direction-dependant (DD) generated `CubiCal` and `killMS` images. Secondly, we use these DD corrected MeerKAT images, combined with our new (DI calibrated) uGMRT data to explore the radio properties of the diffuse sources residing in ZwCl 2341 and plot their 1D spectra. Our MeerKAT and uGMRT data of ZwCl 2341 have revealed diffuse double relics, consistent with previous observations and a potential halo or bridge residing between the relics. Our new MeerKAT observation had the best sensitivity when compared to previous observations of ZwCl 2341 which was able to disentangle the potential diffuse halo or bridge from the relics after tapering, albeit at the 2σ level. We then plot 1D spectra and find that the double relics both exhibit flat spectra with the north relic (NR) ($\alpha_{NR} = -0.70$) slightly flatter than the south relic (SR) ($\alpha_{SR} = -0.88$). We find an unusually flat spectrum for the potential halo or bridge source ($\alpha = -0.33$), which is an anomaly compared to the spectra of other halos reported in the literature. In our observation, it is revealing a large size, complex morphology, unusually flat spectrum, however, its true nature is still unknown. Lastly, we combine our new radio observations with previous X-ray and optical observations to deduce more about the complex merging scenario of ZwCl 2341 and discuss how these independent analyses support the double relic and halo or bridge model suspected to be in ZwCl.

Acknowledgments

Firstly, I would like to thank the Radio Astronomy Techniques and Technologies (RATT) group and Prof Oleg Smirnov for initially allowing me the opportunity to be part of the Radio Astronomy group here at Rhodes University in 2019. I also thank the adequate funding and generous equipment grant I received from the NRF during these past two years which have made it possible for me to comfortably conduct my studies and eventually finish my masters.

The RATT group is a close-knit community consisting of bright and friendly academics and students. I am grateful to have met these people with whom I've got to know better through the busy weeks and weekly Thursday meetings. They have always been very helpful regarding any questions I may have had and have all played a small part in either directly or indirectly contributing to this thesis.

Secondly, I would like to thank my supervisor, Dr Viral Parekh and again, Prof Oleg Smirnov. I thank Viral for his flexibility throughout my masters and his continuous support through answering my every Gmail chat question and setting up Zoom meetings no matter the time of day. Your patience and understanding throughout my masters is appreciated. I also thank him for the useful comments received throughout the writing of my thesis, ensuring that I submit the best possible version. I also thank Oleg for his quick comments regarding my thesis and for always being there when I was in doubt. Your ability to manage a group like RATT and still contribute significantly to the science community is a skill to be admired.

Thirdly, I must thank Prof Liu and Teacher Zang from the Chinese Department at Rhodes for always making me feel welcome whenever I visit, and answering my every question. Teacher Zang is a gifted teacher and I and many of her students have learnt alot from her in the past two years. I also thank Prof Liu for the interesting conversations and his general useful advice.

Lastly, I would like to thank my friends Charles, Koketso, Eric, Karl, Sihle, Lwando, Tlaba and many others from room 47 in the Physics department for making the office a fun and productive working environment. I thank my family for their continuous support. They have played a big role in my success here at Rhodes University as well as the completion of this year.

List of Tables

List of Figures

Contents

Chapter 1

Introduction

1.1 Large scale structure of the Universe

The currently accepted model of cosmology, the **(ΛCDM)** cosmology, tells us that the Universe, on the largest scales, forms an intricate non-uniform pattern of interconnected sheet-like filaments surrounded by large near-empty voids (Bond et al., 1996; Aragón-Calvo et al., 2007). This filamentary sheet-like structure is known as the 'cosmic web' or large scale structure (LSS) of the Universe. The cosmic web is postulated to have been formed due to the interplay of dark matter and dark energy with gravity in the early Universe. The filaments are interconnected thread-like components of enhanced density consisting of dense clusters at the intersection points of these filaments, called nodes. These filaments form the individual strings of the cosmic web and constitute the majority of the mass component. Vast regions of empty space called voids are also abundant within the filamentary structure and make up most of the volume component. We show the main components comprising the cosmic web structure on the left of Figure 1.1 including filaments, nodes and voids. The thread-like filaments can clearly be seen connecting the central nodes. The right panel of Figure 1.1, both top and bottom, show simulation snapshots for the evolution of zoomed-in regions of the cosmic web. The subimages (labelled (c)) show the end of the simulation representing the current time.

The LSS initially grew from small density inhomogeneities of the primordial field due to quantum perturbations in the early Universe (Lang & Lang, 2013). These were then amplified immensely by inflation at a later time; the nature of dark matter (majority mass component) coupled with inflation allowed for the clumping of the former into what are known as dark matter halos (Sparke & Gallagher III, 2007). These formed potential wells in which baryons could later fall into to form structures. The Universe started to cool and larger structures formed through hierarchical merging, smaller structures formed first and successively larger ones formed later. The small density inhomogeneities are therefore believed to be the seeds responsible for all structures seen today (Calzetta & Hu, 1995). Today, our Universe consists of an abundance of structures, ranging from stars, galaxies, clusters of galaxies, superclusters, voids, and massive sheet-like structures comprised of galaxies (Peebles, 1980).

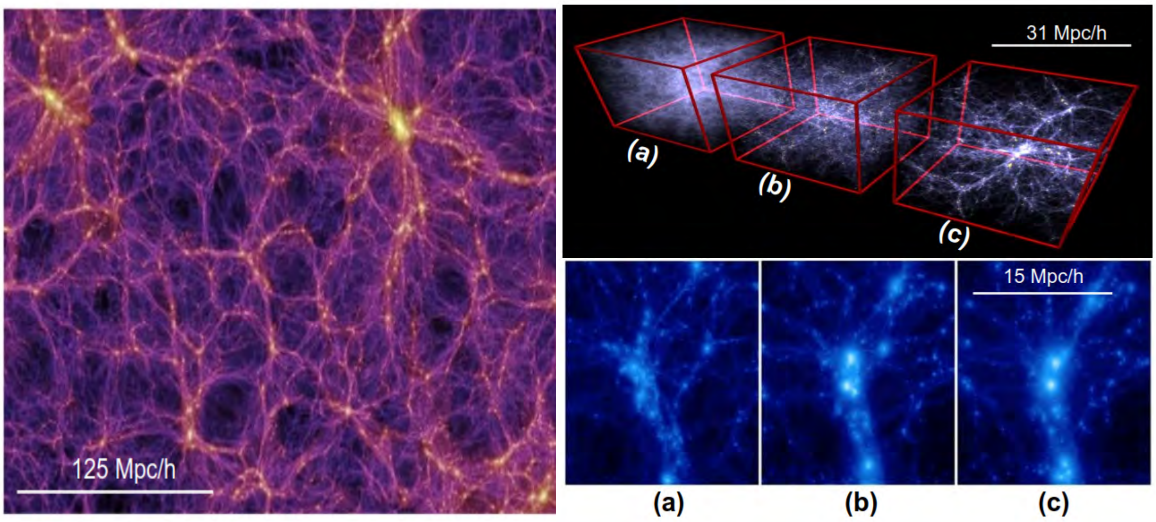

Figure 1.1: The cosmic web and its evolution on different size scales. *Left*: Simulation of a large portion of the cosmic web. Filaments are woven like threads throughout dense walls comprising of cluster of galaxies. The densest regions are shown in bright yellow and the voids in the darker black regions. *Right*: The top diagram shows simulation snap shots of a small volume region of the cosmic web depicting evolution for the formation of the LSS at various redshifts z (from (a)-(c): $z = 6, z = 2$ and $z = 0$) (Springel et al., 2005). The bottom diagram shows similar simulation snap shots as the top, but for the evolution of a node of the cosmic web. It shows the merging of two galaxy clusters (seen clearly as two bright circular structures at the centre of (b) and (c)) at various z (from (a)-(c): $z = 1, z = 0.34$ and $z = 0.07$). These clusters have travelled along the filaments and are merging at the node (Brüggen et al., 2021).

1.1.1 Superclusters

Superclusters are the largest concentrations of matter in the Universe formed at the largest intersection points (large bright yellow regions in Figure 1.1) of the filaments making up the cosmic web. They are the largest constituents of the cosmic web and surround the large less dense voids, forming the 'cellular-type' morphology attributed to the cosmic web. Superclusters can be thought of as being clusters of rich clusters and are generally defined as groups of two or more galaxy clusters above a given spatial density enhancement (Bahcall, 1988). They appear as irregular, flat and non-spherically symmetric objects consisting of high-density systems of galaxies and diffuse gas elongated in a direction along the constituent filaments, extending to lengths of ∼ tens of Megaparsecs (Mpc) (Bahcall, 1999). They have no clear well-defined boundary or central concentration. These properties are expected to be a clear sign that they, to a large extent, reflect the initial conditions set in the early Universe for LSS. Superclusters are too large to be in a gravitationally bounded state and, overall, are in a dynamically younger state, expanding with the Universe as compared to the substructures which they host (Fabian, 2012).

1.1.2 Galaxy clusters

Clusters of galaxies are the most prominent substructures in superclusters that are in a gravitationally bounded state (held together by the clusters self-gravity) and, at their centres, have achieved virial equilibrium (Sparke & Gallagher III, 2007). Galaxy clusters are formed at the nodes of filaments leading to the larger nodes (small bright yellow regions in Figure 1.1). They are small enough (as compared to superclusters) to have achieved dynamical equilibrium during the age of the Universe and large enough to confine a representative fraction of the mass in the Universe (Sarazin, 2003). They are formed through the energetic merging of smaller cluster substructures such as galaxies and groups of galaxies. Clusters of galaxies are complex systems that contain several different thermal and non-thermal components and extend over $\sim 2-4$ Mpc with masses of the order of $\sim 10^{14} - 10^{15}$ $M_\odot$; with a large portion of the mass ($\sim 70\%$) being that of invisible dark matter (Cassano, 2009). The thermal components make up most of the remaining mass and include individual galaxies (∼ 10%) and a hot ionised intracluster medium (ICM) (∼ 15 – 20%) gas (Sarazin, 2002). The existence of these components is evident through X-ray thermal bremsstrahlung emission (Felten et al., 1966). Non-thermal components present inside galaxy clusters include weak (∼ nG) permeating magnetic fields and relativistic electrons. These are evident from the existence of diffuse large-scale synchrotron radio emission associated with an increasing number of clusters (e.g. Feretti et al. 2012; van Weeren et al. 2019). Cosmological conclusions on the relative amounts of visible, dark-baryonic and non-baryonic matter in galaxy clusters can be probed through the study of their dynamical properties and radiation content (e.g. White & Fabian 1995). They also allow us to understand how material flows and interacts with the filament and are ideal laboratories to study the process of LSS formation and evolution. We have shown on the left of Figure 1.2 the location and environment in which galaxy clusters reside. On the right of Figure 1.2, we show a composite image of the well-studied merging galaxy cluster termed the 'Bullet cluster', which is considered to be one of the most spectacular dark-matter interactions currently known in the Universe.

1.1.3 Merging clusters

Cluster mergers are the mechanism by which galaxy clusters are originally assembled (Sarazin, 2002). At the nodes of filament of the cosmic web, gravitational attraction causes smaller cluster units such as galaxy groups to aggregate towards larger units such as galaxy clusters. The merging events consist of at least two subclusters of equal or unequal mass colliding at supersonic speeds, releasing tremendous amounts of gravitational binding energy of the order of $\sim 10^{64}$ ergs on Gyr timescales. This potential energy gets converted into kinetic energy in the form of shocks, turbulence, which in turn heats and re-accelerates cosmic ray (CR) particles and powers the amplification of magnetic fields through merger induced magnetohydrodynamics (MHD) of the ICM (Blandford & Eichler, 1987; Roettiger et al., 1999b; Brunetti et al., 2001). It has been found that most clusters containing non-thermal emission all contain traces of recent dynamical activity (Edge et al., 1992; Watt et al., 1992; van Weeren et al., 2019) . Their multi-wavelength images

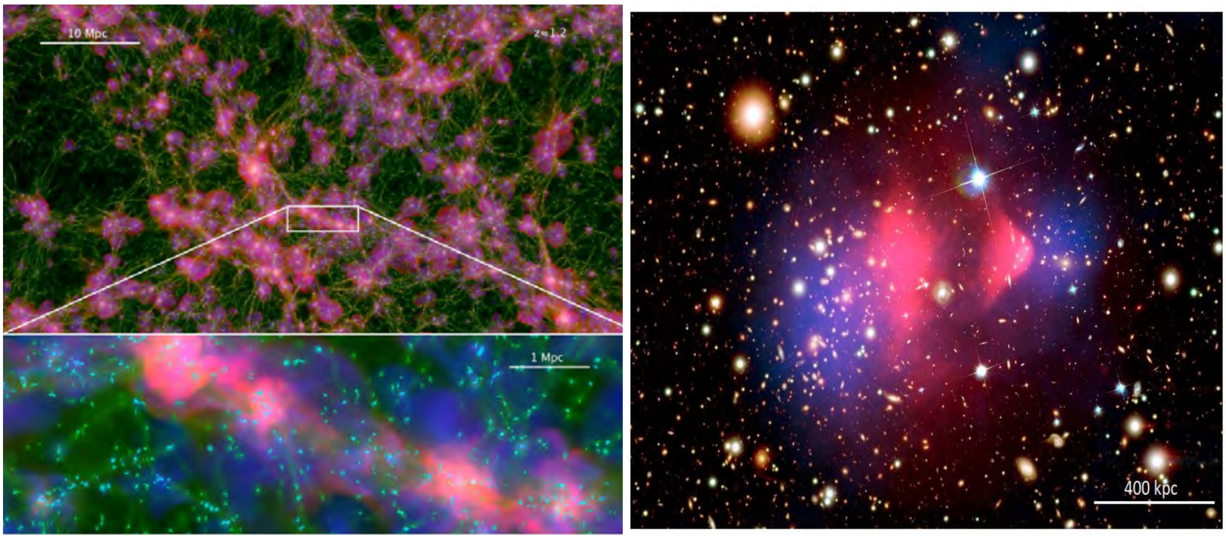

Figure 1.2: Galaxy clusters and their place in the cosmic web. *Left*: Top image shows a region of the cosmic web showing the location of a galaxy cluster within the filaments. Each galaxy cluster is made up of hundreds to thousands of galaxies. From the image spatial scale, we see that each yellow dot is a galaxy (normal matter), while the purple regions represent clustering (mostly dark matter). The bottom image shows a magnified region enclosed by the white rectangle in the top image. It shows the environment associated with galaxy clusters. A trail of hot ionised ICM plasma permeates the cluster. The ICM temperature, density and metalicity are indicated in red, green and blue, respectively (Markevitch, 2005). *Right*: A composite image composed of optical data (yellow light) and X-ray data (pink) combined with a reconstructed mass map (blue) from gravitational lensing of the famous 1E 065756 merging galaxy cluster, often referred to as the 'Bullet cluster'. The mass component (blue) traces the optical light on either side and not the X-ray emitting gas at the centre, indicating the existence of dark matter during the interaction (Clowe et al., 2007)

show evidence of disturbed morphology, strong temperature variations and lack of cooling flows (Discussed in §1.2.1). These properties provide indications of the existence of various energetic event(s) that must have taken place some time in the cluster's history. From the magnitude of energy required to create these features, the only possible explanation is that of cluster mergers since they are the only mechanism known to be violent enough to create a disturbance of this magnitude.

1.1.4 Merger shocks

During initial contact of two subclusters, a shock front is formed as a result of the large gradient in the internal properties of the environment between the two subcluster units. This shock front transports energy and propagates it in the direction of the smaller mass subcluster. Shocks are irreversible processes that increase the entropy of the region preceding the shock as the gas is compressed (Sarazin, 2002). Particle acceleration occurs as the shock wave moves through the cluster. This shock acceleration is of a first-order Fermi nature (Bednarz & Ostrowski, 1996). Acceleration occurs diffusely; particles scatter back and forth across the shock, gaining at each crossing and recrossing an amount of energy. The acceleration efficiency is determined by the shock Mach number $\mathcal{M}$ used to quantify the power of the shock, defined by:

$$\mathcal{M} \equiv \frac{v_s}{c_s}, \tag{1.1}$$

where $c_s = \sqrt{(5/3)P/\rho}$ is the sound speed (or thermal speed) in the pre-shocked gas and v_s is velocity of a shock wave relative to the pre-shocked gas. Typical cluster mergers have $\mathcal{M} \leq 3$ (e.g. van Weeren et al. 2019). $\mathcal{M}$ can also be found from radio observations based on the assumption of the Diffusive Shock Acceleration (DSA) theory (Discussed in §1.2.2.2). in the form of the radio injection spectral index α_{inj}:

$$\mathcal{M}_{\mathrm{radio}} = \sqrt{\frac{2\alpha_{\mathrm{inj}} - 3}{2\alpha_{\mathrm{inj}} + 1}}\ . \tag{1.2}$$

Where α_{inj} is the injection index describing the initial distribution of the electron population and related to the integrated spectral index as: $\alpha_{int} = 0.5 + \alpha_{inj}$ (Kardashev, 1962).

An independent measure of the property of shocks can also be probed through deep X-ray observations by measurement of temperature T, pressure p or density ρ jumps at the location of the shock (ZuHone & Su, 2022). The standard Rankine-Hugoniot jump conditions (Landau & Lifshitz, 1959) are a set of equations relating these properties between the shocked and pre-shocked regions of the shock front:

$$\begin{aligned} \frac{\rho_1}{\rho_2} &= \frac{\gamma+1}{\gamma-1+2\mathcal{M}^2} \\ \frac{p_2}{p_1} &= \frac{2\gamma\mathcal{M}^2+(1-\gamma)}{\gamma+1} \\ \frac{T_2}{T_1} &= \frac{2\gamma\mathcal{M}^2+(1-\gamma)}{\gamma+1}\ . \end{aligned} \tag{1.3}$$

Where subscript 1 and 2 denote the pre-shocked and shocked regions, respectively. Γ is the adiabatic index. This takes the form of an ideal gas $\Gamma = 5/3$ for a fully ionised plasma, which is often an assumed condition in the ICM. Several independent cosmological models have identified two main types of shocks, namely (Bykov et al., 2008):

- internal or merging shocks due to infall and merging of smaller substructures such as galaxy groups or clusters that give rise to moderate $\mathcal{M}$ numbers of $2 \leq \mathcal{M} \leq 4$; and
- external or accretion shocks resulting from accretion of cold gas along filaments onto gravitationally attracting nodes, characterised by high $\mathcal{M}$.

External shocks are formed on much larger scales than merger shocks. Internal shocks are postulated to be the most important source of energy dissipation in clusters providing significant ICM heating (Ryu et al., 2003). This makes make them likely candidates to be the sources of non-thermal emission in clusters of galaxies (Bykov et al., 2000).

1.2 Emission in galaxy clusters

Diffuse radio emission from galaxy clusters are tracers of the shocks and turbulence in the ICM induced by the cluster merging process. The MHD turbulence that forms as a result re-accelerates pre-existing electrons to relativistic speeds inside the cluster. This relativistic property, combined with the charged nature of these thermal electrons co-existing with non-thermal components such as a magnetic fields, produces unique cluster-wide diffuse radio sources attributed to galaxy clusters. Interpretation of their X-ray morphology, radio properties and spectra can give us vital information on the origin and evolution of these sources.

1.2.1 X-ray

The hot plasma of the diffuse ICM gas is detected through the luminous X-ray emission produced by bremsstrahlung radiation. This hot intracluster gas has a typical temperature of $\sim$ 5 keV, central gas density of $\sim 10^{-3}$ electrons cm^{-3} and the resultant emission has an X-ray luminosity of $L_x \sim 10^{44}$ erg s^{-1} (Bahcall, 1996). This emission is a result of the deceleration of high-speed electrons from the force produced due to the interaction of oppositely charged ions (protons) with electrons. As they decelerate, energy in the form of photons (mainly visible in X-ray) is continuously emitted (Sarazin, 1986). This thermal bremsstrahlung radiation process is the primary mechanism resulting in X-ray emission in clusters.

X-ray observations of the cluster ICM provide information on cluster size, morphology, dynamical state and thermal radiation mechanisms. X-ray observations of shocks can directly measure the temperature and density jumps in merger shocks (see Equation 1.4) and can be used to determine the geometry and kinematics of the merger and estimate cluster mass (Evrard et al., 1995). A significant fraction of galaxy clusters show a trend of rapid increase in surface brightness towards the centre in their X-ray surface brightness maps. This is accompanied by steep gradients in density and temperature distributions towards these central regions. The resulting gas, therefore, has lower cooling times than the surrounding gas and contain cooler gas. Galaxy clusters containing these features are termed cool cores (Fabian, 1994). Mergers are known to disrupt cool cores; during the merging event, the ICM that belongs to each subcluster is mixed and shows a disturbed X-ray morphology with significant substructure. Their corresponding X-ray observations display a variety of irregular structures, such as multiple X-ray peaks, sharp X-ray surface brightness discontinuities (termed cold fronts) and strong temperature variations as well as complex gas temperature distributions (Markevitch, 2012). The best known example of merger shock from X-ray observation is the one in the so-called ‘Bullet Cluster’ (Markevitch et al., 2002; Markevitch & Wilson, 2006), which we have shown a composite image of in Figure 1.2. In Figure 1.3, we show its Chandra X-ray surface brightness image, which displays a disturbed X-ray morphology resulting from the merging of two subclusters flying apart after collision. The Bullet cluster hosts several types of diffuse emission (not shown in Figures 1.2 and 1.3). These types of radio sources are common in disturbed X-ray maps and we discuss three classes in the next subsection.

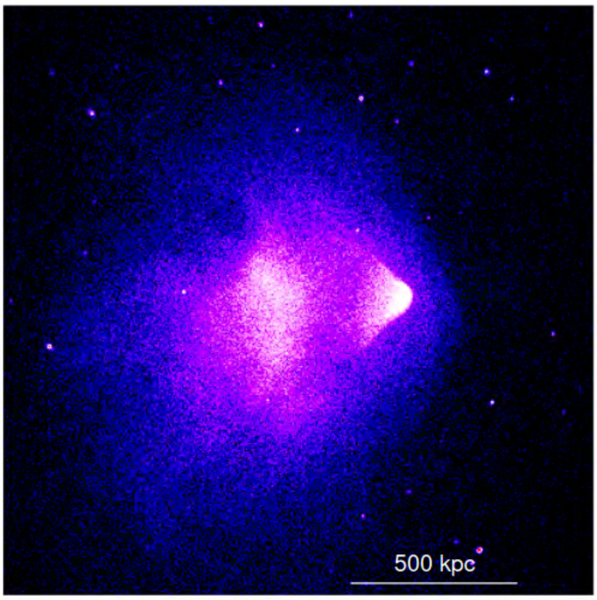

Figure 1.3: Chandra X-ray colour image of the famous ‘Bullet cluster’ or 1E 0657–56. The Chandra surface brightness map is shown in the energy band 0.8 – 4 keV. The spatial scale is shown by the horizontal line at the bottom right. The ‘bullet-like’ structure can be seen exiting the core heading West. The brightest edge around the ‘bullet’ is a shock front. (Markevitch, 2012).

1.2.2 Radio

Several galaxy clusters are known to contain large-scale cluster-wide diffuse radio sources which have no obvious connection to any single active galaxy, but rather the cluster ICM (e.g. Jaffe & Rudnick 1979, Giovannini et al. 1993, Giovannini et al. 1999, Feretti et al. 2001; Ferrari et al. 2008; Feretti et al. 2012). This emission manifests itself through the presence of ($\sim$ GeV) relativistic electrons and weak ($\sim \mu$ G) magnetic fields in the ICM, together with the hot thermal plasma emitting X-rays. They mainly fall into two broad categories: radio halos and relics (e.g. van Weeren et al. (2019) for observational review, and Brunetti & Jones (2014) for a theoretical review) and recently radio ridge (Govoni et al., 2019). These sources are characterised as diffuse, large ($\sim$ 1 Mpc), non-thermal, low surface brightness ($\sim \mu$Jy/arcsec^2) sources with steep spectra ($S_\nu \propto \nu^{-\alpha}$, $-0.7 > \alpha > -1.4$). These diffuse radio sources are mostly found in (but not all) non-relaxed/merging galaxy clusters (Cassano et al., 2010; Parekh et al., 2015) and therefore provide critical information for understanding the merging process. The origin to these diffuse sources is still not fully understood. The combination of relatively short electron radiative times due to synchrotron and inverse Compton (IC) processes (e.g. Jaffe & Rudnick 1979), together with the Mpc scale nature of the emission, implies the need for an in-situ re-acceleration. The proposed re-acceleration mechanism is that of merger shock for relics and turbulence for halos, which are both induced by cluster mergers. Due to the absence of these diffuse sources in many merging clusters, these current proposed formation mechanisms may only represent one component in their formation scenario. Additional factors including availability of magnetic fields, sufficient pool of mildly relativistic CR particles at cluster outskirts (for relics) and cluster-wide volume (for halos) are expected to be available during the merging process to fully explain the existence of these diffuse sources.

1.2.2.1 Halos

Radio halos are large, unpolarised, low surface brightness sources permeating the central Mpc^3 region of galaxy clusters. They display a regular concentric-like geometry (similar to that of the roundish X-ray emission from the thermal ICM) and result from turbulent ICM interaction with magnetic fields (Botteon et al., 2019). Their brightness distribution approximately follows the distribution of the thermal ICM (Markevitch & Vikhlinin, 2001). Their emission is a direct manifestation of the re-accelerated fossil relativistic electrons from the turbulence induced by the cluster merging process. Radio halos found in massive ($\sim 10^{15}$ $M_{\odot}$) and powerful ($L_X \geq 5 \times 10^{44}$ ergs^{-1}) merging clusters at high frequencies (~ GHz) are relatively rare, with about 30% present in these types of clusters (Feretti et al., 2012). By considering the power-law nature of the emitting electrons ($S_\nu \propto \nu^{-\alpha}$) and the steep-spectra property attributed to halos, it can be seen that halo flux extrapolation to high frequencies results in fainter fluxes with an eventual cut-off at > GHz frequencies in the expected spectra of halos (Cassano, 2009). Radio halos, are therefore, more difficult to observe at high frequencies as compared to lower frequencies. Since they appear more luminous at lower frequencies, low-frequency observations have the capability to observe halos associated with less energetic cluster merger events.

The formation of radio halos has been postulated by considering two models, the primary (re-acceleration) electron model and the secondary electron model (or hadronic model). These models attempt to explain radio halo formation by providing solutions to the short radiative electron time problem of the emitting electrons (Brunetti et al., 2012). The primary electron model proposes that electrons are continuously injected into the cluster volume by processes involving AGN of active galaxies or star formation mechanisms. Cluster merging events and/or the previously mentioned processes then supply energy in the form of MHD turbulence which can re-accelerate pre-existing electrons (Brunetti et al., 2001; Petrosian, 2001). The secondary electron model assumes that because protons are abundant within the cluster volume, relativistic electrons can be produced (called secondary electrons) by proton-to-proton collisions from existing relativistic protons (Dennison, 1980; Blasi & Colafrancesco, 1999; Enßlin et al., 2011). However, it has recently been suggested that, non-thermal diffuse emissions from clusters in the form of halos are, in reality, a combination of these two models, comprised of both thermal and non-thermal components; a mixed population of relativistic particles (protons, secondary and primary electrons/positrons) coexisting together in the ICM with turbulent magnetic fields and thermal particles that give rise to these structures (Cassano, 2009). A well-known example of a radio halo is ‘Coma C’ of the Coma cluster (Giovannini et al., 1993; Thierbach et al., 2003; Brown & Rudnick, 2011; Bonafede et al., 2021), which is regarded as a prototype of a cluster–wide radio halo. We shown in Figure 1.4 the giant radio halo found in MACSJ0018.5+1626.

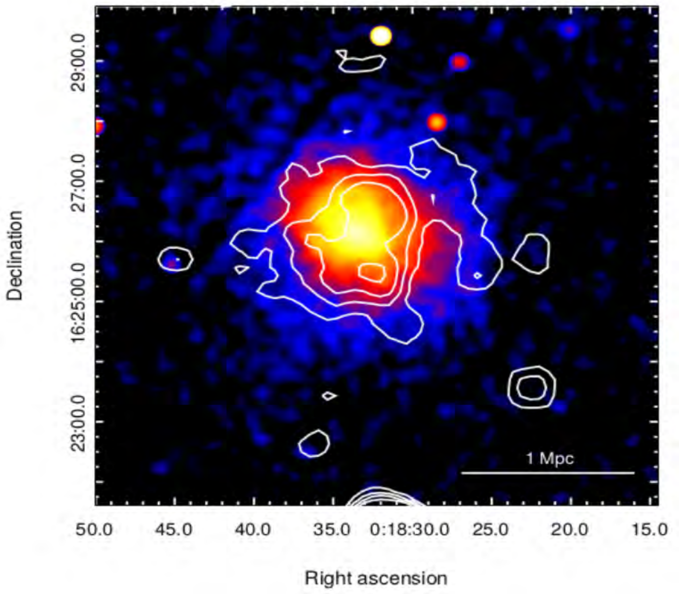

Figure 1.4: Radio emission from the giant radio halo at the centre of MACSJ0018.5+1626 shown in white contours, superimposed on the X-ray colour image obtained by Chandra. The contour levels are spaced as: $[6, 10, 14, 20] \times 1\sigma_{\rm rms}$ where $1\sigma_{\rm rms} = 0.05$ mJy per beam. The beam size is $40'' \times 40''$. The spatial scale shown by the horizontal white line at the bottom right (Giovannini et al., 2020).

1.2.2.2 Relics

Relics are similar to halos in terms of low surface brightness, large size, luminosity, no optical counter-part and a steep spectrum. They are, however, situated outside the hot X-ray ICM at the cluster peripheral regions, exhibit irregular morphologies, have an elongated shape (e.g. Ferrari et al. 2008; Feretti et al. 2012) and are strongly polarised (~ 30%) at frequencies of ~ 1GHz (Ensslin et al., 1997). They occur in isolation or in pairs around galaxy clusters. Pairs of radio relics often called double radio relics are especially rare with only a few currently known

(Venturi et al., 2007; Bonafede et al., 2009a; Brown et al., 2011; Chibueze et al., 2021). The double relics are located on symmetrically opposite sides to the cluster center and perpendicular to the merging axis. These double relic systems can be used to constrain the merger geometry and timescales involved in the merging process (Roettiger et al., 1999a). Well-studied examples of single radio relics include the so-called 'Sausage relic' in the cluster CIZA J2242.8+530 (Van Weeren et al., 2010) and the 'Toothbrush relic' in RX J0603.3+4214 (Van Weeren et al., 2012). Well-studied examples of double radio relics include ZwCl 0008.8+5215 (van Weeren et al., 2011) and PLCKG287.0+32.9 (Bonafede et al., 2014). We show examples of single and double relics in Figure 1.5.

Relics trace out the re-acceleration of mildy relativistic CR electrons caused by the induced shock wave created during the initial merger event (Macario et al., 2011; Shimwell et al., 2015). Double radio relics trace the outward moving shock waves originating at the cluster centre. The currently proposed formation mechanism for the shocks associated with relics is the DSA mechanism (Ensslin et al., 1997; Kang & Ryu, 2015). In this mechanism, the ICM is compressed such that the magnetic fields align parallel to the shock front and electrons are accelerated to high energies. These ordered and aligned magnetic fields, coupled with relativistic electrons, give rise to large regions of highly polarised synchrotron radiation at radio wavelengths. During such events, the created shock waves are relatively weak, with moderate $\mathcal{M}$ in the range ($\mathcal{M} \sim 3 - 5$) (Miniati et al., 2001; Van Weeren et al., 2010). Therefore, pre-existing supra-thermal seed electrons* located at these peripheral regions are vital for the DSA model, if the predicted spectrum and luminosity of relics is to match that of the observed (Ensslin et al., 1997; Roettiger et al., 1999a).

---

[*] Supra-thermal electrons have characteristic energies (several keV) that are larger than the normal thermal population of electrons.

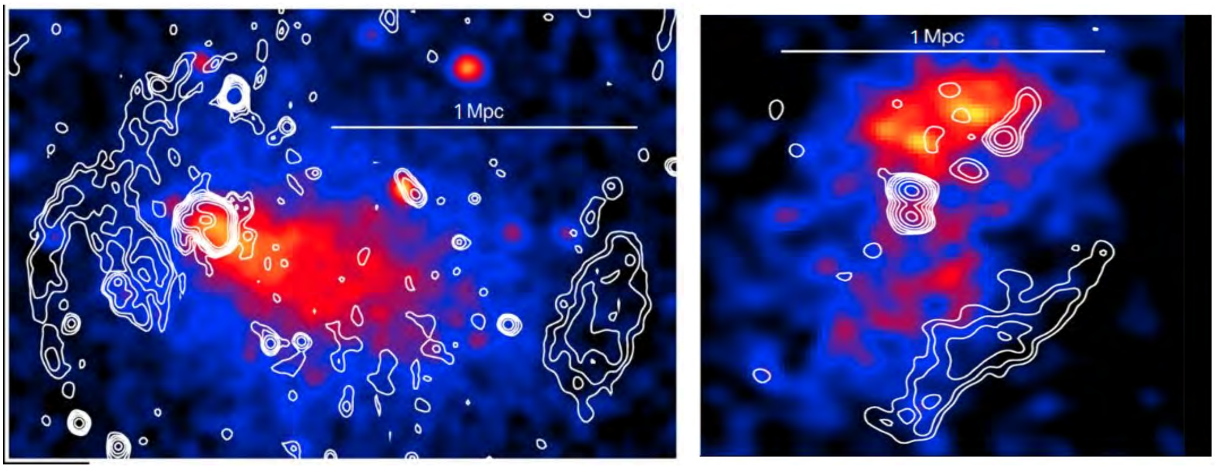

Figure 1.5: GMRT radio images (shown in white contours) overlayed with ROentgen SATellite (ROSAT) X-ray (0.1-2.4 keV) colour images for the two different types of relics. Spatial scales are shown by the horizontal white line. *Left*: GMRT 325 MHz radio image of the double relics in Abell 3376. The radio relics can be seen on either side of the cluster with different morphologies. An elongated and diffuse structure on the left and a diffuse and more defined structure on the right. The contour levels start from 5.8 mJy beam $^{-1}$ and increase by a factor of $\sqrt{2}$. The beam size is $39'' \times 39''$ (Kale et al., 2012). *Right*: GMRT 235 MHz radio image of the single radio relic found in the cluster PLCK G200.9-28.2. The contour levels are spaced as: $[1, 2, 4, ...] \times 3\sigma_{\rm rms}$, where $\sigma_{\rm rms} = 0.39$ mJy beam^{-1}. The beam size is $14.7'' \times 12.8''$ (Kale et al., 2017).

1.2.2.3 Ridge and bridge

Simulations have revealed a dynamically complex structure in which a shock acceleration mechanism due to a major merger is not the main source of the observed emission, as is the case with halos and relics; rather, it is turbulence in the inter-cluster bridge caused by complex dynamics of substructures embedded in filaments between galaxy clusters. This turbulence produces weak shocks ($\mathcal{M} \leq 2-3$) that cause re-acceleration of the pre-existing fossil electrons embedded in the filament of the bridge to radio energies (∼ GeV), which interact with large scale (∼ Mpc) weak (∼ nG) magnetic fields. Brunetti & Vazza (2020) have shown that the Fermi(II) re-acceleration mechanism is most favoured under these physical conditions and gives rise to very long dynamical time scales in the bridges connecting clusters. Radio emission is then observed following the filament connecting the two clusters. This type of source is called a *radio ridge*. A few clusters have been reported in the literature which show radio ridges between two clusters (Murgia et al., 2010; Botteon et al., 2018; Govoni et al., 2019; Botteon et al., 2020). The most notable of these is the spectacular 5 Mpc long radio ridge connecting the two massive clusters A399 and A401 (Govoni et al., 2019; Nunhokee et al., 2021), observed with the Low-Frequency Array (LOFAR) (van Haarlem et al., 2013). We show this specific example in the top left of Figure 1.6. Observations of radio ridge sources can provide us with an opportunity to probe unexplored mechanisms of in situ particle acceleration that operate on volumes of several Mpc and have the potential to probe the dissipation of energy on scales larger than galaxy clusters. Observing this type of source is a major challenge due to its truly diffuse nature on such large spatial scales (Brunetti & Vazza, 2020).

On smaller scales, ridges of radio emission have also been found connecting galaxy clusters with galaxy groups (Venturi et al., 2022) and in galaxy clusters hosting halos and relics, where the emission is seen in a central region between the halo and relic or double relics (Govoni et al., 2001; Bonafede et al., 2012; Carretti et al., 2013; Lindner et al., 2014; Brown & Rudnick, 2011; Bonafede et al., 2021). These types of sources are termed *radio bridge*. It has been suspected that the true nature of bridge-like sources between double relics are simply diffuse and very faint halos situated in the cluster centre, and due to resolution and sensitivity constraints they are perceived as bridges connecting the relics instead of being separate components.

Clusters such as A1758 (Giovannini et al., 2009), A3367 (de Gasperin et al., 2021) and RXCJ 1314.4–2515 (Venturi et al., 2007) are known to host halos between double relics. We show the cluster A3667 on the top right of Figure 1.6. In this image, a potential halo is seen residing between the two relics; one of its components however, is still connected to the relic on the right and could appear as a bridge-like structure in lower resolution data. The outer relics for these types of sources could be formed from shocks originating in the merging processes involving several substructures, while the central halo or ridge emission could be due to the large-scale turbulence at the cluster centre originating from these same merging processes. At the bottom of Figure 1.6 we show diffuse radio bridge emission between a galaxy cluster and a galaxy group in the Shapley Supercluster. This radio bridge structure detected with MeerKAT is particularly significant as it was detected at GHz frequencies whereas the few other cases of radio bridge detection were detected at much lower frequencies of a few hundreds MHz.

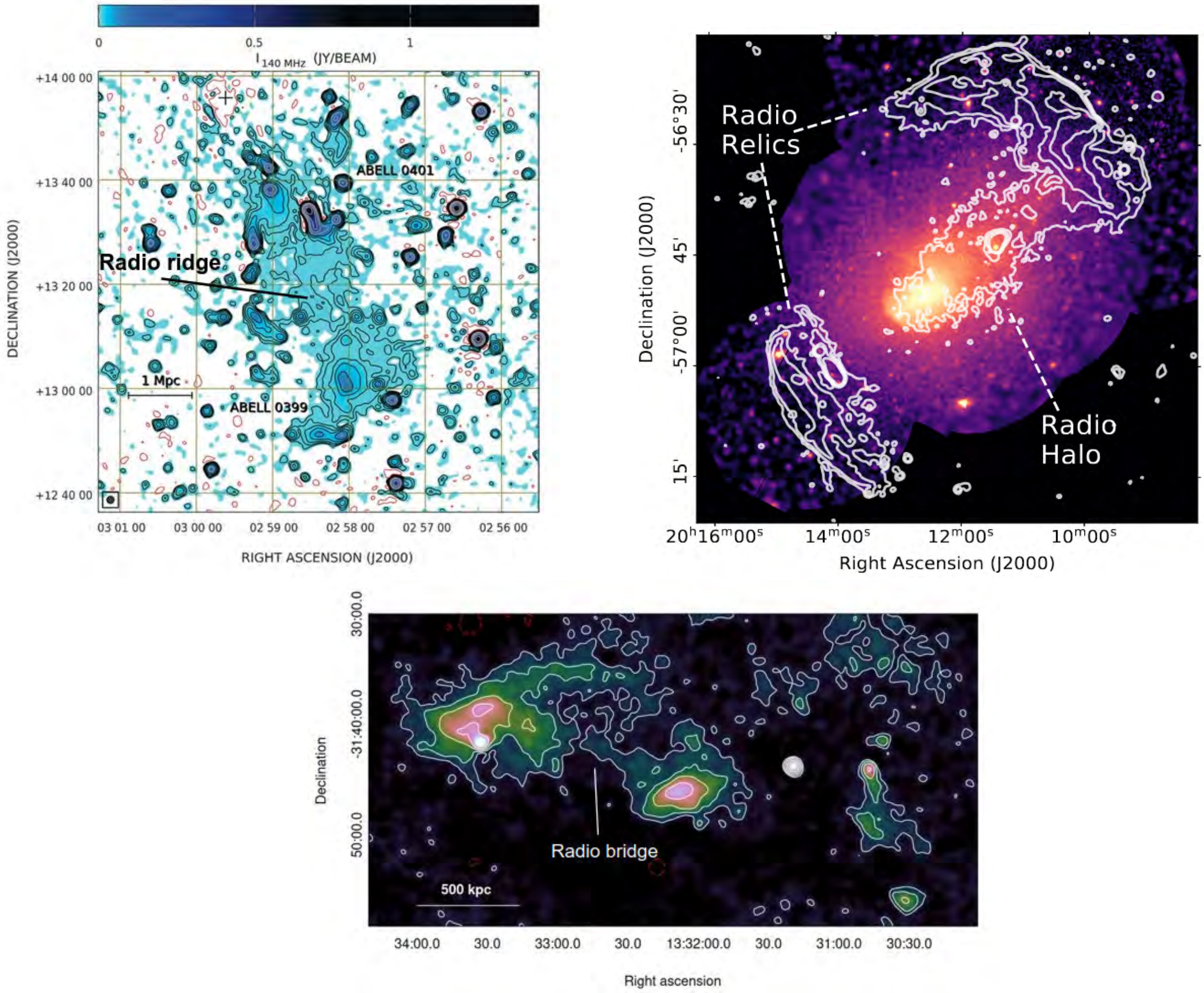

Figure 1.6: Diffuse radio emission between diffuse sources of different spatial scales. The diffuse radio source in each image is labelled. *Left*: 140 MHz LOFAR radio image of the $1.4^{\circ} \times 1.4^{\circ}$ region centred on Abell 0399-0401 system. Colour and contours both show the radio emission at 140 MHz with beam size 80″ (shown bottom left) and $1\sigma_{\rm rms} = 1$ mJy beam^{-1}. The contour levels start at $3\sigma_{\rm rms}$ and increase by factors of 2. Large scale diffuse emission is seen connecting the two clusters (Govoni et al., 2019). *Right*: MeerKAT 1283 MHz radio contours image overlayed on XMM-Newton X-ray colour image of the cluster A3667, which hosts a potential central halo between peripheral relics. The contours are spaced as: $[5, 20, 80, 320] \times 1\sigma_{\rm rms}$, where $1\sigma_{\rm rms} = 17$ μJy beam^{-1}. The beam size is 35″×35″ (de Gasperin et al., 2021). *Bottom*: 1283 MHz MeerKAT radio colour and contour image of a region in the Shapley supercluster involving the minor merger of the galaxy cluster A3562, with a galaxy group SC1329–31. The image has been convolved with a beam of 40″×40″. The contour levels are spaced as: $[1, 2, 4, 9] \times 3\sigma_{\rm rms}$, where $1\sigma_{\rm rms} = 30$ μJy beam^{-1}. Large scale ∼ 1 Mpc and low surface brightness diffuse emission can be seen between the galaxy cluster and group (Venturi et al., 2022).

1.2.3 The relationship between diffuse emission and cluster properties

Correlations should exist between the radio, thermal and physical properties of merging galaxy clusters hosting diffuse radio sources, based on the idea that the energy dissipated during cluster–cluster mergers power the formation of these sources (Cassano et al., 2010, 2013; Yuan et al., 2015; Cuciti et al., 2021; Duchesne et al., 2021). The most well studied is that of the link between the detection of diffuse emission and its X-ray luminosity L_X (Giovannini et al., 1999), with the highest radio halo probability detection in clusters with the highest L_X. Feretti et al. (2000); Liang et al. (2000) and Govoni et al. (2001) were among the first to find an explicit relationship between the X-ray and radio properties of galaxy clusters through a power-law correlation of the radio halo power P with L_X. Since the L_X is also a tracer of the cluster mass $\mathrm{M}_\odot$ and is linked to the cluster temperature T_X, the correlation can be extended between the radio power with $\mathrm{M}_\odot$ and T_X. For observational reasons, the radio power at 1.4 GHz ($P_{1.4\mathrm{GHz}}$) is often used and the X-ray luminosity is often reported in the $0.1 - 2.4$ keV band (therefore also denoted $L_{[0.1-2.4]\mathrm{keV}}$). The general relation can be written as:

$$\log(P_{1.4\mathrm{GHz}}) = \beta \log(Y) + C\ , \tag{1.4}$$

where C is the normalisation factor, β is the proportionality factor and Y can take the form of L_X, $\mathrm{M}_\odot$ or T_X. An extensive study by Brunetti et al. (2007, 2009) for the $P_{1.4\mathrm{GHz}}$ vs L_X was conducted for a sample of halo emitting galaxy clusters from GMRT (Venturi et al., 2007, 2008) and literature. Halo emitting clusters traced the $P_{1.4\mathrm{GHz}} - L_X$ correlation while halo absent clusters were well separated, with upper limits located well below the expected correlation. We show one such correlation on the left of Figure 1.7. This clear separation of radio halo-emitting clusters from radio halo-absent clusters can be understood from the radio halo-merger connection in which clusters follow the evolutionary path:

- Galaxy clusters host radio halos for a period of time from dynamics induced by cluster mergers and populate the $P_{1.4\mathrm{GHz}} - L_X$ correlation;
- After some period of time the clusters become dynamically relaxed and their Mpc scale

emission is gradually suppressed and clusters populate the bottom right region of the upper limits.

These same correlations naturally extend to systems hosting single (Giovannini & Feretti, 2002) and double relics (Feretti et al., 2012), with the radio power relationship extending to additional properties (additional forms of Y in Equation 1.4) such as relic largest linear size (LLS), projected distance and spectral index (Bonafede et al., 2012; Ade et al., 2014). These new correlations showed that relics with high radio power have larger linear sizes and that there is a tendency of larger relics to generally be located at larger distances from the cluster centre and of smaller relics to have steeper spectral indices.

1.3 Radio telescopes

A device that converts radio frequency fields into current is called an antenna. A radio telescope is an antenna designed to observe faint radio emissions from the sky. A typical radio telescope has three major components, namely mount, optics and electronics receiver systems. We briefly cover the former two, while the latter is discussed at the beginning of §2. We use an example antenna shown on the left in Figure 1.8, with labels demonstrating the location of these major components and show other types of mount and optic designs on the right in Figure 1.8.

The main optical components are the primary reflector surface and sub-reflector. The primary reflector surface is a large parabolic dish* designed to collect signals and reflect/propagate them onto a smaller sub-reflector where they are captured by the receiver. This is an example of a dual reflector system. A single reflector design only has the main (or primary) reflector and a receiver. The antenna shown on the left of Figure 1.8 is a dual reflector design corresponding to the offset

---

*A parabolic dish has a non-uniform response to incoming radiation from different directions. It has maximum sensitivity in the pointing direction (phase centre) that drops off away from that direction. This sensitivity pattern is known as the primary beam pattern. The full width at half maximum (FWHM) of the main lobe from this primary beam pattern is the measure of the beam size.

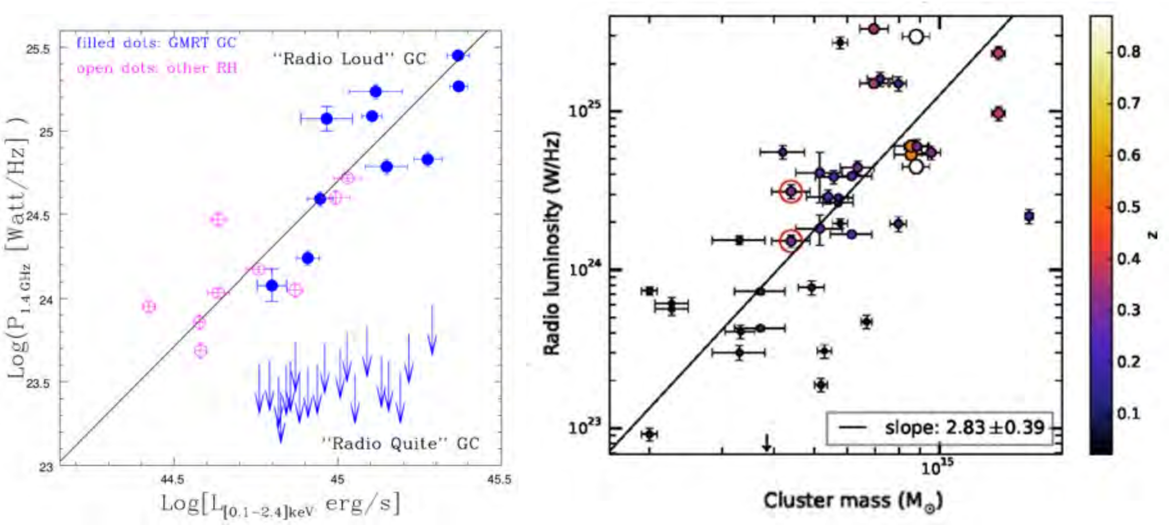

Figure 1.7: The correlation between X-ray luminosity and mass vs radio power of a sample of galaxy clusters which host diffuse radio sources. *Left*: The halo radio power $P_{1.4\text{GHz}}$ vs X-ray luminosity L_x correlation first reported by Brunetti et al. (2009) for a sample of galaxy clusters hosting halos from the GMRT survey and literature. These samples are indicted by the small circles and are expected to follow the correlation (solid line). The filled blue circles are clusters at $0.2 \leq z \leq 0.4$ from GMRT while the empty pink circles are clusters with z lower than this from literature. The blue arrows at the bottom right are halo absent (radio quite) clusters from the GMRT survey. The length of the arrows represent the upper limits that are all well below the correlation. *Right*: Relic radio power $P_{1.4\text{GHz}}$ vs cluster mass $M_\odot$ for a sample of single and double relic clusters from Feretti et al. (2012). The z is colour-coded (shown on right). Each relic in the double relic cluster is separately plotted for the same cluster mass but for different radio powers. Each relic is therefore situated at the same horizontal position, but vertically separated depending on the differences in their radio power. We use the double relics of PSZ1 G096.89+24.17 (shown by the two red circles) to illustrate this (Ade et al., 2014).

Gregorian model of (2c) on the bottom right under the optics panel (Figure 1.8). The optics of (2a) is an example of a single reflector system.

Radio telescopes can function either as steerable (tracking) or transit (non-tracking). The two mounts shown on the left in the top panel of Figure 1.8, the equatorial mount (1a) and the alt-azimuth mount (1b), are both examples of steerable antennas. Alt-azimuth mounts allow the primary reflector to rotate about two perpendicular axes, horizontally and vertically. Advantages of the alt-azimuth mount design include its inexpensive design and the fact that gravity acts in the same plane keeping the reflector profile stable and accurate. One disadvantage of this design is that, as the antenna tracks a source, the aperture rotates with respect to the source causing beam asymmetries (Iheanetu et al., 2019). The equatorial mount tracks sources along the polar axis aligned in a plane parallel to the Earth's rotation. The advantage is that the beam asymmetries of the previous design are avoided as a result of rotation along a single axis. Disadvantages include expensive cost and its inability to observe sources close to the horizon.

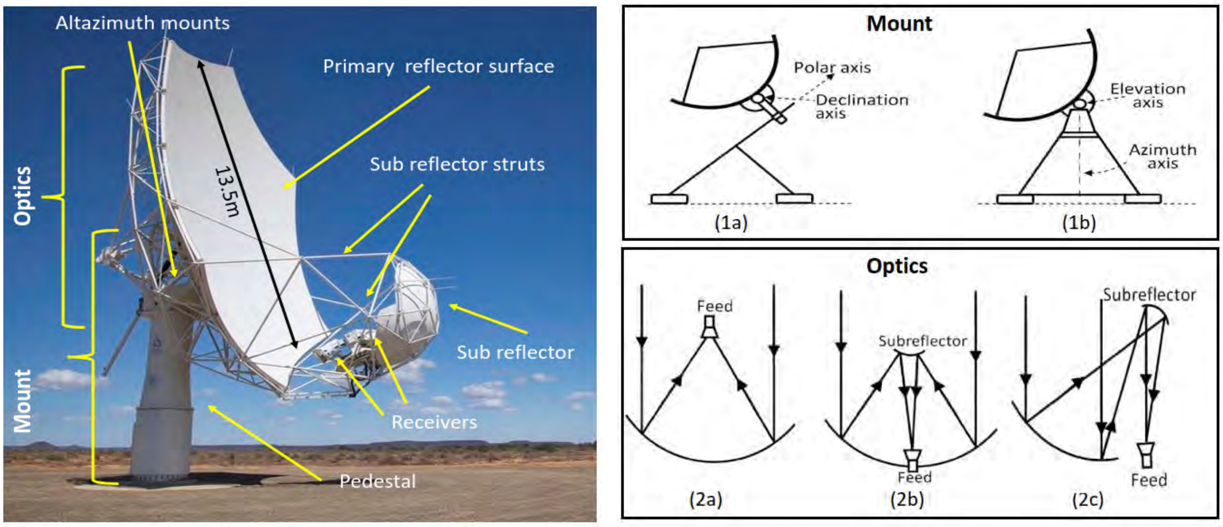

Figure 1.8: The major components of an antenna including examples of some mount and optic designs. *Left*: The MeerKAT single antenna used as an example with labels showing the main optical and mount components. *Right*: Top panel shows two steerable mounts: (1a): Equitorial mount and (1b): Alt-azimuth mount. Bottom panel shows an example of three optical designs: (2a): Prime focus, (2b): Cassegrain and (2c): offset Gregorian (Perley et al., 1989; Jonas, 2009; Booth & Jonas, 2012).

1.3.1 MeerKAT

MeerKAT is a 64 telescope array that lies in a radio-quiet Karoo semi-desert region situated in the remote Northern Cape province of South Africa (Jonas, 2009; Jonas & Team, 2016; Mauch et al., 2020). This region has ideal conditions to conduct radio astronomy as it experiences little stray interference from cellular phone networks and TV broadcasts. It is a precursor to the international Square Kilometer Array (SKA) project and will form an integral part of the mid frequency component of SKA, SKA-MID. MeerKAT is currently the most sensitive cm-wavelength telescope in the southern hemisphere, observing the sky below a declination of $+45^{\circ}$ (given its limiting elevation of $+15^{\circ}$). The MeerKAT antennas use an offset Gregorian design equipped with a parabolic primary reflector (13.5 m diameter) and a concave ellipsoidal symmetric sub-reflector (3.4 m diameter), installed on alt-azimuth mounts (Booth et al., 2009). The example antenna of Figure 1.8 is the MeerKAT antenna containing labels of these components.

The MeerKAT correlator supports 1024, 4096 and 32768 channel modes. Three receivers are available: (1) UHF-band: 580–1015 MHz, (2) L-band: 900–1670 MHz and (3) S-band*: 1.75-3.5 GHz (Jonas & Team, 2018). The centre frequencies are 800 MHz, 1283 MHz and 2625 MHz for UHF, L-band and S-band, respectively. Its scientific scope offers to cover a range of physics and astronomy topics such as the evolution of galaxies and galaxy clusters, investigating the role of HI in the early Universe and further testing of general relativity (Booth & Jonas, 2012). The total number of baselines, given a 64 telescope array, is 2016. The maximum and minimum baseline for MeerKAT is 8 km and 29 m, respectively. This allows observation of radio sources with angular scales between $5''$ and $27'$ at 1283 MHz. The central/inner dense component of MeerKAT, containing 70% of the receiving area, is 1 km in diameter, which serves to improve sensitivity towards imaging of extended radio sources. The outer component, consisting of the remaining 30% of dishes, is distributed out to a diameter of 8 km (Jonas & Team, 2018). A close-up view of a few MeerKAT antennas and the central square array configuration in which they are situated are both depicted at the top of Figure 1.9. We show at the bottom of Figure 1.9 the MeerKAT antenna layout for the core (600 m maximum baseline) and full (16 km maximum

---

*Currently in commissioning.

baseline) region.

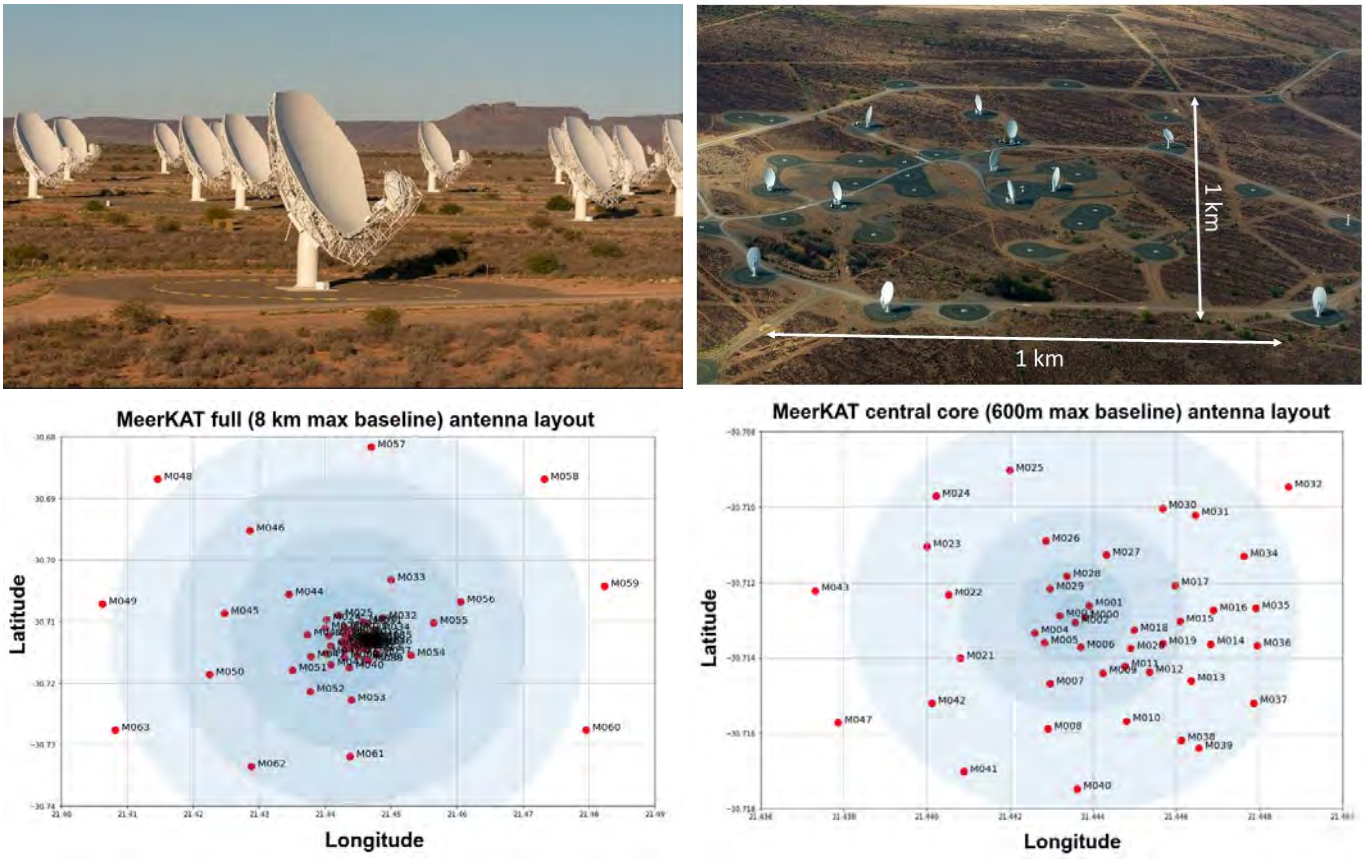

Figure 1.9: MeerKAT antennas and antenna layout for the whole and central square region of the array. *Top*: MeerKAT antennas (left) and the central square region of the MeerKAT array (right). *Bottom*: MeerKAT full antenna layout (left) and antenna layout for the central square region (right). The antennas are shown as red dots with corresponding labels. Each coloured ring is of different diameter. For the left image, the coloured rings are 1, 2, 4, 6, 8 km in diameter. For the right image, the coloured rings are 50, 100, 300 and 600 m in diameter (Jonas, 2009; Booth & Jonas, 2012).

The high sensitivity of MeerKAT is attributed to its large collecting area, A_e and low system temperature, T_{sys}. The large collecting area is partially a result of the unique offset Gregorian optic design (right panel of Figure 1.9, labelled (2c) under ‘optics’), as opposed to the more common centre-feed antenna model (right panel of Figure 1.9, labelled (2a) under ‘optics’) (Jonas & Team, 2018). This unique antenna design eliminates blockage of the primary aperture, providing uncompromised optical performance and sensitivity, excellent imaging quality and good rejection of unwanted radio frequency interference from satellites and terrestrial transmitters (Booth & Jonas, 2012). Typical data sets for usual observation times (4-8 hours) with normal settings (8 seconds sampling time, 4000 channels) can be several hundreds of GBs to a few TB in size.

1.3.2 The Giant Metrewave Radio Telescope

The Giant Metrewave Radio Telescope (GMRT), located in Khodad, India, is one of the largest and most sensitive low-frequency radio telescopes in the world (Swarup et al., 1997; Ananthakrishnan, 2005; Gupta et al., 2017). GMRT was one of the first in a series of new radio observatories that made an impact on low-frequency radio astronomy in the 1990s. Shortly after its commission, new facilities such as LOFAR and Murchison Widefield Array (MWA) (Tingay et al., 2013) joined the scene, becoming operational by the end of 2010. The GMRT array configuration consists of 30 antennas (each of 45 m diameter) spanning over 25 km. 14 antennas make up the central core of the array while the remaining 16 antennas are arranged around the core to form a Y-shape. The distribution of antennas allows for good uv coverage on both the short and long baselines, providing a total collecting area of about $30,000$ m^2 at metre wavelengths. Before its upgrade, it operated at five frequency bands in the range of 120-1450 MHz: 150, 245, 320, 610 and 1420 MHz, each with bandwidths of 33.3 MHz. The maximum and minimum baselines of GMRT are 25 km and 100 m, respectively. This allows observation of radio sources with angular scales between $5''$ and $43'$ at 610 MHz.

The recent upgrades to the GMRT telescope, ‘upgraded GMRT’ (uGMRT), have made it one of the most sensitive instruments operating at centimetre and decimetre wavelengths. These improvements initially took place in 2010, with completion in 2018. This upgrade included broadband receivers and a backend which now incorporates an additional four bands of 400 MHz bandwidth: $50-80$ MHz (band 1), $120-250$ MHz (band 2), $250-500$ MHz (band 3), $550-850$

MHz (band 4) and 1050 – 1450 MHz (band 5). The older narrow band receivers are referred to as 'Legacy GMRT' and the bands after upgrade are referred to as 'upgraded GMRT' (uGMRT). In addition to these bandwidth enhancements, extra capability to the existing GMRT array in terms of uv-coverage and sensitivity has also been employed. These changes have allowed for the imaging of extended sources to sizes twice of what was possible with the legacy GMRT (van Weeren, 2015). GMRT has always had noticeable RFI issues at frequencies lower than 700 MHz; as a result, the uGMRT has implemented a new RFI online filter that performs real-time broadband and narrowband RFI excision that can effectively deal with broadband RFI mitigation at these frequencies (Buch et al., 2016). Typical data sets for a few hours of observation time with default settings (16s sampling time, 256 frequency channels) are only a few GB in size ($<$ 10GB) for the Legacy GMRT and are several tens of GBs for the uGMRT. Until the arrival of Phase 1 of the SKA, SKA1, uGMRT will be one of the most sensitive facilities operating in the 250–1500 MHz frequency range. We show in Figure 1.10 the GMRT single antenna, GMRT array and bandwidth comparison between the GMRT with uGMRT.

1.3.3 The future SKA and current precursors

The SKA[*] is the most ambitious science project of the 21st century. The SKA attempts to build the worlds largest radio telescope with one square kilometre of collecting area (Hall et al., 2008). It will exploit techniques of interferometry and aperture synthesis used in radio astronomy to combine thousands of many small antennas to simulate a single giant radio telescope capable of extremely high sensitivity and angular resolution. It represents the next major step in radio astronomical facilities, providing two orders of magnitude increase in collecting area over current existing telescopes. The idea of the SKA was first conceived in the 1990s and later developed and elaborated in the 2010s. The SKA will be built in the southern hemisphere with the core locations being South Africa and Australia. The entire SKA organisation includes 14 countries[†] with the headquarters located at the Jodrell Bank Observatory in the UK.

---

[*] `https://www.skatelescope.org`

[†] The 16 member countries in addition to South Africa and Australia include, Canada, China, France, Germany, India, Italy, New Zealand, Spain, Netherlands, United Kingdom, Sweden, South Korea, Portugal and Switzerland.

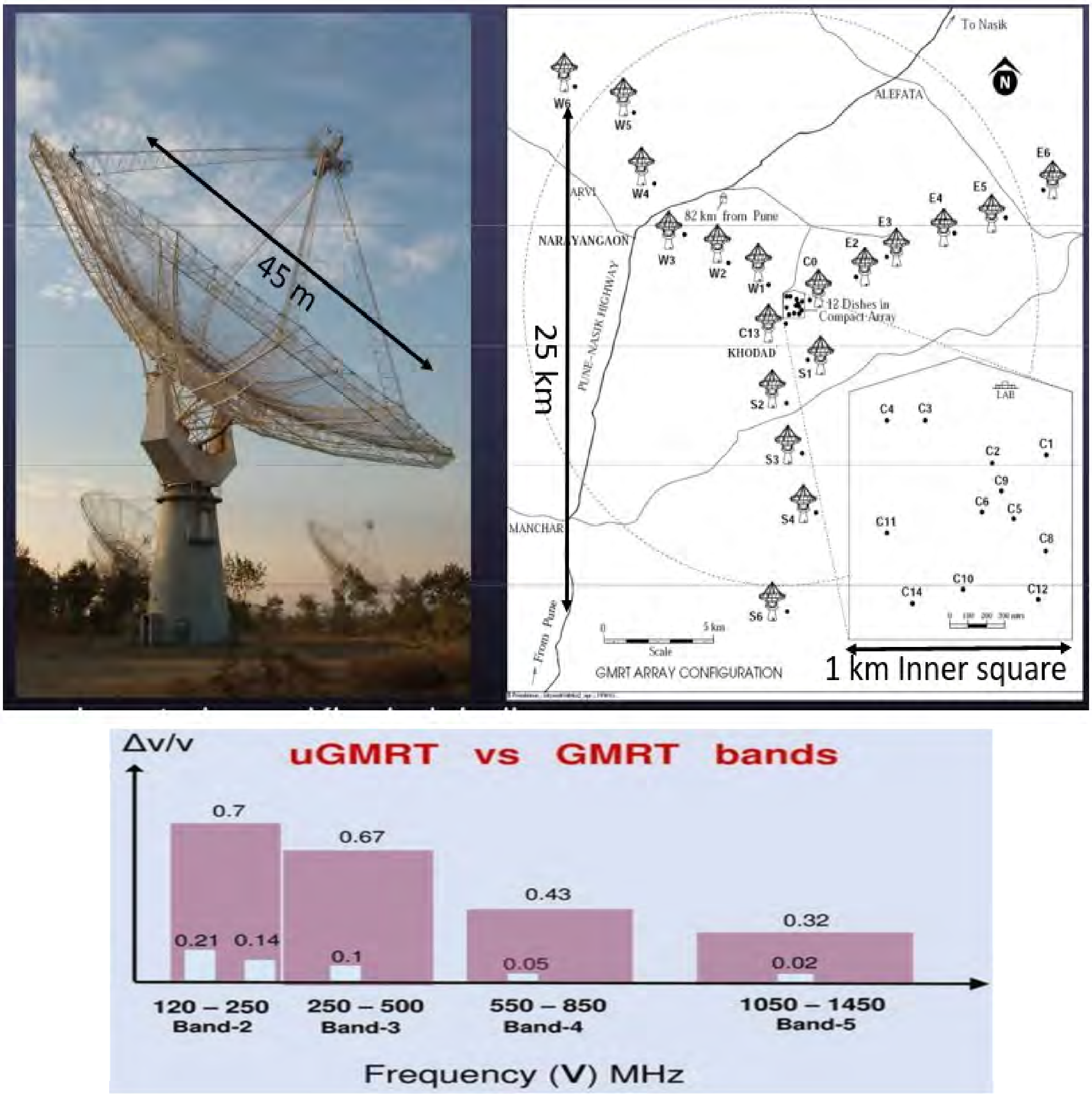

Figure 1.10: GMRT single antenna, antenna array configuration and uGMRT vs GMRT band comparison. *Top*: Left image shows a single 45 m steerable GMRT antenna. Right image shows the 30 dish GMRT array configuration. An enlarged region of the central square is shown at the bottom right. *Bottom*: Bandwidth comparison of the Legacy GMRT with the newer uGMRT. The wider pink bars represent the new uGMRT bands while the narrower light blue bars within the wider pink bars represent the older Legacy GMRT bands (Gupta et al., 2017).

A series of demonstrator telescopes and systems known as SKA pathfinders[‡] and precursors,

---

[‡] Some examples of current SKA pathfinders include GMRT in India, LOFAR in Netherlands, Five-hundred-meter Aperture Spherical Telescope (FAST) in China and the Very LArge Array (VLA) in the USA.

are already operational or under development across the world. These will play a major role in predicting the required technology that will need to be developed to cater for the goals of the SKA. We have already mentioned the MeerKAT precursor in §1.3.1, which is the focal point for SKA South Africa. Apart from MeerKAT, three other SKA pre-cursors exist in the Southern hemisphere: Hydrogen Epoch of Reionization Array (HERA) (DeBoer et al., 2017) , Australian SKA Pathfinder (ASKAP) (Johnston et al., 2008), and MWA. HERA and MeerKAT are situated in South Africa, while the latter two are situated in Australia. In the top of Figure 1.12 we show the current SKA-precursors.

South Africa's Karoo region will host the core of the high- and mid-frequency dishes forming SKA-MID, Western Australia's Murchison Shire region will host the low-frequency antennas forming SKA-LOW. The full SKA will be implemented in phases, with each subsequent phase adding more antennas than the previous. The first phase of the SKA, SKA1, is planned for the year 2025-2027. It will include additional dishes to MeerKAT and ASKAP. SKA1-MID will include an addition of 133 dish antennas to the existing 64-dish MeerKAT array and a frequency coverage of 0.35 to 13.8 GHz. In total there will be nearly 200 dishes situated in a dense core and extending in three spiral arms over 150 km. The density of the core will decreases with radial distance and the vast majority of antennas will fall within a square kilometre; while only a handful of antennas at the extremes of the core (about 4 km from the core). We show this layout in Figure 1.11. The full SKA will entail further expansion of dishes across SKA1-LOW and SKA1-MID and ultimately over the southern African continent; spreading over at least 3000 km, and with a frequency coverage extending from 70 MHz to at least 25 GHz. We show at the bottom of Figure 1.12 a conceptualised image of the future SKA in South Africa and how SKA1 compares to current modern interferometers in terms of sensitivity.

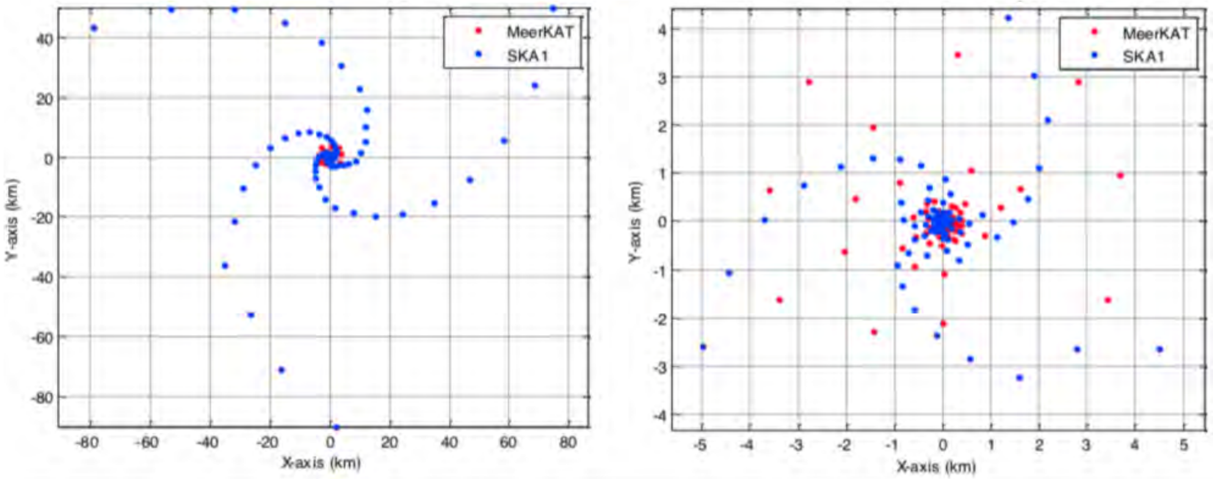

Figure 1.11: SKA1-MID layout (blue dots) including the current MeerKAT antennas (red dots) showing the three spiral arms of maximum baselines of 150 km (*Left*) and 10 km (*Right*).

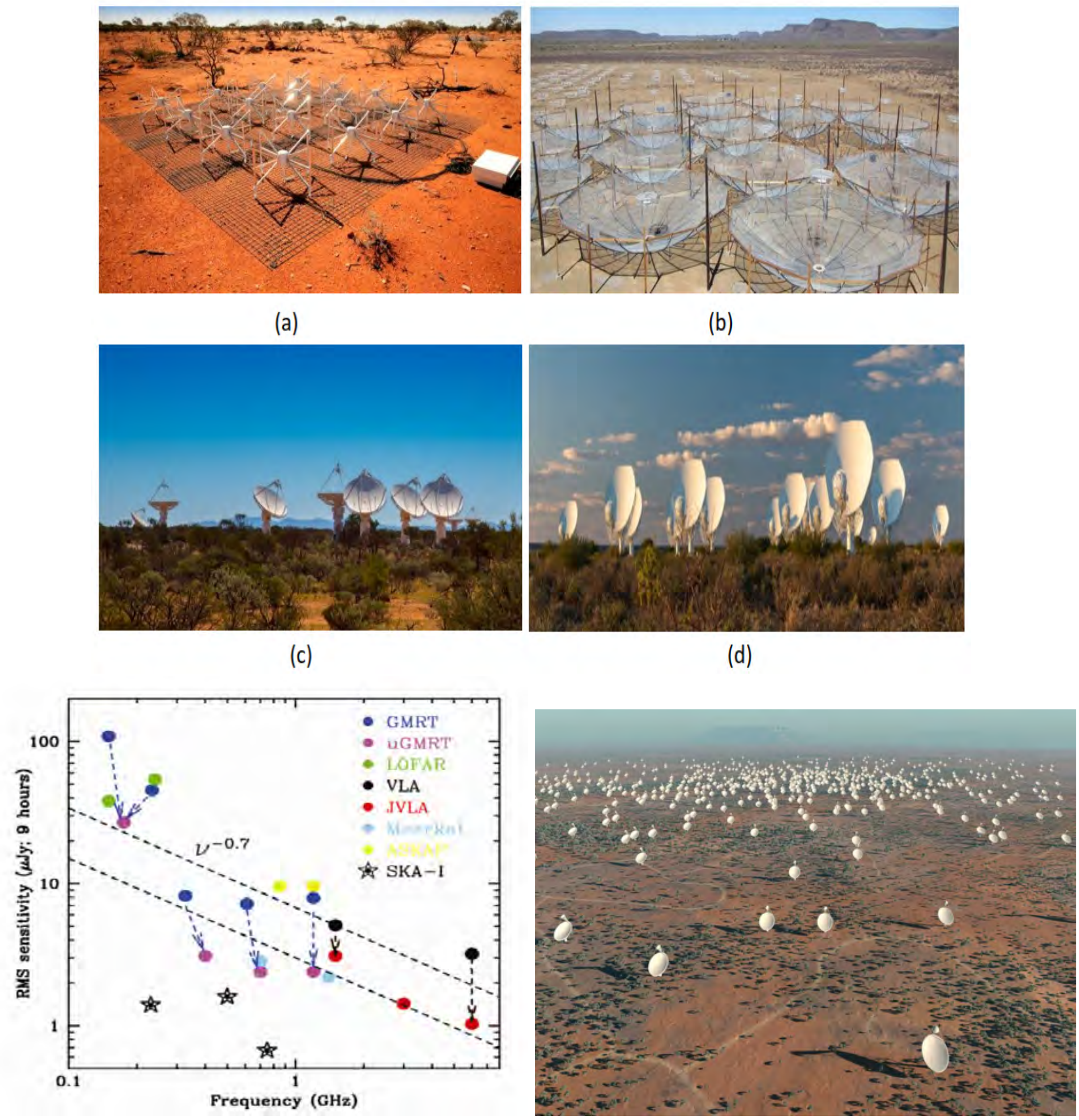

Figure 1.12: SKA precursors and future SKA1 sensitivity and conceptualisation. *Top*: SKA precursors in South Africa and Australia: (a), (b), (c) and (d) are MWA, HERA, ASKAP and MeerKAT, respectively. *Bottom*: The left panel shows the continuum sensitivities comparison between the SKA precursors, SKA pathfinders and the SKA1 at various frequency ranges for a source observed for nine hours. The sensitivity of SKA1 (black stars) are well-below that of the other interferometers (Gupta et al., 2017). The right panel shows an artist impression of the final phases of the SKA1.

Chapter 2

Radio interferometry

The increasing demands for higher resolution images in radio astronomy and impracticality of building single-dish telescopes to cater for this resolution have necessitated the switch from large dishes to many smaller antennas or stations[*]. Radiation captured by antennas in an array are a direct consequence of the interaction of incoming incoherent electromagnetic (EM) waves (called signals) originating from astrophysical sources with the receiver. The family of techniques used to constructively interfere signals collected by the different antennas in an array and combine them to act as one in order to produce output from what a single telescope would capture is called interferometry (Thompson et al., 2004). A minimum of two antennas (forming a single baseline) observing simultaneously at the same frequency are required for interferometry. We show this scenario in Figure 2.1. The antenna receivers/feed consist of two receptors that convert the signal to voltages. Each receiver is sensitive to only one of two mutually opposite polarisations (X or Y for linearly polarised and L or R for circularly polarised). These voltages are fed to various electronics (such as filters) where they are amplified and finally fed to the correlator. The correlator combines the signals from the different antennas by multiplying them and time-averaging the product. The final form of this product is the complex visibilities.

2.1 Radio interferometer response: The van Cittert–Zernike theorem

In radio astronomy, all sources in the sky are treated as being spatially incoherent. This Source incoherency is a direct consequence of treating different parts of the sky as being statistically independent. This combined with the fact that the wavefront of incoming radiation emanating from these sources are located at such large distances away from the receiver, makes them almost

---

[*] A station refers to any element of an interferometric array that produces two output signals, one for each polarization. For example, a parabolic dish or aperture array.

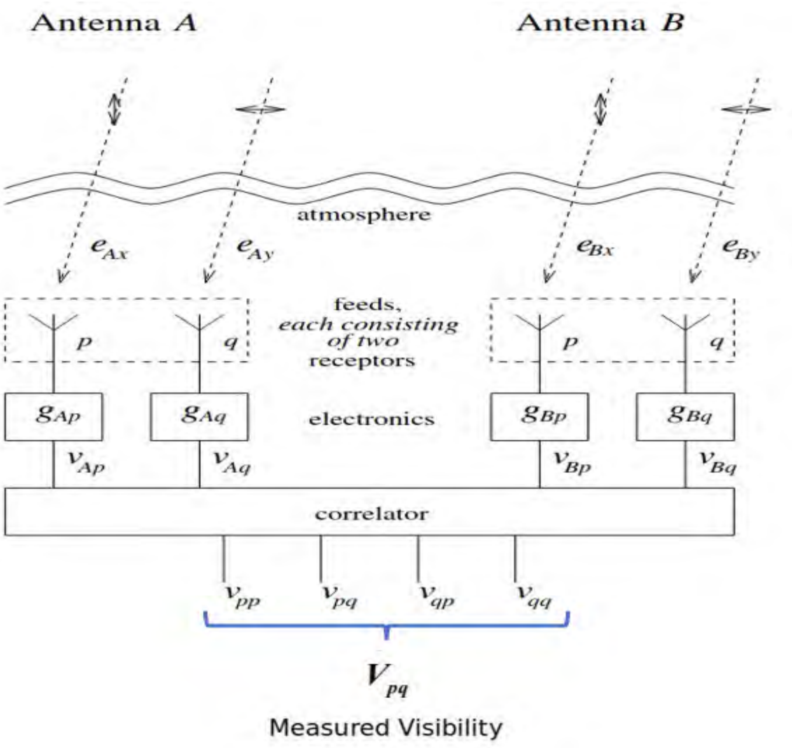

Figure 2.1: Schematic diagram of a simple interferometric system consisting of two antennas, A and B, each with correlator feeds p and q, showing the chain of equipment utilised in the processing of incident radiation induced on the primary reflector (Hamaker et al., 1996; Thompson et al., 2004).

coherent when they reach the receiver. This allows for application of the van Cittert–Zernike (vCZ) theorem (Thompson et al., 2008). The vCZ theorem states that under certain conditions, the Fourier Transform (FT) of the intensity distribution of a far-field, incoherent source is equal to the degree of coherence of the corresponding wave-fronts from that source reaching the receiver (Mandel & Wolf, 1995). In the context of radio astronomy, each pair of antennas in an array forms a baseline, the baselines make up a coordinate system residing in visibility space called baseline coordinates (u, v, w)*; where the w axis points outward from the phase centre. Each

---

*Baseline coordinates are the differences between the Cartesian coordinates for the position between two antennas in units of wavelength. For antennas p and q, the baseline coordinate is: $\boldsymbol{B}_{pq} = (B_x, B_y, B_z)_{pq} = (x_p - x_q, y_p - y_q, z_p - z_q)$.

baseline measures a single and different point in visibility space, which therefore, measures a different degree of coherency of the incoming radiation. This degree of coherence is encapsulated into a function called the complex visibility function, $V(u,v,w)$. Each point in visibility space can be mapped to a point in the sky. Sources in the sky are modelled as points on a celestial sphere residing in image space; with the position of each point being described by the angular coordinates (l,m,n), where l and m are directional cosines and $n = \sqrt{1-l^2-m^2}$. The entire source population is encoded in the source intensity distribution function $I(l,m,n)$, also called the sky brightness or brightness distribution function (Taylor et al., 1999). We show in Figure 2.2 a schematic diagram of the relationship between image and visibility space.

The vCZ theorem in the context of radio astronomy therefore states that the complex visibility function, $V(u,v,w)$, representing all measured points in visibility space, is the FT of the intensity distribution of the sky brightness or brightness distribution $I(l,m,n)$ (representing all points in image space mapped from visibility space) (Taylor et al., 1999). The exact conditions under which this vCZ theorem holds (excluding source incoherency and far-field already mentioned) includes homogeneity of the propagation medium, small field approximation, co-planar baselines and narrow-bandwidth. Under these conditions, given a two-element phase tracking interferometer, we can use the vCZ theorem to write out its general response to spatially incoherent radiation from a far field:

$$V(u,v,w) = \int_{-\infty}^{+\infty}\int_{-\infty}^{+\infty} A(l,m)I(l,m)e^{-2\pi i\left[u_{pq}l+v_{pq}m+w_{pq}\left(\sqrt{1-l^2-m^2}-1\right)\right]}\frac{dl\,dm}{\sqrt{1-l^2-m^2}}\ . \tag{2.1}$$

Where $V(u,v,w)$ is the visibilities, $I(l,m)$ is the true sky brightness and $A(l,m)$ is the primary beam effect. The primary beam effect is the inevitable manifestation of the primary beam pattern (see footnote of § 1.3) in synthesized images that causes degradation of the image quality the further you move from the phase centre. Equation 2.1 describes the relationship between the projection of $V(u,v,w)$ onto a plane tangent to the celestial sphere (forming $I(l,m)$) perpendicular to the line of sight n (Cornwell & Perley, 1992). We show a schematic diagram of the geometric setup of Equation 2.1 on the right of Figure 2.2. The process of recovering the sky brightness $I(l,m)$ from the visibilities $V(u,v,w)$ forming a two-dimensional image through Fourier synthesis (application of Equation 2.1) using an ensemble of two-element interferometers is known as aperture synthesis or synthesis imaging.

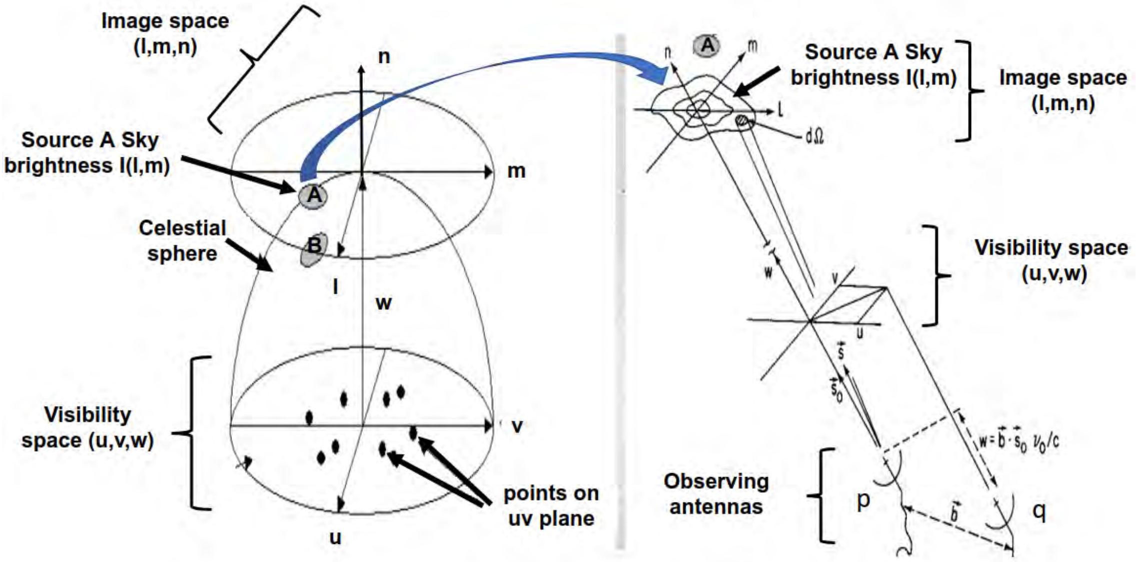

Figure 2.2: Relationship between the two coordinate systems, image (l, m, n) and visibility (u, v, w) space, used in radio astronomy. The angular coordinates (l, m, n) and baseline coordinates (u, v, w) unit vectors are shown as Cartesian unit vectors. *Left*: A large scale view of the relationship between these two coordinate systems. Sources A and B reside on the surface of the celestial sphere and are shown by the small shaded ellipse regions (with sky brightness $I(l, m)$) and are sub-spaces of image space (Perley et al., 1989). *Right*: A close-up view of the left showing the geometric setup for observation of source A by two antennas p and q. A small area element of solid angle $d\Omega$ of $I(l, m)$ is shown as observed by antenna p at position $\vec{s}_0 + \vec{s}$ (Taylor et al., 1999).

Aperture synthesis is essentially the entire observational procedure from the input signal to the output image. It includes many components, one of which is the correcting of visibility data before they are combined into an image. The wavefronts emanating from sources undergo various corruptions as they transverse through different interstellar mediums before they reach the receiver. There are also various instrumental and electronic-based errors related to telescope designs and array configurations that must be taken into account. The purpose of calibration is to remove the effects of these atmospheric and instrumental related errors that come with measurements of the visibility function (Thompson et al., 2004). The imaging and calibration problem have traditionally been treated as separable and independent. A modern framework has recently been devised formulating imaging and calibration as a single problem; being two sides of the same coin. This framework is known as the the Radio Interferometric Measurement Equation (RIME) and is of major convenience for understanding the problems related to the stages of aperture synthesis.

2.2 Radio interferometry framework: The measurement equation RIME

The initial work of Hamaker et al. (1996) developed a formulation of an explicit RIME that unified the concepts of Stokes parameters*, Jones matrices and radio interferometry into a single framework. Further work by Hamaker (2000) then led to a fully 2×2 matrix formulation of the RIME, providing the mathematical underpinnings of a generic radio telescope. The RIME formalism provides a convenient and rigorous mathematical framework for tackling the problem of calibration (Smirnov, 2011). It is built upon matrix algebra; its simplicity gives a clear description of the propagation effects induced on a signal from its path from source to the correlator. It does this by representing all the corruptions transforming the original electric field in the form of linear (2×2) transformations matrices, called Jones matrices (Jones, 1941) as multiplicative factors of the observed visibility matrix. Each Jones term describes a different effect, has its own specific implementation (if the term is known prior) and parametrisation (if the term is solvable). Below is an example of one such equation for a two-element interferometer pq, that measures the true sky X from the visibilities V, including the effects of electronic gain G, antenna geometry K, primary beam B and ionosphere D:

---

*Stokes parameters are a set of four parameters universally used to measure the degree of polarisation of a source. They are related to the amplitudes of the components of the electric field, E_x and E_y, that are both perpendicular to one another and normal to the direction of wave propagation.

$$\underbrace{\boxed{V_{pq}^{meas}}}_{\text{Measured Visibilities}} = \underbrace{\boxed{G_p \cdot \left(\int_s K_{p,s} \cdot B_{p,s} \cdot I_{p,s} \right.}}_{\text{Calibration}} \underbrace{\boxed{X_s \cdot X_s^H}}_{\text{Sky}} \underbrace{\boxed{\left. I_{q,s}^H \cdot B_{q,s}^H \cdot K_{q,s}^H ds \right) \cdot G_q^H}}_{\text{Calibration}} . \tag{2.2}$$

The outer G terms are called direction-independent (DI) effects and the inner terms are called direction-dependent (DD) effects that must be integrated over all directions s. In essence, DI effects contain little variability across the entire Field of View (FoV)[†] while DD effects vary significantly. The latter requires more elaborate techniques to solve than the former. The specific details of these effects are not important for this current discussion. We leave this for §2.3.4. The striking similarity of Equation 2.2 to the vCZ equation of radio astronomy in Equation 2.1 is obvious. We will describe the procedure involved in deriving this framework.

Given a simple monochromatic signal that is described by a vector $\boldsymbol{e}$ in an arbitrary coordinate system with the direction of propagation from sky source, to antenna, to receiver to correlator, to measurement of complex voltages $\boldsymbol{v}$, if we have a single antenna consisting of a correlator with two feeds a and b with associated complex voltages v_a and v_b, then the linear relationship for this system will be given by:

$$\boldsymbol{v} = \boldsymbol{J}\,\boldsymbol{e} \Longleftrightarrow \begin{pmatrix} v_a \\ v_b \end{pmatrix} = \boldsymbol{J} \begin{pmatrix} e_a \\ e_a \end{pmatrix} . \tag{2.3}$$

Where $\boldsymbol{J}$ is a 2×2 matrix known as a Jones matrix which takes into account all the propagation effects (corruptions) which the signal undergoes from source to antennas (Smirnov, 2011). This is the fundamental linear relationship between the data received (voltages converted to data) from the signal at some distant source. Each corruption has its own unique $\boldsymbol{J}$ term. Therefore, the $\boldsymbol{J}$ actually represents the cumulative product of all the corresponding propagation effects. In general:

$$\boldsymbol{J} \doteq \boldsymbol{J}_n \boldsymbol{J}_{n-1} \boldsymbol{J}_{n-2} \dots \boldsymbol{J}_1 \quad \text{where} \quad \boldsymbol{J}_i \boldsymbol{J}_j \neq \boldsymbol{J}_j \boldsymbol{J}_i \, . \tag{2.4}$$

[†] The FoV is the fraction of the sky to which the telescope is sensitive to.

Where J_i represents a unique and specific effect. An example Jones chain $\boldsymbol{J}$ can be seen in Equation 2.2, where $\boldsymbol{J}$ would take the form of $\boldsymbol{J} = \boldsymbol{GKBI}$. The condition on the right of Equation 2.4 is the general non-commuting property of the Jones matrices, and hence, the order in which to apply these effects are important. An arbitrary antenna μ in an array consisting of two feeds a and b will have Jones matrices J_μ for the signal e_μ, and will recover a voltage v_μ:

$$\boldsymbol{v}_\mu = \boldsymbol{J}_\mu \boldsymbol{e}_\mu \Longleftrightarrow \begin{pmatrix} v_{\mu a} \\ v_{\mu b} \end{pmatrix} = \boldsymbol{J}_\mu \begin{pmatrix} e_{\mu a} \\ e_{\mu b} \end{pmatrix} . \tag{2.5}$$

These voltages are then fed into a correlator, which computes the complex correlations $v_{\mu a} v^*_{\nu b}$. This type of calculation is performed for each antenna pair in an array and then compiled using aperture synthesis. The mathematical form of the cross-correlation of two antennas p and q, each with two correlator feeds a and b is a 2×2 visibility matrix, achieved by applying matrix multiplication of their respective voltage vectors $\boldsymbol{v}_p$ and $\boldsymbol{v}_q$:

$$\mathsf{V}_{pq} = 2\begin{pmatrix} \langle v_{pa} v^*_{qa} \rangle & \langle v_{pa} v^*_{qb} \rangle \\ \langle v_{pb} v^*_{qa} \rangle & \langle v_{pb} v^*_{qb} \rangle \end{pmatrix} = 2\left\langle \begin{pmatrix} v_{pa} \\ v_{pb} \end{pmatrix} \begin{pmatrix} v^*_{qa} & v^*_{qb} \end{pmatrix} \right\rangle = 2\langle \boldsymbol{v}_p \boldsymbol{v}_q^H \rangle . \tag{2.6}$$

Where the averaging operation $\langle\rangle$ is done over a time bin of finite small Δt and $(\cdot)^H$ is the Hermitian or conjugate transpose operator. The factor of two is just a matter of convention. If we substitute Equation 2.3 into the last expression of Equation 2.6 we obtain:

$$\mathsf{V}_{pq} = 2\langle \boldsymbol{J}_p \boldsymbol{e}_p (\boldsymbol{J}_q \boldsymbol{e}_q)^H \rangle = 2\langle \boldsymbol{J}_p (\boldsymbol{e}\boldsymbol{e}^H) \boldsymbol{J}_q^H \rangle = 2\boldsymbol{J}_p \begin{pmatrix} \langle e_x e^*_x \rangle & \langle e_x e^*_y \rangle \\ \langle e_y e^*_x \rangle & \langle e_y e^*_y \rangle \end{pmatrix} \boldsymbol{J}_q . \tag{2.7}$$

The complex visibility V can therefore be alternatively described as an operation of all $\boldsymbol{J}$ (expressed as a multiplicative chain) on the original signal. We omit the subscripts p and q for $\boldsymbol{e}$ since this signal is the same signal observed by all antennas. The last bracketed term is the cross-correlation of the signal vector $\boldsymbol{e}$ and can be written in terms of the Stokes parameters I, Q, U and V, which define the source brightness matrix B:

$$\begin{pmatrix} \langle e_x e^*_x \rangle & \langle e_x e^*_y \rangle \\ \langle e_y e^*_x \rangle & \langle e_y e^*_y \rangle \end{pmatrix} = \begin{pmatrix} I + Q & U + iV \\ U - iV & I - Q \end{pmatrix} \equiv \mathsf{B} . \tag{2.8}$$

Where the $e_x e_y$ are the x, y polarisations of the signal $\boldsymbol{e}$. The Stokes parameters describe the polarisation state of light from the source (Shurcliff, 2013). We can now obtain the general discrete (point source) RIME by combining Equation 2.7 into Equation 2.8:

$$\mathsf{V}_{pq} = \boldsymbol{J}_p\,\mathsf{B}\,\boldsymbol{J}_q^H = \boldsymbol{E}_p \boldsymbol{G}_p \boldsymbol{K}_p \mathsf{B} \boldsymbol{E}_q^H \boldsymbol{G}_q^H \boldsymbol{K}_q^H = \boldsymbol{E}_p \boldsymbol{G}_p \mathsf{X}_{pq} \boldsymbol{E}_q^H \boldsymbol{G}_q^H \ . \tag{2.9}$$

Where we have used Equation 2.4 to express $\boldsymbol{J}$ explicitly as a cumulative sum of different effects: $\boldsymbol{J} = \boldsymbol{EGK}$. $\boldsymbol{E}$ represents the DD effects, $\boldsymbol{G}$ represents the DI effects and $\boldsymbol{K}$ is the scalar phase matrix. In the final term, we have absorbed the uncorrupted effect terms, such as source properties B and phase $\boldsymbol{K}$ into a single Jones matrix X called the source coherency.

The sky in general is not a sum of discrete point sources, but rather a continuous distribution of sources as seen by baselines pq in the $uv-$plane described by the visibility $\mathsf{V}_{pq} = \mathsf{V}_{pq}(u, v)$. We obtain the full-sky RIME by taking the integral form of the final term of Equation 2.9:

$$\mathsf{V}_{pq} = \boldsymbol{G}_p \left(\iint_{lm} \boldsymbol{E}_p\, \mathsf{X}(l, m)\, \boldsymbol{E}_q^H \, dl\, dm \right) \boldsymbol{G}_q^H = \boldsymbol{G}_p \left(\iint_{lm} B_{pq} e^{-2\pi i (u_{pq} l + v_{pq} m)} \, dl\, dm \right) \boldsymbol{G}_q^H \ . \tag{2.10}$$

The latter form of the full sky RIME is the 2-D version of Equation 2.2 and is exactly the vCZ equation of 2.1, with the effects of calibration incorporated within. It conveniently encapsulates the two main problems of radio interferometry, calibration (outer terms) and imaging (inner bracketed term).

As elegant as the RIME may be, it unfortunately, does not incorporate all the procedures required to fully recover the original signal and its application therefore currently remains limited to the realms of simulation and calibration. The `MeqTrees` software package was the first to implement measurement equations based on the RIME formalism described here for purposes of simulation and calibration (Noordam & Smirnov, 2010). The method of data-reduction is the current framework in which implements all procedures known to correct data and extract the true signal.

2.3 Radio interferometric data reduction

In the introductory part of this chapter, we showed a schematic diagram of the equipment involved in converting cosmic signals into raw visibility data in Figure 2.1, for a two-element interferometer. We then wrote out an explicit form of the cross-correlation product used to combine the signals in the correlator to form the raw visibilities in Equation 2.6. Eventually, this raw data gets converted into a usable format that can be easily processed. One such format is called a Measurement Set (MS). An MS is a set of tables containing data from the observation(s) and is the input file required for most data-reduction procedures. The raw data inside the MS requires post-processing that involves flagging, calibration and imaging (in that order) before it can become of any use to conduct science. The RIME incorporates the latter two but not the former. Flagging is the process of removing unwanted or bad data. Calibration is the process by which instrumental and atmospheric errors are estimated (in the form of $\boldsymbol{J}$) and corrected. Imaging is the process of turning these corrected visibilities into a representation of the true sky (through application of the vCZ theorem) followed by deconvolution to remove the effects induced by incomplete sampling of the uv-plane. These different steps of data processing can be incorporated into a single famework called a pipeline. A pipeline is a set of commands consisting of nearly all steps of data-reduction that can run with minimal or no user intervention. In the following chapters, we briefly mention the main steps of data-reduction that can be run within pipelines.

2.3.1 Flagging

The observed bandwidth of telescopes has dramatically increased over the last decades. Modern telescopes in radio astronomy such as ASKAP, LOFAR, the Jansky Very Large Array (JVLA) (Selina et al., 2018) and MeerKAT have observable bandwidths that often overlap with other parts of the radio spectrum not reserved for radio astronomy. At the same time, technological advancement has consequently brought an increased number of man-made radio transmitters. The signals emanating from these transmitters have been affecting radio astronomy more and more over the years, particularly due to the increasing sensitivity of observations. This has caused the reserved radio spectrum to be significantly populated with a variety of signals resulting in crowding (Pankonin & Price, 1981), which are generally unwanted. The unwanted man-made signals are often several orders of magnitude stronger than the weak astrophysical signals of interest and consequently, negatively affect radio observations producing various interferences within the data. These types of interferences are termed radio-frequency interference (RFI). RFI tends to affect multiple neighbouring samples in the time-frequency domain of the data. In a so-called 'waterfall plot', RFI will manifest itself in the form of straight-line artefacts parallel to the time and frequency axes. These common RFI signatures are shown in the waterfall-plot of Figure 2.3. The procedure used to mitigate RFI or suppress these artefacts in the data is called flagging.

Flagging of RFI is applied in two different stages: (1) before data is correlated, such as pre-correlation flagging and (2) after data is correlated, such as post-correlation flagging. Pre-correlation flagging does not involve the user and is handled by the system electronics. It processes large amounts of data over a short period of time (Offringa et al., 2010). The constraints imposed by the hardware imply that only limited dimensions of the data are accessed, such as from a single antenna or a small time/frequency range. Pre-correlation flagging can therefore deal with only the strongest and most obvious RFI. User intervention is necessary to fully mitigate the leftover RFI through post-correlation flagging (Offringa et al., 2012). This takes place at stage (2). This residual bad data is removed during data-reduction either manually or via automation. Increased data volume, sensitivity and the increased contamination of RFI through electronic equipment has led automated RFI flagging methods to be developed and preferred over manual flagging. However, manual flagging must still be done if the automated method has failed in some respect. Examples of automatic flagging strategies include `AOFlagger`[*] and `TriColour`[†]. The `AOFlagger` software implements the morphological technique in conjunction with various statistical methods for RFI detection (Offringa, 2010; Offringa et al., 2012). This software includes various files for several telescopes called flagging strategies that have their own customisation for each telescope in order to optimise the RFI detection accuracy for different

---

[*] `https://github.com/pkgw/aoflagger`

[†] `https://github.com/ska-sa/tricolour/`

Table 2.1: List of MeerKAT known RFI sources for L-band

RFI source	**Frequency range (MHz)**
GSM (Mobile phones)	900-915 (uplink), 925-960 (downlink)
Aircraft Transponders	Multiple intermittent signals between 1000-1200
Global Positioning System (GPS)	1565-1585, 1217-1237, 1375-1387, 1166-1186
Global Navigation Satellite System (GLONASS)	1592-1610, 1242-1249
Galileo global navigation system	1191-1217, 1260-1300
Afristar satellite	1453-1490
Iridium satellite constellation	1616-1626
International mobile Satelite Organisation (Inmarsat)	1526-1554
Alkantpan military testing site	1600

band-pass shapes, time/frequency resolutions, and FoV of these different telescopes. `Tricolour` is a highly configurable and parallel software that implements the Sum-Threshold and MAD statistical methods widely used for detection of interference. In Table 2.1 we show the major RFI contaminated regions of L-band for MeerKAT.

2.3.2 Calibration

Apart from corrupted data resulting from the signals induced by man-made instruments (RFI), the signal from our target source undergoes a series of distortions or corruptions that are induced by various instrumental and atmospheric effects. These are removed by the process of calibration. The calibration procedure in theory derives a series of complex scaling factor $\boldsymbol{J}$ terms or corrections based on the difference between a skymodel (model visiblity), created from previous observations to that of the real observed visibilities of the source. The scaling factors selected are the ones that minimize the following function:

$$\chi^2 = \sum_{pq} ||\boldsymbol{D}_{pq} - \boldsymbol{J}_p \boldsymbol{M}_{pq} \boldsymbol{J}_q^H|| \ . \tag{2.11}$$

Where $\boldsymbol{D}$ is the observed visibility, $\boldsymbol{M}$ is the model visibility and $|| \cdot ||$ is the norm. From

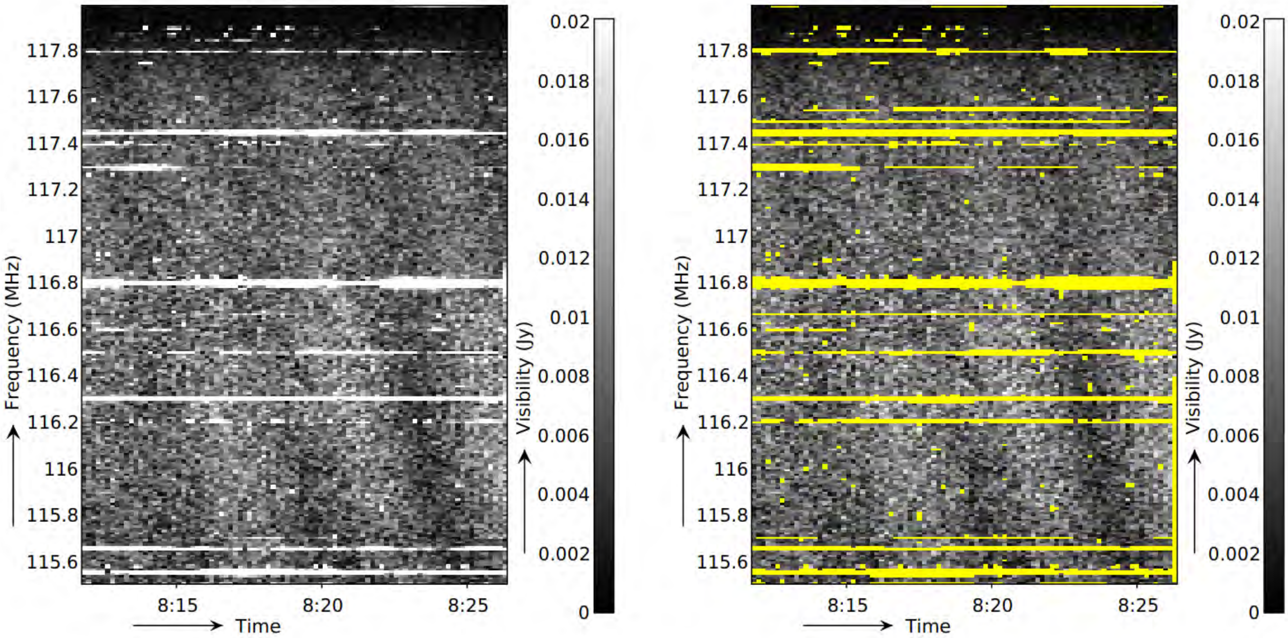

Figure 2.3: Typical RFI features of raw data and how flagging strategies generally remove them. *Left*: An example of unflagged WSRT data clearly showing the typical spectral line RFI features in a small bandwidth over a short time interval. *Right*: The same original data after application of the `AOFlagger` automated flagging strategy.

these differences, we can derive how the original signal was affected and what transformations need to be applied in order to minimise this difference. Following Noordam & Smirnov (2010), we recognise three stages of calibration, namely 1st generation calibration (1GC), 2nd generation calibration (2GC) and 3rd generation calibration (3GC). From the full sky RIME of Equation 2.10 in §2.2, we classify 1GC and 2GC calibration techniques as DI effects that are intended to solve for $\boldsymbol{G}$, while 3GC calibration techniques are DD and are implemented to eliminate the inner source-specific $\boldsymbol{E}$ terms. Figure 2.4 uses an oversimplified diagram to show these effects.

2.3.2.1 1st generation calibration (1GC)

1GC, also known as cross-calibration, makes use of calibrator fields (well-studied sources with known flux, shape, and spectral behaviour) to derive the response of an instrument. It is used to

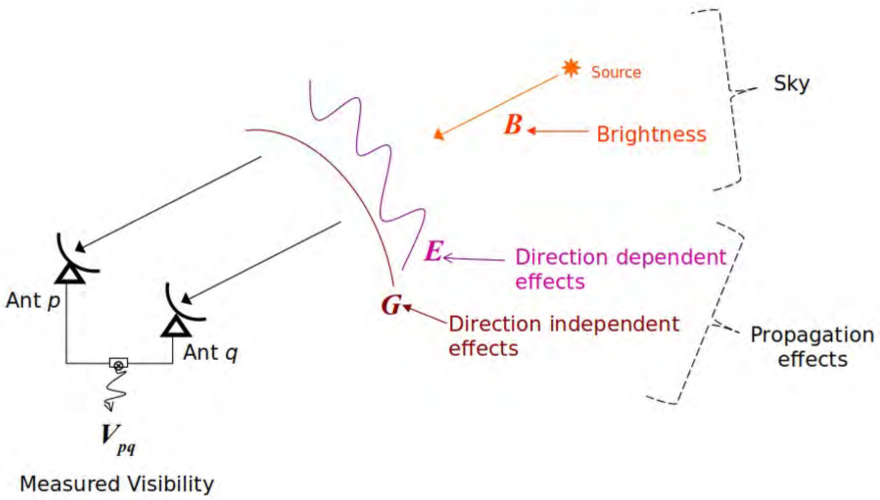

Figure 2.4: An oversimplification of the calibration scheme for interferometry. DI $\boldsymbol{G}$ and DD $\boldsymbol{E}$ both vary with time and frequency, but $\boldsymbol{E}$ effects additionally vary with direction while $\boldsymbol{G}$ effects do not. We visually show this property with a curved and smoothed line, respectively.

determine the complex gain solutions or scaling factors that are required to calibrate the target field. These scaling factors are determined by observing various calibrator fields. These sources are observed repeatedly during an observation, as the telescope switches between them and the target source. The target source is observed for the longest ($\sim$ 30 minutes) and the calibrator fields are observed for a much shorter duration ($\sim$ 2-5 minutes). Below we describe the usage of calibrators in order to obtain the calibration:

- Amplitude/Flux calibration: This calibration performed by observing a primary calibrator. The primary calibrator is used to scale the fluxes of the visibilities to their true values. The primary calibrator must be a very bright and unresolved source in order to obtain a high Signal to Noise Ratio (SNR) in the shortest time possible to reduce the time spent on this source. It need not be close to the target source. It is usually observed for about $\sim$

3-5 minutes at the beginning, middle and end of an observation, as the amplitude scale is assumed to have little variability. For a typical MeerKAT observation, two southern sky calibrators are available for the primary calibrator, J1939-6342 and J0408-6545 [†].

- Complex gain calibration: This calibration is performed by observing a secondary calibrator. The secondary calibrator is used to track gain (in particular, gain-phase) variations with time. Information from this calibrator must be interpolated to the target source. Error in this extrapolation grows with increasing distance which means this source must either be selected near the target, or be observed more densely via shorter time cycles or both. This source is therefore observed many times in a loop with the target source. A single scan on this calibrator is typically $\sim$ 2 minutes.

- Bandpass calibration: This calibrator is observed to correct for the frequency response of the instrument. An ideal Bandpass calibrator has similar properties to that of the primary calibrator and in addition, must have an accurately known spectrum. It is common practice to use the same source for bandpass and flux calibration.

From 1GC calibration, we obtain complex gain solutions which we apply to our target source. We then perform imaging (including deconvolution) to obtain the 1st order skymodel.

2.3.3 Imaging

We have already stated the response of a two-element interferometer in §2.1 (Equation 2.1) through application of the vCZ theorem to radio astronomy. The geometrical setup of the vCZ theorem for radio interferometric observations was also schematically shown in Figure 2.2. This essentially expresses the task intended for imaging algorithms. At its simplest, imaging is the process of transforming the complex visibility samples V into a true representation of the sky I. We can omit the w term in Equation 2.1 to clearly show this. The w term is the component of the baseline along the line of sight to the phase and delay tracking centre. During an observation, an

---

[†] Details of these calibrators are found here: `https://skaafrica.atlassian.net/servicedesk/customer/portal/1/article/1481408634`

interferometer continuously adjusts the delay and phase signals to compensate for this changing w. The w term removal can be justified by assuming one of these two properties:

1. Small FoV

   For a small FoV, the projection of sampled points from the (u, v) plane onto the celestial sphere (l, m) does not vary significantly for a range of sky angles. This is because, intuitively, for a relatively small region on a sphere the curvature is approximately constant. This can be seen for the shaded ellipses (A and B) on celestial sphere on the left of Figure 2.2. For these regions, the celestial sphere of the sky translates to $n = \sqrt{1 - l^2 - m^2} \approx 1$, and the w can thus be ignored:

$$\forall w, l, m : w(\sqrt{1 - l^2 - m^2} - 1) \ll 1, \text{ valid for small FoV.} \tag{2.12}$$

2. Coplanar baselines

   If the ensemble measurements represented by the visibility function are collected by an array in a plane parallel to Earth's equatorial plane, for example, confined to either east-west or north-south, then a coordinate transformation of $w = au + bv$ can be performed, thereby allowing the 3rd variable in $V(u, v, w)$ to drop out.

By excluding the w term and beam effects (for further simplicity), we can rewrite Equation 2.1 as:

$$V(u, v) = \int_{-\infty}^{+\infty} \int_{-\infty}^{+\infty} I(l, m) e^{-2\pi i(ul+vm)} dl dm \ . \tag{2.13}$$

Equation 2.1 has now reduced to a familiar 2-D Fourier relationship between the visibility function and sky brightness, thus providing a clear way to extract the true image. In reality, the Fast Fourier Transform (FFT) is usually used in conjunction with a gridding routine, which interpolates the uv points on an evenly spaced finite grid for application of the FFT. The irregularly sampled uv-domain is the result of the irregularity of scans in an observation.

Unfortunately, Equation 2.13 captures only half of the imaging problem, because the resultant image from Fourier inversion of Equation 2.13 will only give a correct image for the complete sampling of the uv-plane, which in reality, is not possible. Incomplete sampling of the uv-plane is unavoidable due to the finite number of antennas in an array. Observations only obtain noisy samples of the visibility function at discrete locations in the Fourier plane. The incomplete sampling of the uv-plane gives a synthesised beam response with many sidelobes called the dirty beam or Point Spread Function (PSF)[‡] due to the response from empty/non-sampled regions. After Fourier transforming the visibilities, this dirty beam is simultaneously convolved with the sample measurements at every point, resulting in a blurred image called the dirty image (Taylor et al., 1999; Thompson et al., 2004). Deconvolution algorithms attempt to extract the true image from this dirty image.

2.3.3.1 Deconvolution

The deconvolution process attempts to give reasonable values to the empty regions in the Fourier plane that have not been sampled and remove the associated sidelobes of the dirty beam that have manifested in the dirty image. The problem is to extract the true image I (true sky brightness) from knowledge of the dirty image I^D (measured sky brightness) and the PSF B:

$$I^D(l,m) = I(l,m) * B(l,m)\ . \tag{2.14}$$

Where $*$ is the convolution operator. The extraction of the true image from the dirty beam is a deconvolution problem, which deconvolution algorithms attempt to solve. The most widely used deconvolution method in radio interferometry is the CLEAN algorithm originally formulated by Hogbom (Hogbom & Brouw, 1974; Cornwell, 2009) and variants thereof (Zhang et al., 2020). The CLEAN variants have become the workhorse of radio interferometric imaging and usually consist of two cycles namely, the major cycle (performed in the visibility plane) and the minor cycle (performed in the image plane) (Taylor et al., 1999; Thompson et al., 2017). The original Hogbom CLEAN has only minor cycles. The main basis for these algorithms is the assumption that most sources can be represented by combinations of point-like sources described by δ

[‡] The PSF is related to the geometry of the array configuration and is how the array samples the uv domain. The full side lobe pattern of the PSF results from the incomplete sampling.

functions. The CLEAN algorithm uses an iterative approach to decompose the sky brightness $I^D(l, m)$ into point-source responses and replaces each one with the corresponding response to a beam free of sidelobes called a clean beam. The flux densities and positions of the replaced point sources are called the CLEAN components. This iterative algorithm works as follows:

1. Initial input:

   The starting ingredients for deconvolution are the PSF B, dirty image I_D and an all-zero model M^P for the point sources. This model will be used to record the position x_q, y_q and flux I_q of point sources and could take the form of:

   $$M^P = \sum_{q=1}^{N} I_q \delta(x - x_q)\delta(y - y_q) \ . \tag{2.15}$$

2. Population of the model and updating of the residuals:

   The points with the highest intensity on the dirty image are subtracted by the PSF centred on that position. The resultant image after this subtraction is the residual image R. The position and flux density of the subtracted sources are recorded and added to the model of Equation 2.15. The procedure repeats for all point sources N, with each subsequent iteration utilising the previous residual to find the remaining sources in order to perform the subtraction. The model is continually updated in the process. With each iteration, the model contains more sources and the residual contains fewer sources. This process can be summarised as:

   $$\begin{aligned} R(1) &= I_D - B * M^P(1) \\ &\vdots \\ R(N) &= I_D - B * M^P(N) \end{aligned} \tag{2.16}$$

   Where $M^P(N)$ and $R(N)$ is the model and the residual formed after subtraction of the last source N.

3. Termination of the algorithm:

The procedure terminates (limit of N is set) when a user-defined maximum number of iterations is exceeded or when a user-defined maximum threshold for the brightest source in the final residual image falls below a certain value.

4. Obtaining CLEAN image from the final products of (3):

   The final residual image $R(N)$ makes up the background component of the image (mainly composed of noise) while the final model $M^P(N)$ encodes the sources or the foreground component. By taking the final residual $R(N)$ and adding it to the final model $M^P(N)$ convolved with a Gaussian PSF (clean beam), we obtain the final CLEAN image:

   $$\mathcal{I}^{CLEAN} = G * M(N)^P + R(N)\ . \tag{2.17}$$

   Where $\mathcal{I}^{CLEAN}$ is the resultant clean image, the final model $M^P(N) = \sum_n^N M^P(n)$ is the sum of all point source components and G is the Gaussian PSF.

We have shown that after removal of the w term, the imaging problem consists of two parts namely, Fourier inversion of Equation 2.13 and deconvolution of Equation 2.17. We have demonstrated that the latter problem utilises the CLEANing process, which is a rather straightforward procedure. However, due to the properties attributed to the current- and next-generation telescopes, the removal of the w term is not so straightforward. These newer telescopes include properties that are in direct contradiction to the properties of List 2.3.3 of §2.3.3, such as large FoV and non-coplanar baselines. For large FoV, noticeable image degradation from the phase error is induced if the w term is ignored (Cornwell & Braun, 1989). For non-coplanar arrays, no simple transformation exists to eliminate the w term. This leads to the current general imaging problem, and as a result, standard methods of image reconstruction cannot be solely utilised, leading to the development of more elaborate imaging techniques.

2.3.4 Advanced calibration

After applying the derived solutions of 1GC in §2.3.2.1 to the model visibility that optimize Equation 2.11 of §2.3.2, a 1st round of imaging is performed that gives rise to a 1st order skymodel. Further calibration is usually required as either, (a) good calibrator fields might not exist close to the target or (b), since the calibrator and target fields are observed in different scans, rapid gain fluctuations are not captured by the 1GC solutions. We, therefore, have to perform further calibration by the use of 2GC techniques, and sometimes even 3GC techniques.

2.3.4.1 2nd generation calibration (2GC)

2GC, also called self-calibration (self-cal) is an iterative calibration algorithm in which the target source is used to calibrate itself (Pearson & Readhead, 1984). It assumes instrumental effects are constant over the entire FoV, associating a single DI complex gain term (which can have a complicated behaviour in frequency and time) with each antenna of the interferometer (Smirnov & de Bruyn, 2011). It is most successful at calibrating relatively narrow fields with a single dominant source of emission. By alternating between calibration and imaging over a certain number of iterations, it can successively refine the model of the target field. The procedure is summarised in Figure 2.5. It begins with an initial model, that is either based on previous observations or from a dirty uncorrected image made after 1GC. After each iteration, a new model is created from the previous corrected image and calibrated (parameters of the RIME are optimised to minimize Equation 2.11 and the solutions are applied to the model) to match the real data. This loop repeats itself until a fixed number of iterations or threshold (SNR limit) have been reached. Once the model visibilities are corrected for, they are imaged to form the final 2GC calibrated image.

2.3.4.2 3rd generation calibration (3GC)

The previously mentioned properties attributed to modern telescopes have introduced a host of new subtle instrumental effects that have become a limiting factor in achieving high-quality images. These effects need to be dealt with if we wish to reach the thermal noise and take full advantage of the capabilities offered by these new instruments. 2GC calibration techniques alone are not sufficient to limit these effects, since they take only DI effects into account. 2GC calibration techniques can only determine one phase correction per antenna per time interval for

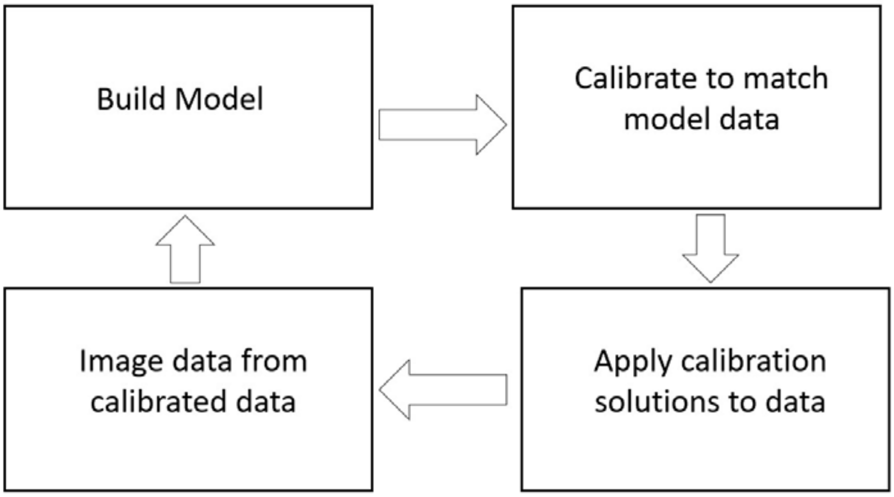

Figure 2.5: A flow diagram demonstrating the iterative procedure of self-calibration as a cycle starting from 'Build Model'. Several runs of this cycle will generate the final 2GC-calibrated image.

the entire FoV. 3GC or DD calibration refers to the family of techniques used to treat direction-dependent calibration effects (DDEs). DDEs are effects that vary across the FoV as well as between antennas (Smirnov & de Bruyn, 2011). The most important DDEs include variations in the primary beam/sensitivity pattern of each antenna and the ionosphere (Lonsdale, 2005; Intema et al., 2009).

The rotation of the primary beam pattern corresponds to the rotation of the sky overhead. This rotation is intrinsic to the alt-azimuthal mounts employed on modern arrays. During an observation, this rotation causes severe baseline, time and frequency variable DDEs that manifest themselves as artefacts in the image. These artefacts are visually noticeable by the concentric-like noisy pattern they produce around sources, whose intensity decreases with distance from the source.

These artefacts are specifically prominent around bright sources in the observed field and even more so for off-axis bright sources that fall into the antenna side lobes. They can potentially hamper the detection of faint and diffuse emission as well as imaging of target source(s) at the phase centre. Examples of such artefacts are shown in the left panels of Figure 2.6, arranged from smaller FoV (top) to larger FoV (bottom). The artefact pattern depends on dish geometry and array configuration. The right panel shows the results after DD calibration solutions have been applied to the 2GC calibrated image (left), forming the final calibrated 3GC image.

2.4 Imaging and calibration software

The RIME formalism in §2.2 is clear through Equation 2.10; the imaging and calibration process can be thought of as two aspects of the same optimisation problem. The unification of these historically separate problems has become clearer through recent developments and understanding of 3GC. Elaborate image reconstruction techniques have already replaced some traditional functions of calibration (Rau et al., 2009). This has consequently promoted the development of fast and sophisticated imaging and calibration algorithms paving the way for newer software. The newer imaging software discussed in the next subsection attempts to take into account the problematic w term during the imaging procedure, while the calibration software places special emphasis on taking into account the newer DD calibration effects.

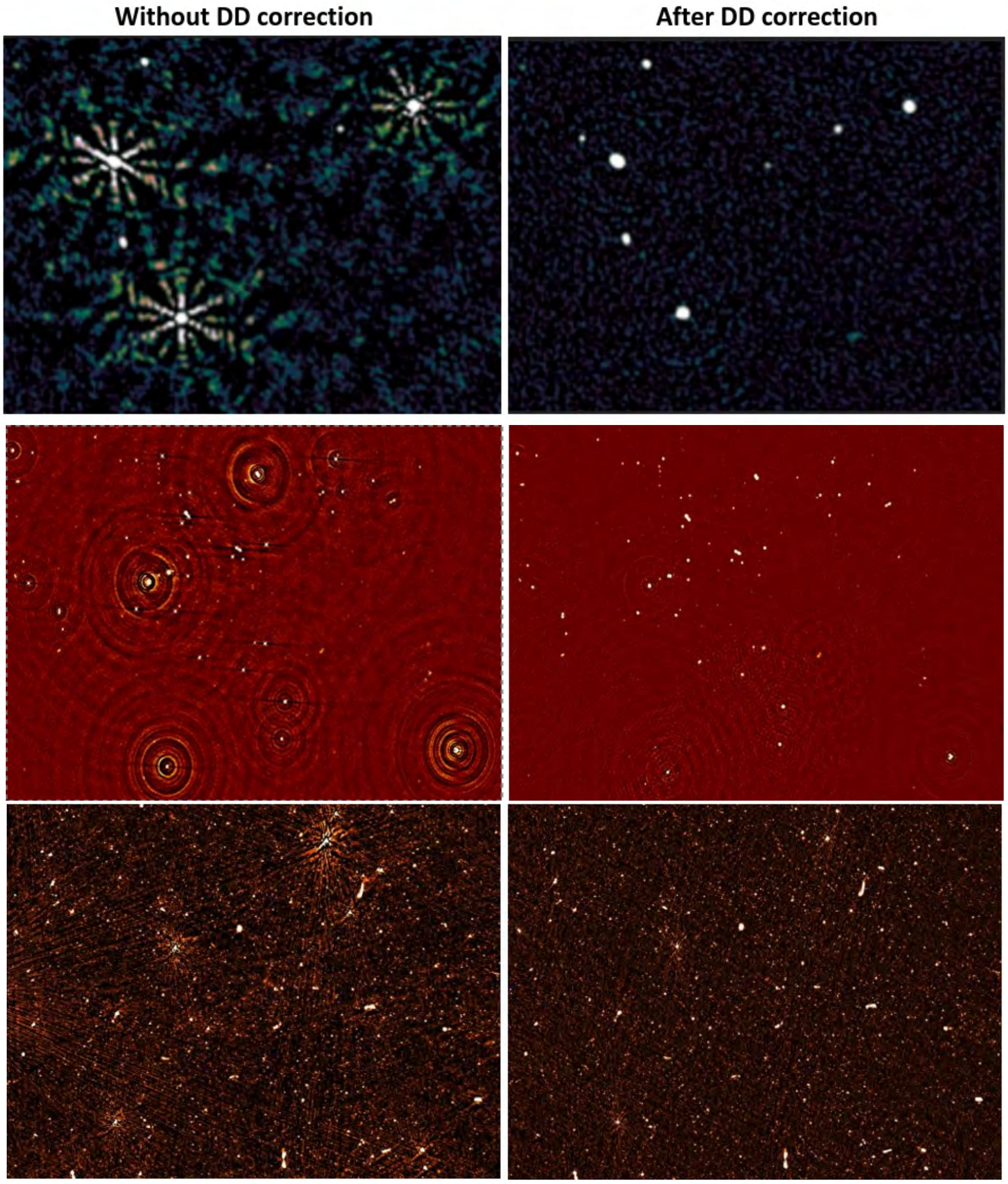

Figure 2.6: Before and after DDE corrections for different observations of increasing FoV going from top to bottom. Top, middle and bottom images are examples of VLA, WSRT and GMRT data, respectively (Tasse, 2014).

2.4.1 WSClean: W-Stacking based cleaning

W-stacking cleaning (`WSClean`)* is an imaging software package written in C++ that makes use of the W-stacking technique for taking into account the problematic w term (Offringa et al., 2014). It can efficiently deal with large volumes of wide-field interferometric data from modern many-element arrays. The W-stacking technique considers several uv-grids of constant w in the form of w layers onto which the visibilities are separately gridded. After gridding, the inverse FT is applied to each individual plane and a w correction is applied once all these individual grids have been stacked. This is an alternative approach to the well-known W-projection algorithm (Cornwell et al., 2008). In W-projection, each uv-sample is convolved with a w-term correcting kernel and FFT is applied on the final result. The W-stacking technique exploits the fact that multiplication of each pixel is generally much faster than convolving an image. There is therefore a trade-off between these two techniques: W-stacking spends more time doing the FFTs, instead of gridding and convolving, therefore, requiring more memory; for W-projection, the opposite is true and thus is more reliant on CPU power. `WSClean` supports the Hogbom and Cotton-Schwab (Schwab, 1984) deconvolution cleaning algorithms, as well as multiscale CLEAN (Cornwell, 2008), and can also deconvolve polarised signals in a joint approach. The W-stacking technique can be summarised using the following equation:

$$\frac{I'(l,m)(w_{max}-w_{min})}{\sqrt{1-l^2-m^2}} = \int_{w_{min}}^{w_{max}} e^{-2\pi i (w\sqrt{1-l^2-m^2}-1)} dw \int\int V(u,v,w)\times e^{-2\pi i(ul+vm)} dudv \ . \tag{2.18}$$

Where $I'(l,m) = I(l,m)A(l,m)$, w_{min} and w_{max} are the minimum and maximum values of w, receptively. We can arrive at this equation by considering the vCZ theorem of Equation 2.1 and perform the following steps: 1) Invoke the small w term approximation of Equation 2.12 to make Equation 2.1 a FT equation, 2) Rewrite Equation 2.1 as an Inverse FT for $I'(l,m)$, 3) sum over all w terms. We can rewrite Equation 2.18 in a more practical way by replacing the integrals with a sum:

---

*https://gitlab.com/aroffringa/wsclean

$$\frac{I(l,m)(w_{max} - w_{min})}{\sqrt{1-l^2-m^2}} = \sum_{w_{min}}^{w_{max}} e^{-2\pi i(w\sqrt{1-l^2-m^2}-1)} \sum_{u_{min}}^{u_{max}} \sum_{v_{min}}^{v_{max}} V(u,v,w) \times e^{-2\pi i(ul+vm)} . \quad (2.19)$$

From this discrete form we can theoretically describe how the W-stacking method reconstructs the dirty image from the sky brightness:

1. Determine the number of planes, N_w in which to uniformly distribute w layers along the w axis from w_0 to w_{N_w-1}.
2. Assign visibilities $V(u_i, v_i, w_i)$ with different w_i values to the w plane corresponding to the w_i value of that plane or rounded to the nearest w_i value corresponding to a nearby plane (nearest neighbour).
    (a) For each w_i layer, visibility data with the same w value are re-sampled on a uniformly spaced grid (gridding) and then subsequent inverse FFT (double sum in Equation 2.19) to map the data onto the lm-plane;
    (b) Applying the DD phase shift term $e^{2\pi i w(\sqrt{1-l^2-m^2}-1)}$.
3. Repeating the above for all w layers, N_w and adding the results.
4. Applying the final scaling $\sim (w_{max} - w_{min})/\sqrt{1-l^2-m^2}$ after adding.

The final scaling $\sim (w_{max} - w_{min})/\sqrt{1-l^2-m^2}$ will be different in practice, since individual w layers will not be completely sampled with data. Each pixel will therefore need to be divided by the weighted number of samples in that layer. We have shown a schematic diagram in Figure 2.7 of this W-stacking technique.

`WSClean` is run through the command line. All parameters can be accessed through the `WSClean` help file called by `wsclean --help` in the command line. Performance options include `-j` and `-mem` for the number of cores and memory use, respectively. Imaging options include image size `-size`, number of iterations `-niter`, auto masking `-auto-mask` and cleaning threshold `-threshold`. `WSClean` supports natural, uniform and Briggs (Briggs, 1995a,b) weighting schemes through the `-weight` option. The robust parameter for Briggs weighting is set by `-weight briggs` and its values range from -2 to 2. Various tapers[*] such as a Gaussian taper and Tukey taper can be specified through `-taper-gaussian` and `-taper-tukey`, respectively.

One of the unique features of `WSClean` is its wideband multi-frequency deconvolution mode for joint channel cleaning of multiple MSs. This can be implemented through using both the `-join-channels` and `-channels-out` options. `WSClean` calculates the full available bandwidth (over all MSs) and splits them into chunks/subbands (divided by `-channels-out`) with the same amount of input channels. Each subband is deconvovled separately and combined into a multi-frequency synthesis (MFS) map through the joined-channel deconvolution mode (`-join-channels`) of `WSClean`. This algorithm produces similar results to `CASA`'s multi-frequency deconvolution algorithm (Rau & Cornwell, 2011), but is orders of magnitude faster. `WSClean` also supports multiscale cleaning (Offringa & Smirnov, 2017). Multiscale cleaning models sources as extended objects, composed of various different sized scales. It has better accuracy when imaging diffuse sources. This option can be turned on with `-multi-scale` and is often used together with the multi-frequency deconvolution mode.

2.4.2 DDFacet: A facet based imager

`DDFacet`[†] is an imaging software (Tasse et al., 2018) written in C and Python that makes use of the polyhedron imaging technique (Cornwell & Perley, 1992) to deal with DDEs (including primary beams, DD gains, and the problematic w term) during imaging. This technique exploits the 2-D FT approximation for small FoV's by approximating the full-sky with many suitably small FoV's, called facets. It does so by decomposing the image into a regular grid of squares satisfying the FoV approximation of Equation 2.12. Each square is a facet and a solution is

---

[*] Tapering is a weighting tool used to reduce the influence of long baselines (the largest uv spacings) by suppressing the sidelobes caused by incomplete sampling on the longest baselines. The shape of the beam is improved at the expense of spatial resolution.

[†] `https://github.com/cyriltasse/DDFacet`

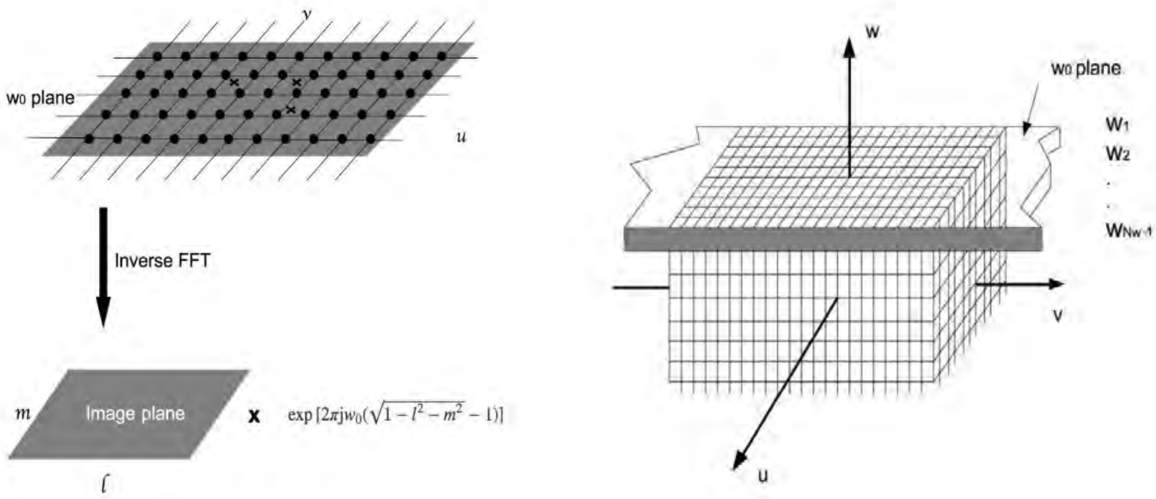

Figure 2.7: Schematic representation of the important steps of the W-stacking technique described in List 2.4.1. *Left*: Schematic representation of (2) in List 2.4.1, showing how a strip (single w layer) of image space lm (bottom image) is reconstructed from a strip of visibility space uv (top image). The $\boldsymbol{x}$'s on the uv plane (three shown) represent real uv measurements and the evenly spaced block dots represent gridded visibilities for application of the FFT (Equation 2.19) to produce the image slice. *Right*: The final stages of the W-stacking technique described in (3) and (4) in List 2.4.1. After all visibilities are assigned, gridded and FFT to a finite number of w–planes N_w, these planes are stacked along the w axis ranging from w_0 to w_{N_w-1} to produce the final image (Ye, 2019).

applied to each one during calibration. The final image is a sum of the solutions applied to each facet. The centre point of each facet is chosen to be the brightest source or group of sources in the area of the facet. An example of this faceting structure is shown in Figure 2.8. The regular grid of squares representation of facets used by `DDFacet` is shown on the right panel at the bottom of Figure 2.10. The general procedure for the faceting technique is as follows:

1. Estimation of the facets:

   The visibility function for this method is obtained by estimating $I(l,m)$ for several points on the celestial sphere. A localised small region (facet) surrounds each point and thus all the points approximate the celestial sphere as a celestial polyhedron. Each narrow-field facet is tangent to the celestial sphere at its own phase centre. For a given direction (l_0, m_0, n_0), the visibility function is obtained by phase rotating to each point:

$$V_{PR} = V(u, v, w)e^{2\pi i[u(l_0-l)+v(m_0-m)+w(n_0-n)]} \ . \tag{2.20}$$

For each phase rotation in a direction (l_0, m_0, n_0), the (u, v, w) spatial coordinates must be recalculated and the sky brightness $I(l_0, m_0)$ can be obtained from the 2-D transform of V_{PR} with respect to the projected coordinates of (u_0, v_0). At this point, a solution is also applied to the visibilities that may include primary beam effects.

2. CLEANing of each facet:

   The effect of incomplete sampling still persists for small FoV and therefore the problem of deconvolution must still be tackled. The CLEANing procedure required to do this is essentially the same as the one described in the numbered list of §2.3.3.1, except now it has to deal with many smaller images (facets). The PSF is also slightly different for each facet.

   After estimation of the facet in (1), the local PSF is used to deconvolve the brightness on that facet, which is followed by subtraction from the overall visibility forming a residual polyhedron. The PSF side lobes do not include emission from other facets and must therefore stop at some threshold. The resulting residual polyhedron is then used to carry on the deconvolution for the remaining facets in a manner equivalent to Equation 2.16.

3. Combining the result:

   After a sufficient number of cycles of (1) and (2) set by some user-defined maximum threshold or number of iterations that take into account all facets, the deconvolved images for each facet are combined into a single image. A coordinate re-projection must be performed once for each facet before they are added, taking into account their varying geometry. All the solutions are then smoothed over to prevent sudden changes in the image across facet borders.

Consideration to the artefacts in an image (see left of Figure 2.6) from DDE are simultaneously taken into account during `DDFacet` imaging by the use of a different PSF for each facet (step (2) in List 2.4.2). DDEs cause the effective PSF to vary with direction, which violates the shift-invariant PSF assumption of the CLEAN algorithm. Normal imagers use the ideal PSF for cleaning and ignore this difference. The artefacts are essentially the difference between the ideal PSF used for cleaning, and the ‘distorted’ PSF that is there due to the DDE. By using a different PSF for each facet, `DDFacet` effectively takes this difference into account.

`DDFacet` can be run through the command line or through a parset file*. A complete list of all parameter’s can be found by invoking the `DDFacet -h` in the command line. We have shown in Appendix §G an example `DDFacet` parset file including some of its options. `DDFacet` supports a variety of deconvolution algorithms, specified through the `-Deconv-Mode` option, which are all variants of, and including, the CLEAN algorithm. It additionally includes a new algorithm called sub-space deconvolution (SSD), through `-Deconv-Mode SSD`. In SSD, regions with bright point sources are processed in parallel. In the first step, these regions (also called islands) are isolated and deconvolved independently from one another. In the 2nd step, all these models are combined and subtracted from the visibilities, which are then re-imaged. Corrections applied to a single island are all applied to other islands resulting in fast convergence over multiple iterations.

The skymodel (facet-based) used in `DDFacet` during deconvolution is described by a .DicoModel file. To use a skymodel from another or previous run, one would invoke the option `-Predict-InitDicoModel`. `DDFacet` has a number of options for constructing the most suitable polyhedron from the corrected data in which these deconvolution algorithms can be applied to. The total number of facets for the celestial polyhedron representation of the image is chosen with `-Facets-NFacets`; this is used in conjunction with `-Facets-DiamMax` and `-Facets-DiamMin` to set the maximum and minimum facet size, respectively. The number of pixels in an image and the cell size are chosen by `-Image-NPix` and `-Image-Cell`, respectively. The same weighting schemes are supported as with `WSClean` through `-Weight-Mode`, including Briggs robust weighting through `-Weight-Robust`. `DDFacet` comes with a list of beam files for various beam

---

*A parset file is a single configuration file listing all possible options available for the software. The user selects the options in which to modify instead of specifying them on the command line.

models through the option `-Beam-FITSFile`, to accurately model the beam pattern ($A(l,m)$ in Equation 2.1 of §2.1) of the specific instrument in use. Currently supported beams include GMRT, MeerKAT, LOFAR, and so forth. Masking is also supported either externally with `-Mask-External` or internally with `DDFacet` through `-Mask-SigTh`.

One of the unique features of `DDFacet` includes its ability to save the intrinsic and apparent component of any image from the image process. These are produced by indicating an upper case or lower case letter for the intrinsic and apparent components, receptively. For example, `-Output-Images DdRrIi` option will output intrinsic and apparent images for dirty (Dd), residual (Rr) and restored images (Ii), respectively.

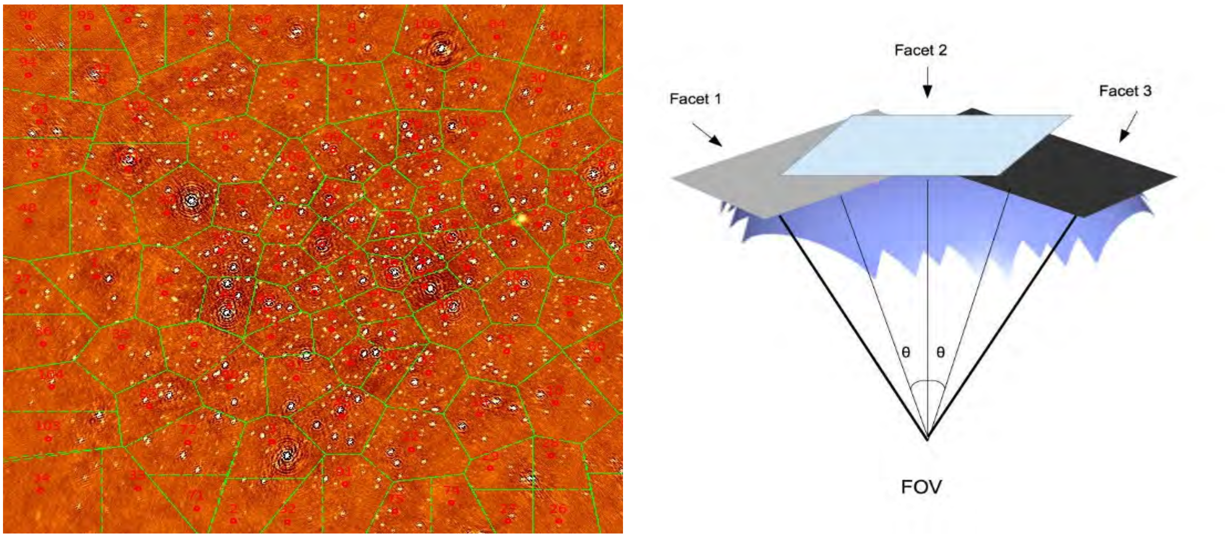

Figure 2.8: The faceting framework. *Left*: A wide FoV image of the Bootes field that has been split up into many facets shown by the green shapes, all satisfying the small w approximation. *Right*: How an observer would see the faceting framework when looking up into the sky. The thick black lines represent the entire FoV, which in this example, is divided into three smaller FoV represented by the three facets, Facet 1,2 and 3. The angle θ shows a $\pm\theta$ displacement of the centre of Facet 1 and Facet 3 from the phase centre which is the centre of Facet 2 (Tasse et al., 2018; Ye, 2019).

2.4.3 killMS: facet-based calibration

`killMS`[*] is the companion package to `DDFacet`, mainly written in C and Python, that performs DD self-calibration based on a model or image, using the Wirtinger formalism applied to the non-linear optimisation problem in the context of calibration (Tasse, 2014). This has transformed the traditional non-linear least squares (NLLS) problem of calibration into a separable non-linear complex-optimisation problem. This ultimately allows exploitation of algorithmic shortcuts to simplify calibration and overall speeding up of the calibration process. This has paved the way for the development of many new algorithms and gain solvers.

`killMS` implements two very efficient algorithms for solving the DD calibration problem, namely the Jones based solver (Complex Half Jacobian optimisation (CohJones)) and a physics-based solver (non-linear Kalman Filter (KAFCA)). The calculations made by `killMS` are performed in parallel for directions and stations. These calculations are performed by several workers called worker pools, working from a job queue with each worker using a single core. `killMS` works in conjunction with `DDFacet` to perform the calibration during imaging. Both softwares make use of shared memory for the communication of data and results for different processes (van Hateren, 2019). The `DDFacet` and `killMS` architecture and typical run are shown in Figure 2.9.

The facets constructed from `DDFacet` composing the image form all possible directions in which `killMS` can perform the calibration. Ideally, one would perform the calibration for every source (each facet) in the field. However, individual facets contain insufficient SNR to properly perform the calibration. Utilising every facet is also be computationally expensive. Instead, only a subset of the sources are calibrated for. `killMS` splits the sky into polygonal tessels (tessellation of the image) that depend on the bright source distribution of the image. Each tessel defines a subset of sources that are typically larger than the facets. The combined signals from all sources within a tessel give sufficient SNR to perform calibration. `killMS` takes the `DDFacet` output image and estimates a solution ($\boldsymbol{J}$ term) in directions defined by each tessel. A solution is then ‘associated’ with the centre of each tessel. `DDFacet` then uses the solution from the tessel whose

---

[*] https://github.com/cyriltasse/killMS

centre is nearest to the centre of each facet. The top right of Figure 2.10 shows typical tessel geometries. The bottom right of Figure 2.10 shows how the polygonal tessel and facet differ.

The tessellation of an image is first achieved by choosing appropriate centers located on bright sources using regions defined from the SAOImage `DS9` viewer software[*]. These define the tessel centres. For MeerKAT images, usually 6-10 centres are chosen while for LOFAR ~ 45 are chosen. A utility called `MakeModel` converts the region file to a NumPy (.npy) array file. This file contains the spatial information regarding the tessellation. To apply the tessellation, we put this file into `DDFacet` under the option `-Facets-CatNodes`. The tessel centers define the directions in which calibration will be performed. Figure 2.10 shows two examples of how an image is tessellated (right) from a chosen set of tessel centres (left) using `DS9` region files.

A comprehensive list of all parameters can be found by invoking `kMS -h` in the command line. `killMS` has no parset file and is run through the command line. We have shown in Appendix §G a list of some of the `killMS` options. The solver type options in `killMS` are specified with `-SolverType`. Performance options include `-dt` and `-NCPU` for time-interval for solution (in minutes) and number of cores to use, respectively. The skymodel used by `killMS` is the .DicoModel file created from `DDFacet` and is called using the `-BaseImageName` option. The output solutions are saved in the same folder as the MS and under the name specified under `-OutSolsName`.

The `DDFacet/killMS` software combo is currently being utilised as part of the official processing pipeline (called the DDF-pipeline[†]) for The LOFAR Two-metre Sky Survey (LoTSS) (see Shimwell et al. (2017, 2019) and van Weeren et al. (2020); Tasse et al. (2021) for details and results, respectively). There has also been increased usage of this pipeline for MeerKAT data and a corresponding wiki page[‡] has been created for new users.

---

[*] https://sites.google.com/cfa.harvard.edu/saoimageds9

[†] https://github.com/mhardcastle/ddf-pipeline

[‡] https://github.com/cyriltasse/DDFacet/wiki/Creating-a-MeerKAT-DD-corrected-intrinsic-flux-image-with-DDF-kMS

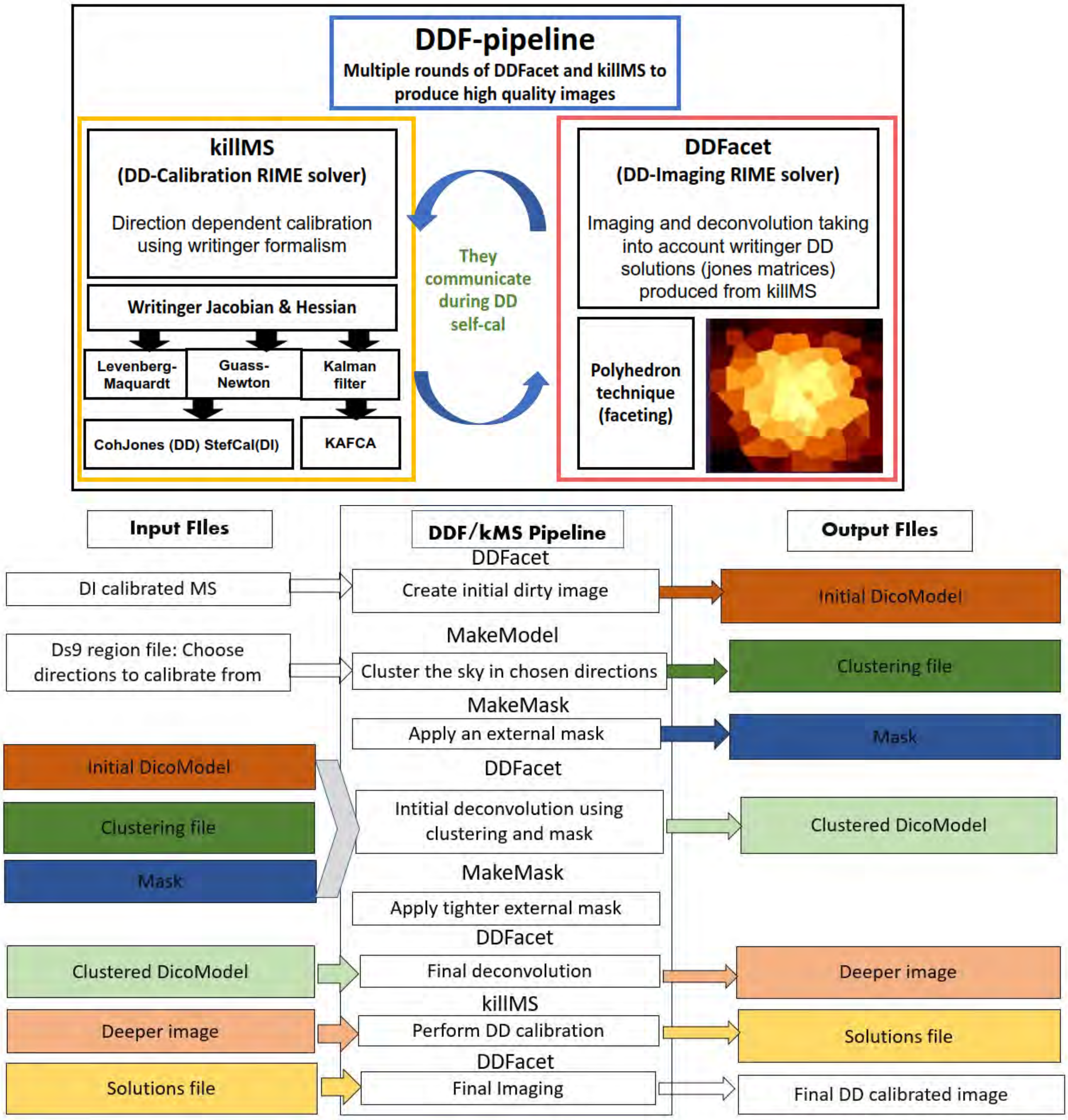

Figure 2.9: `DDFacet` and `killMS` architecture and pipeline. *Top*: The DDF-pipeline architecture showing `killMS` on the left and `DDFacet` on the right. The corresponding optimisation algorithms of `killMS` are shown in the three blocks in the middle that all make use of the Writinger derivative. The associated solver for each algorithm is shown in the last blocks just below. *Bottom*: Typical `DDFacet` and `killMS` run. The middle block shows the functions of the main processes performed by the different software and tools used in the pipeline. It starts from initial imaging (top) to final imaging (bottom). The left and right sides show input and output files, respectively, with the same coloured boxes representing the same files.

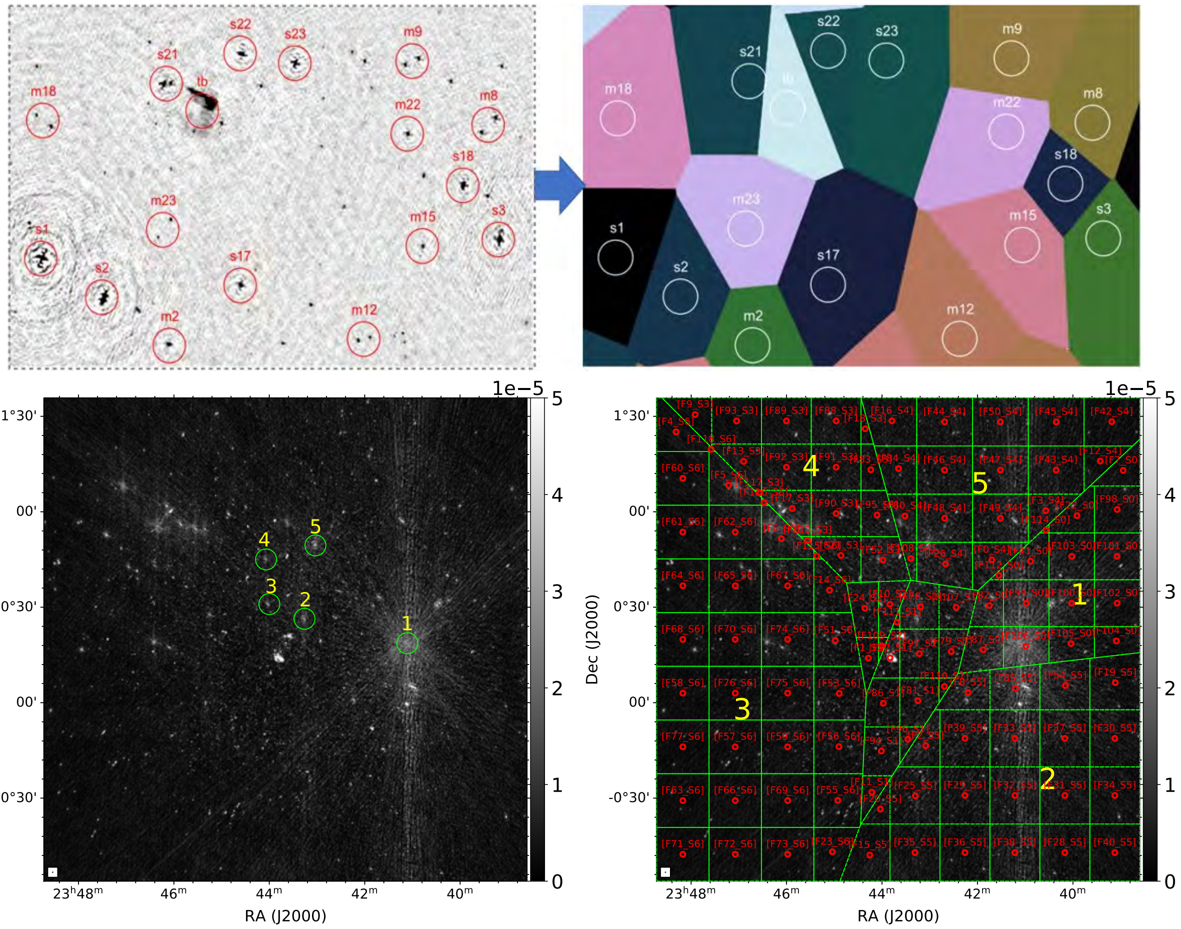

Figure 2.10: The `killMS` calibration framework. Calibration directions are defined by the tessellation of the image (right) from marked bright sources (left). *Top*: Example of calibration directions for the LOFAR image of a region around the Toothbrush cluster. `DS9` marked regions (left) define the tessellation of the image (right). The centre of each circle defines a direction to perform calibration (Van Weeren et al., 2016). *Bottom*: The same scenario as above for a wide FoV cluster field. The `DS9` marked regions are shown as green circles on the left and are labelled from 1 to 5. The right image shows the tessels (large green polygons) corresponding to the marked regions on the left with same labels. Brighter sources are associated with smaller tessels as they contain sufficient SNR (see source 1), while fainter sources are associated with larger tessels to capture sufficient SNR (see source 3). The smaller green squares are facets used by `DDFacet` for the imaging.

2.4.4 CubiCal: A peeling method

`CubiCal` is a software package written in Python that performs DD self-calibration using a simultaneous form of peeling approach called differential gains (Kenyon et al., 2018). The differential gains method is a generalisation of the first peeling procedure introduced by Noordam (2004) and is an extension to the framework presented in Smirnov & Tasse (2015) to solve for multiple gain terms. The solvers of `CubiCal` (phase-only, full 2×2 complex, amplitude and phase solvers), like with the ones from `killMS`, exploit complex optimisation. The RIME formalism introduces the notion of a Jones chain; a chain of gain terms, each of which may be defined over different time and frequency solution intervals (see Equation 2.4 of §2.2). This Jones chain constitutes a combination of DI and DD terms, expressing the entire calibration procedure as a single term. These multiple gain terms are solved sequentially without applying the inverse gains to the observed visibilities. `CubiCal` utilises the same structures found in `killMS` such as multi-processing and shared memory in combination with Cython* to allow maximisation of performance. We can use an arbitrary RIME for interferometers pq to explain the details of the differential gains approach of `CubiCal` (Smirnov, 2011):

$$\mathsf{V}_{pq} = \boldsymbol{G}_p \left(\sum_{pq} \sum_{s} \boldsymbol{E}_p \mathsf{X}_{spq} \boldsymbol{E}_q^H \right) \boldsymbol{G}_q^H \ . \tag{2.21}$$

Where V is the observed visibilities and X is the source coherency. In this equation, it represents the intrinsic DD skymodels for the individual sources s being peeled. $\boldsymbol{G}$ are DI errors affecting the entire FoV and are constrained to phase-only solutions. $\boldsymbol{E}$ are DD errors which are notably present around bright sources far away from the phase centre. These errors can be full complex 2×2 Jones matrices or can be constrained to complex diagonal and phase-only diagonal matrices. `CubiCal` solves for the $\boldsymbol{G}$ terms on small time/frequency scales for a few bright sources while simultaneously solving for $\boldsymbol{E}$ terms on larger time/frequency scales for a subset of fainter sources. The bright sources are manually marked and stored using `DS9` in the same way as described for the `killMS` procedure. This `DS9` source region file contains information on the specific direction

---

*Cython allows for the inclusion of C- like compiled code in Python.

in which to perform peeling. `CubiCal`, like `DDFacet`, can be run on the command line or through a parset file. A comprehensive list of all parameters can be found by invoking `gocubical -h` in the command line. We have shown in Appendix §G an example `CubiCal` parset file including some of its options.

The DI model used for the peeling is the `DDFacet` generated skymodel, the .DicoModel file. The source-specific DD model is generated from this skymodel, in conjunction with the `DS9` region file through the command `-model-list`. Simultaneous $\boldsymbol{G}$ and $\boldsymbol{dE}$ solving (where $\boldsymbol{G}$ and $\boldsymbol{dE}$ are specified through the option `-sol-jones`) can be performed on this model through enabling the option `-model-ddes`. Appropriate solution intervals must be chosen to obtain the best SNR ratio during calibration (Armel Mbou Sob et al., 2021). Time and frequency solution intervals are specified through `-g-time-int` and `-g-freq-int` , respectively. `-g-type` specifies the type of Jones matrix to solve for (full complex, diagonal or phase-only). After peeling, the final corrected visibilities are formed, which can be deconvolved and imaged by `WSClean` or `DDFacet`, forming the final calibrated image.

2.5 Data-reduction pipelines

The processing or reduction of data coming from modern telescopes is a daunting process due to the many factors that need to be taken into account simultaneously. There are usually only few a large effects and many small effects. The large effects are generally easy to identify and fix and have a significant effect on image quality as compared to the smaller ones. The smaller effects are more difficult to identify and filter out from the data and minutely affect the image quality. However, when the numerous small effects are combined they can be significant in deterring the image quality.

The high data rates and the requirement for real-time processing of future radio interferometers (including MeerKAT, uGMRT, VLA, LOFAR and SKA) have made it impractical to manually correct for these many small effects. Essentially, traditional manual data-reduction methods are no longer viable, necessitating the development of more sophisticated and easier methods, built upon a large element of automation. Automating several very time-consuming data-reduction steps, some of which albeit trivial (corresponding large and noticeable effects), involves performing a large number of iterations of calibration, imaging and flagging, with minimal user interaction. After each iteration, the quality of both the visibility data and the reconstructed skymodel is refined. At the end of this automation, most effects should be eliminated and the output data, almost science ready.

This automation of data-reduction applied to radio data is implemented in a framework called a pipeline. Pipelines simplify the cumbersome process of data-reduction, since all data-reduction tasks are systematically structured in a single framework allowing for efficient and reproducible data-reduction. We show in Figure 2.11 the general workflow used in reducing radio interferometic data. This type of workflow is implimented in data-reduction pipelines such as **C**ontainersed **A**utomated **R**adio **A**stronomy **Cal**ibration (`CARACal`) and **S**ource **P**eeling and **A**tmospheric **M**odelling (`SPAM`), which are discussed next.

2.5.1 The CARACal pipeline

The `CaraCal`* pipeline (Józsa et al., 2020) (formerly known as MeerKATHI) is a platform independent, flexible automated pipeline consisting of a collection of Python modules in the form of Stimela scripts that are used to execute all steps of data-reduction. Stimela (Makhathini, 2018) is a platform-independent (through the usage of containerisation technologies such as Docker, Singularity, Podman) framework for running diverse software in a pipeline. It allows combined usage of several open-source radio interferometry software packages (Common Astronomy Software (`CASA`), `Ragavi`, `CubiCal`, `AOFlagger`, `WSClean` and so forth) in the same script. `CARACal` can reduce radio interferometry continuum and spectral line data in full polarisation. It makes use of `CASA` for basic 1GC calibration and has the option of using two flagging packages, `AOFlagger` and `TriColour`. It uses `CubiCal` for 2GC calibration and `WSClean` for the imaging. Stimela incorporates all these software in a unified scheme, following a sequential order known as a workflow based on the user input, allowing the user to perform the corresponding data-reduction tasks in one flexible data-reduction script. This script takes the form of a master configuration file that

---

*`https://CARACal.readthedocs.io/en/latest/`

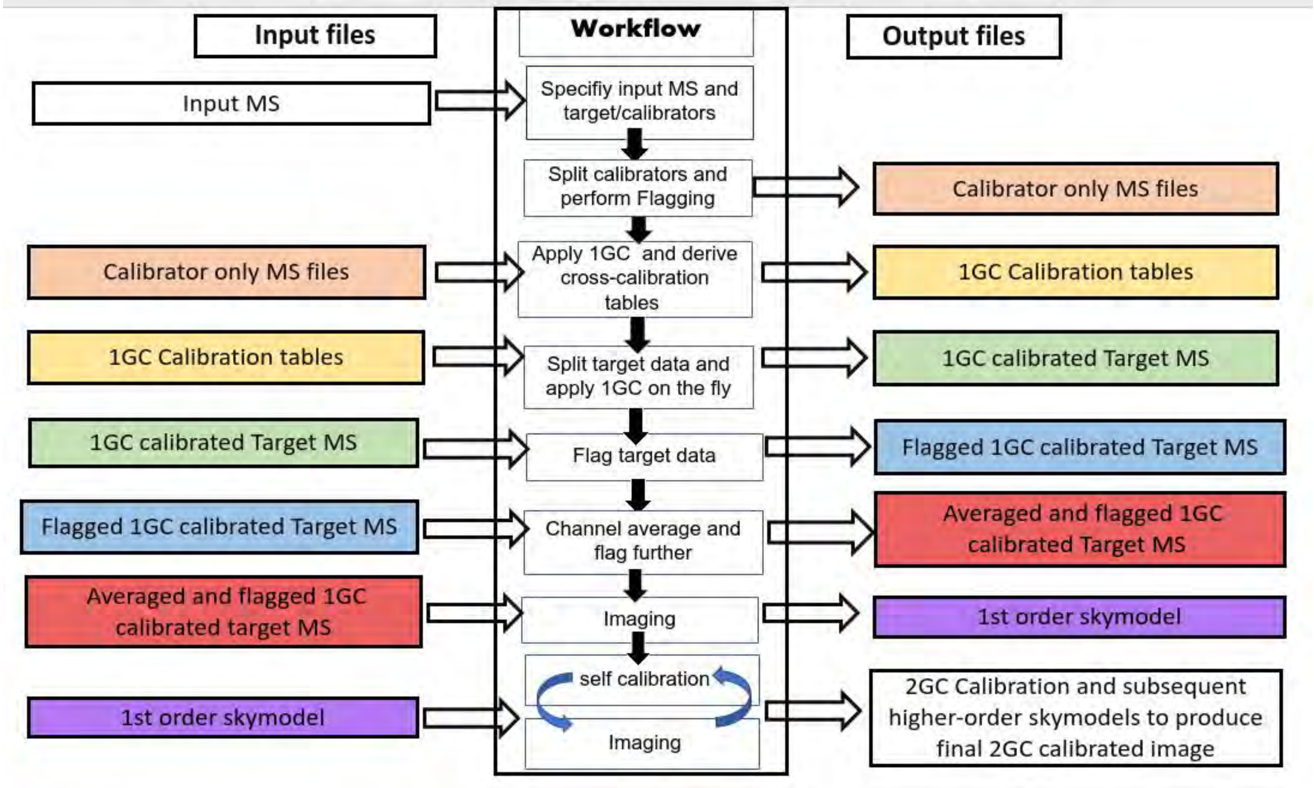

Figure 2.11: A schematic diagram showing the general radio interferometric data-reduction process. The central block depicts the general workflow and the input and output files are shown on the left and right, respectively. The same input/output files are shaded with the same colour.

utilises YAML (Yet Another Markup Language). YAML is a human-readable data-serialisation language designed to work well with modern programming languages for common everyday tasks (Ben-Kiki et al., 2009). It is commonly used for configuration files and in applications where data is being stored or transmitted. This makes it highly suitable for `CARACal`, as it can efficiently specify a series of modules (named workers) along with their various parameters (using a key-value pairs data scheme) needed for the data-reduction process. The relationship between `CARACal` workers, tasks and parameters is schematically shown in Figure 2.12. We have shown in Appendix F an example `CARACal` .yml file with workers, tasks and their parameters.

`CARACal` was initially developed for MeerKAT and has been used in a variety of MeerKAT projects. For example, it was used in the reduction of MeerKAT data of a bright radio galaxy

(ESO 137-006) situated in the Norma galaxy cluster (Ramatsoku et al., 2020). The output products revealed a complex collimated synchrotron thread network linking the lobes of the radio galaxy. This type of structure has never been observed in a radio galaxy before. HI observations of the galaxy group Fornax A were also reduced with `CARACal` (Kleiner et al., 2021). The detailed images show a host of pre-processing activity such as massive amounts of HI in the Inter Galactic Medium (IGM) and unusual galaxy morphologies. Active ongoing development by collaboration primarily between the South Africa Radio Astronomy Observatory, INAF-Osservatorio Astronomico di Cagliari and Rhodes University has already extended its data application to other telescope arrays similar to MeerKAT, such as VLA and uGMRT.

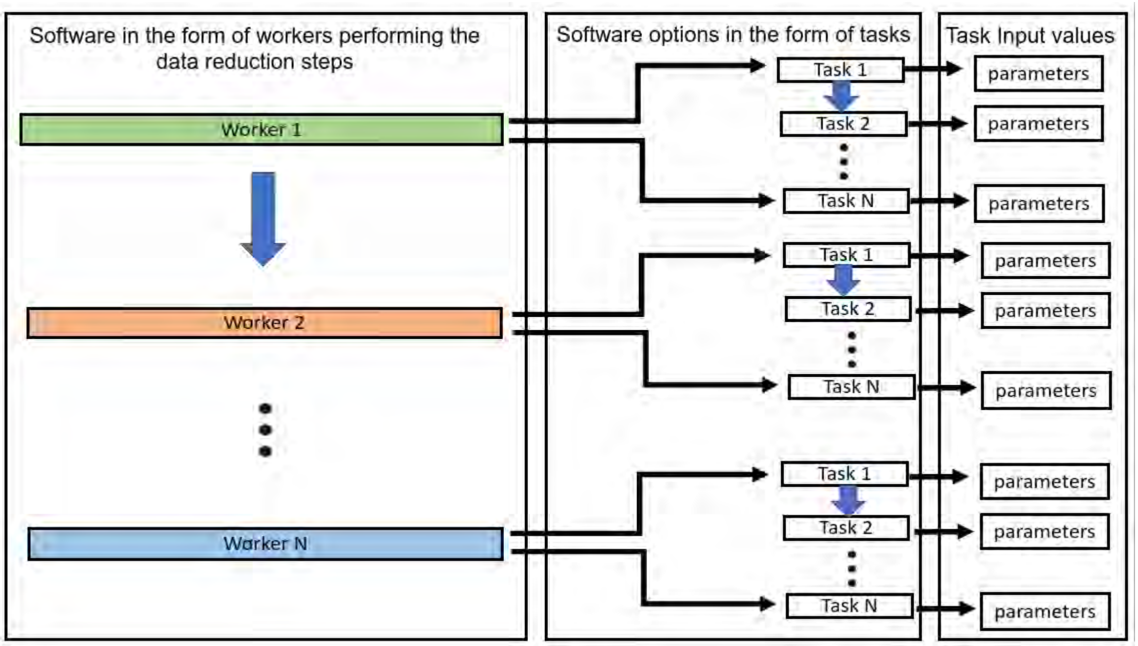

Figure 2.12: A schematic representation of the `CARACal` workflow showing the relationship between workers, tasks and parameters.

2.5.2 The SPAM pipeline

The `SPAM` pipeline* is a Python-based extension to the Astronomical Image Processing System (`AIPS`) pipeline (Greisen, 2003) designed to deliver science-ready data products in an efficient,

---

*`http://www.intema.nl/doku.php?id=huibintemaspam`

systematic and reproducible way with minimal user interaction (Intema et al., 2009; Intema, 2014). Its development was driven towards the reduction of complicated low-frequency GMRT data of galaxy clusters. `SPAM` is essentially a set of `AIPS`-based data-reduction scripts in Python that includes DD ionospheric calibration, modelling and imaging of radio interferometric data. The `AIPS` based functionality is delivered through a Python interface with the use of `Parsel Tongue` (Kettenis et al., 2006). `Parsel Tongue` makes the trusted `AIPS` algorithms and data structures available through Python. Data-reduction is performed through the collection of Python scripts that execute `AIPS` directly for the initial data-reduction steps. One of the special features of `SPAM` is that the pipeline is almost fully automated (with only few manual operations for initial input of data) for GMRT observations at 150, 235, 325, 610 MHz and has given good results for uGMRT band 3 (250-500 MHz) and band 4 (550-850 MHz) data.

Since its release in 2008, `SPAM` has been successfully applied to many GMRT data sets of various frequencies and has yielded good quality continuum images comparable with, or even better than manual `CASA` data-reduction. It was extensively used in the first data release of the 150 MHz continuum TIFR GMRT Sky Survey (TGSS) (Intema et al., 2017; Bhukta et al., 2022), highlighting its capability in providing highly efficient and reproducible data-reduction of data from high-resolution and low-frequency continuum observations. The details for running the `SPAM` pipeline on GMRT and uGMRT data sets are described here [*]. For wide-band uGMRT data, `SPAM` has difficulties processing large fractional bandwidths and therefore splits the bandwidth into smaller chunks (subbands) that are processed independently. The final step of `SPAM` data-reduction is to then use `WSClean` to jointly image the calibrated output visibilities of each subband.

2.6 Post data reduction: Image analysis techniques

Data from pipelines are not always science ready and might require further processing through application of advanced imaging and calibration software as discussed in §2.4. In addition, subtracting of discrete and unresolved point sources is a common practice in radio astronomy that

---

[*] `http://www.intema.nl/doku.php?id=huibintemaspampipeline`

helps to better image the target of interest.

Studying the final image quality after application of pipelines and calibration software, through the use of various statistical parameters is also a good practice to quantitatively check the image quality. These two techniques are the topics of discussion in this section.

2.6.1 Point source subtraction

With the increasing sensitivity of telescopes such as MeerKAT, we can detect more fainter populations of discrete point sources which were not possible to detect with previous telescopes. These point sources are often blended in with extended diffuse emission and add bias in estimating the physical properties of the extended target source. Hence it is important to pay attention to filter out and subtract these discrete point sources. Removing point sources is also an important task for generating an unambiguous spectral index map of the extended emission. There are various techniques available for excising point sources. One of the most standard and intuitive methods is that of subtraction of a high-resolution model from the visibility data. This high-resolution model is generated by imaging with uniform weighting and a applying a uv cut for exclusion of the inner baselines, putting more weight on the longer baselines that correspond to the angular size of small-scale structures. The high-resolution model will mostly contain point sources and will have filtered out any extended emission. This high-resolution model is then subtracted from the calibrated visibility data and the resultant residual data after subtraction is re-imaged using a natural weighting and with no uv cut. If the goal was to recover more flux from diffuse emission, a tapering of a larger beam size can additionally be applied to the final imaging step, which will lower the resolution. The resulting low resolution image will have the potential to pick up and emphasise any diffuse structure that was obscured by complexity and errors.

Due to the overall dependence this method has on the different angular scales of the underlying radio sources, the user can sometimes easily over-subtract and potentially suppress any faint and diffuse emission. The iterative nature of the procedure is also often time-consuming. As a result, it is necessary to develop a standard and efficient point source subtraction method that gives the user maximum control over the point sources in which they want to subtract using a minimum number of iterations. For this, we use the `Crystalball` software[*] which can be used within a Stimela script or in a pipeline to perform the subtraction. The method is illustrated in Figure 2.13. This method gives the user full control over the specific point sources they wish to subtract by allowing the user to manually select the point sources in which they want to subtract. These sources are saved in a point-source specific column in the MS (instead of a high-resolution model as with previous method) making the point source removal procedure a simple subtraction of columns. This procedure requires the (source-specific) region file generated from the SAOImage `DS9` viewer, in combination with a clean components source list file[†] generated from `WSClean`. The procedure is as follows:

1. The user creates the `DS9` region file by manually marking the point sources in the image which they want to remove using circular regions.

2. The clean components source list file is generated from `WSClean` with the `-save-source-list` option. This option can be specified during the final self-calibration imaging step of the pipeline (`SPAM` or `CARACal`).

3. `Crystalball` is then used to take these two files, point source regions and clean component list, to generate another column in the given MS, containing the predicted visibilities for the clean components within the specified `DS9` regions. This column contains the point sources we wish to subtract.

4. This column can then be subtracted from the visibilities using MSUtils[‡] and the residuals are then re-imaged with `WSClean`, `DDFacet` or any other imaging software to create the source-subtracted image.

The `Crystalball` method is easily transferable from one data set to another as the user is not required to modify several imaging parameters to produce a high-resolution model as would be required in the previously mentioned general method, since all steps in List 2.6.1, are independent of the image properties.

---

[*] https://github.com/paoloserra/crystalball

[†] https://sourceforge.net/p/wsclean/wiki/ComponentList/

[‡] https://github.com/SpheMakh/msutils

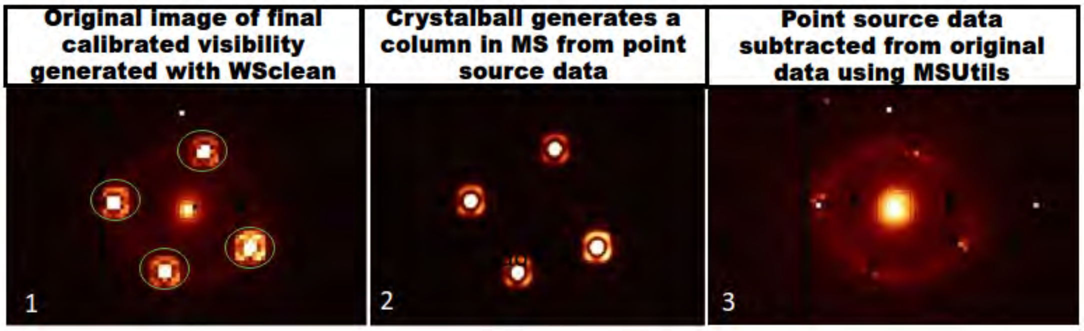

Figure 2.13: The general procedure of point source subtraction using the `Crystalball` method demonstrated on stimulated data of a galaxy with diffuse emission surrounded by four point sources. The first diagram has marked the location of these point sources with green circles using the `DS9` software (Step 1 in List 2.6.1). The 2nd diagram shows what would result if we imaged the column created from the `DS9` region file of left image with clean components file generated from `WSClean` (Step 3 in List 2.6.1). The final image shows after subtraction, we can visually see that more flux has been recovered from the diffuse emission (Step 4 in List 2.6.1) (Biernaux et al., 2016).

2.6.2 Image fidelity and dynamic range

Radio interferometric data are invariably corrupted by a host of errors due to atmospheric and instrumental effects. The calibration techniques and various imaging algorithms can eliminate only a limited amount of errors, and as a result, the final image will always deviate from the true image. Image fidelity and dynamic range (DR) are terms that are used to quantitatively estimate the errors of this final image (Taylor et al., 1999). Image fidelity is a general term used to quantify how well the original source brightness has been re-constructed in the image. It attempts to measure the difference between the produced image and that of the ideal image. Due to lack of prior knowledge of the ideal image, combined with the impracticality of determining an error for every pixel in an output image, image fidelity cannot be directly measured. We can, however, use a parameter called the DR as a means to qualitatively judge the image fidelity. The DR is generally measured by the ratio of peak brightness/maximum intensity to image root mean square (RMS). According to the literature (Braun, 2013), there are three accepted ways to calculate this quantity from radio astronomical images:

$$DR1 = \frac{flux_{\text{peak}}}{RMS_{\text{local}}}, \quad DR2 = \frac{flux_{\text{peak}}}{min_{\text{local}}}, \quad DR3 = \frac{flux_{\text{peak}}}{RMS_{\text{global}}} . \tag{2.22}$$

Where $flux_{\text{peak}}$ is the peak brightness/maximum intensity. RMS_{local} and RMS_{global} is the RMS for a region of an image and full image, respectively. It will be shown in §4.1 that, as a result of these definitions, the DR is as a measure of the degree to which imaging artefacts or calibration errors around the strong source(s) are suppressed. Increased DR therefore represents, increased image fidelity and better on-source reconstruction. The DR depends on size, type and distribution of errors in the visibilities. Images produced after 1GC calibration will typically yield DR of $\sim 10^2 : 1$, 2GC calibrated images can reach DR's of $\sim 10^5 : 1$, while 3GC is has been able to reach DR's beyond that of $\sim 10^6 : 1$ (Smirnov, 2011; Braun, 2013).

2.6.3 Statistics in radio astronomy

The raw visibilities obtained after filtering through various electronics from the receiver are commonly converted into an MS format for use in data-reduction. The raw visibilities contain noise derived from many different sources that is Gaussian in the real and imaginary parts. From the vCZ theorem of Equation 2.1, it then follows that, in the ideal case, image pixel noise will also be Gaussian (albeit spatially correlated by the PSF). Calibration errors and/or imaging artefacts will then cause a deviation from Gaussianity. We can use several statistical measures to characterise this deviation. Table 2.2 shows a number of statistical parameters often used in radio astronomy and the statistical category in which they occupy. These categories are location measures, dispersion measures (or measures of scale) and moments. Location measures describe the central tendency of data, dispersion measures describe the spread and moments characterise the distribution. We describe the ones most relevant to radio astronomy.

In this work, we apply these statistical measures to our final restored images, where data resides in image space. MIN and MAX are the minimum and maximum pixel values, respectively, in an image. They will often capture outliers. The RMS is an important quantity in radio astronomy. It was used in the definition of DR in Equation 2.22 and is also used to quantify the sensitivity

Table 2.2: Statistical parameters and their definitions grouped into three categories.

Category	Statistical quantities	Precise definition
Location measures	Mean ($\hat{x}$)	$\frac{\sum_i^N x_i}{N}$
	Max (MAX)	$\max(x_i)$
	Min (MIN)	$\min(x_i)$
	Normal (NORM)	$\sqrt{\sum_i^N \lvert x_i \rvert^2}$
Dispersion measures	Standard deviation (s)	$\sqrt{\frac{\sum(x_i - \hat{x})^2}{N-1}}$
	Root Mean Square (RMS)	$\sqrt{\frac{\sum_i^N x_i^2}{N}}$
	Mean Absolute Deviation (MAD)	$\frac{1}{N}\sum_i^N \lvert x_i - \hat{x} \rvert$
	Dynamic range (DR)	$\frac{\max(X_i)}{RMS}$
Moments	Kurtosis (KURT)	$\frac{1}{N}\frac{\sum_i^N (x_i - \hat{x})^3}{s^3}$
	Skewness (SKEW)	$\frac{1}{N}\frac{\sum_i^N (x_i - \hat{x})^4}{s^4}$

of an observation. The RMS found in a residual image or in a region of a restored image void of emission is known as RMS sensitivity or thermal noise* and is commonly indicated by σ_{rms} or just σ. The σ_{rms} is an important quantity used to confirm the 'detection' of a signal of interest. The most common measure of detection of this signal is the $3\sigma_{\text{rms}}$ result. This is directly related to the normal distribution; detection at the $3\sigma_{\text{rms}}$ level means that there is a signal present at an amplitude of three times the standard deviation of the noise. MAD is a robust determination of the variability of data as it is not affected by outliers. It is biased in the presence of asymmetrical distributions and only relevant for statistical samples which are symmetrically distributed around their median. KURT characterises the distribution tails or indicates the degree of peakiness. A KURT = 3 is a normal distribution. SKEW indicates deviation from symmetry about a mean. SKEW = 0 is a normal distribution indicating complete symmetry about the mean. We have shown their interpretation in Figure 2.14.

To calculate these various statistical values we made use of the in-house Astronomical Image

---

*The thermal noise also be directly calculated from: $\sigma_{\text{rms}} \sim \frac{T_{sys}}{\Delta\nu\tau}$, where T_{sys} includes all noise contributions from source, atmosphere, ground, telescope and receiver, to name a few. $\Delta\nu$ and τ are the bandwidth and integration time of the observation, respectively.

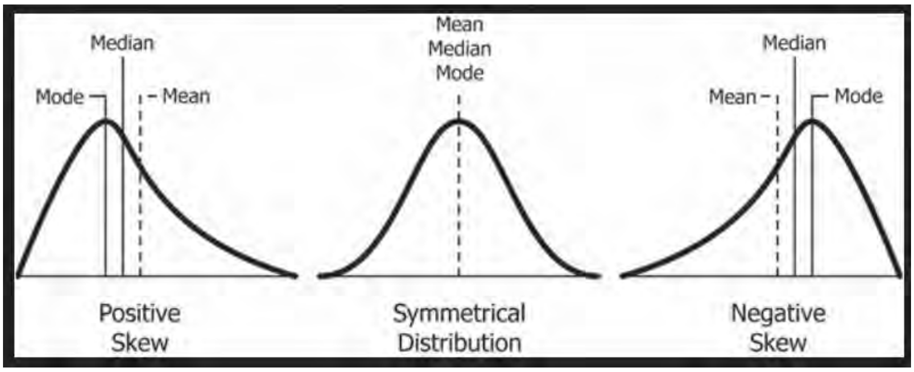

Figure 2.14: Simple illustrations showing the moments, KURT and SKEW, and how they quantify variation from a normal distribution.

Fidelity Assessment Tool (`aimfast`) Software*. This easy to use software is run from the command line and can calculate various statistical properties for the full image or specified cut-out regions.

---

*https://github.com/Athanaseus/aimfast

Chapter 3

Saraswati supercluster and MeerKAT observations

3.1 Introduction to the Saraswati Supercluster

The *Saraswati* supercluster is one of the largest structures in the observable universe (Bagchi et al., 2017, hereafter B17). The size and mass of the *Saraswati* supercluster is ~ 200 Mpc and $\sim 2 \times 10^{16}$ $\mathrm{M}_{\odot}$, respectively. It is located at a redshift of $z \sim 0.28$ and was originally found in the Stripe 82 region in the 3rd generation phase of the Sloan Digital Sky Survey (SDSS-II) (Abazajian et al., 2009). The main body of this wall-like supercluster comprises of at least 43 massive galaxy clusters and 3016 galaxies. There are five high-mass galaxy clusters concentrated in its dense (gravitationally bound) core region, which extends to a radius of 20 Mpc and encompasses a mass of at least 4×10^{15} $\mathrm{M}_{\odot}$ (20% of total supercluster mass). This core region, therefore, makes up the majority of its total mass component. Its unique features not only include its mass and size but also its highly unusual morphology and richness. These properties reveal that it was formed by some extreme, large-scale, matter density enhancements in the early universe around ~ 4 Gyr. *Saraswati*'s most significant feature is, however, the presence of localised non-thermal diffuse emission spanning the optical filament of galaxies on beyond Mpc scales. These filaments, located near the core of the supercluster are suspected to be related to the complex dynamic state of the cluster. *Saraswati* stands out in the sky as an especially rare and possibly one of the largest significant density enhancements found at medium-high redshift epochs. Only a few superclusters of this size and mass magnitude are currently known in the early universe, namely the Shapley Supercluster ($z = 0.046$) (Shapley & Ames, 1930; Venturi et al., 2017, 2022) and the BOSS great wall ($z = 0.47$) (Liivamägi et al., 2012; Lietzen et al., 2016). In the left of Figure 3.1 we show a redshift cone plot from $z = 0$ to $z = 0.4$ indicating the region making up *Saraswati* shown by a curved red rectangle centred on its position. The two plots on the right side of this figure show this same region successively magnified.

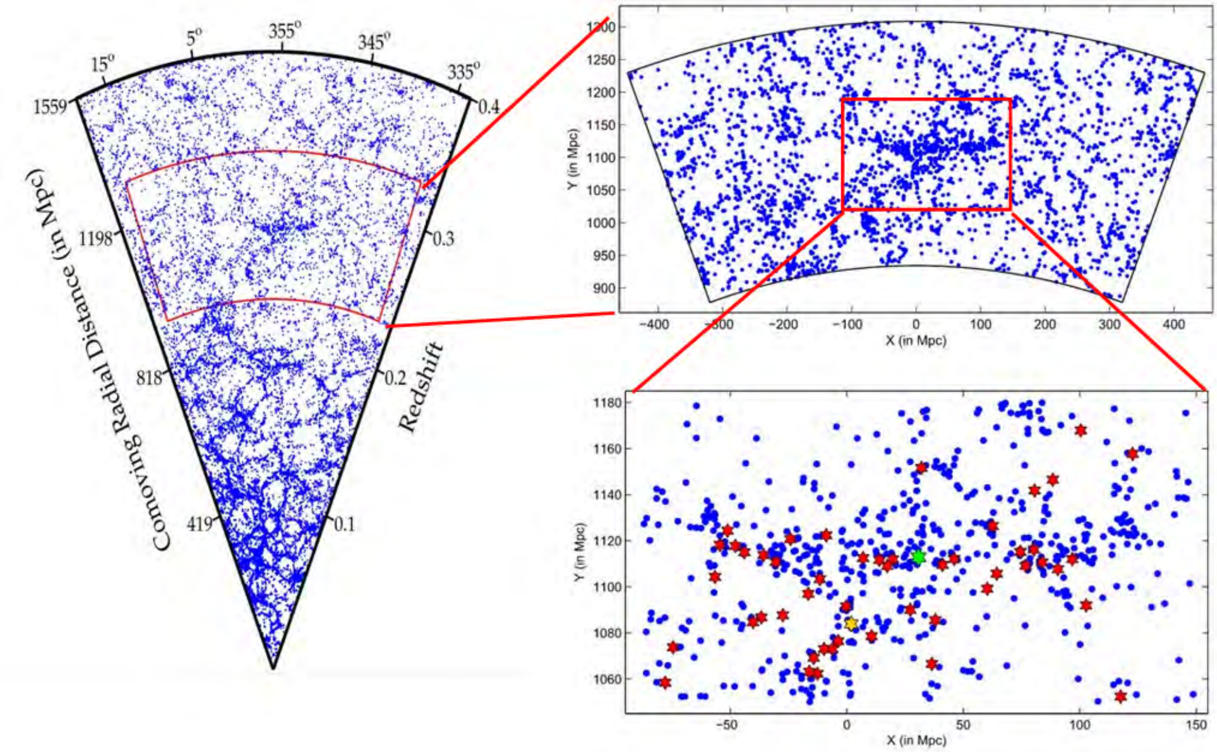

Figure 3.1: The location of the *Saraswati* supercluster in the nearby universe and its galactic distribution. *Left*: Redshift cone plot of SDSS galaxies (shown as blue dots) extending from $z = 0$ to $z = 0.4$. The red curved box of width RA 45°, and height DEC 2.5°, shows the concentration of galaxies making up the *Saraswati* supercluster. *Top right*: A close-up view of the red box region from the cone plot (left) showing a more detailed view of the galaxy distribution. The width and height of the box are around 800×300 Mpc^2. *Bottom right*: A close-up view of the red box region from the previous image (top right) showing the distribution of galaxy clusters in *Saraswati* marked by the red stars ★. ZwCl 2341.1+0000 (ZwCl 2341 hereafter) is marked by a orange star ★ and Abell 2631 (A2631 hereafter) by a green star ★ (Bagchi et al., 2017).

3.1.1 The complex galaxy clusters ZwCl 2341 and A2631

The most massive and second largest galaxy clusters residing in the dense core of the *Saraswati* supercluster is A2631 and ZwCl 2341, respectively. These clusters are shown in the zoomed-in cone plot region at the bottom right of Figure 3.1. The position of ZwCl 2341 and A2631 is indicated by an orange star ★ and green ★ star, respectively.

3.1.1.1 ZwCl 2341

ZwCl 2341 is a multi-filamentary Mpc scale galaxy structure (at $z = 0.269$) associated with complex diffuse radio emission. It is located ~ 45 Mpc from the core of the *Saraswati* supercluster and resides on a trail of galaxies that make up the southern filamentary network connected to the main central region. Optical analysis and dynamical mass estimates of Boschin et al. (2013) concluded that the system is likely comprised of three to six subclusters with a total dynamical mass estimate in the range $10^{14} - 10^{15} h_{70}^{-1}$ $M_{\odot}$. Weak gravitational lensing mass estimates by Benson et al. (2017) reported a mass of $(5.57 \pm 2.47) \times (10^{14}$ $M_{\odot})$, which is consistent with the estimate made by the Planck Collaboration (Ade et al., 2016) of $(5.2 \pm 0.4) \times 10^{14}$ $M_{\odot}$. Weak gravitational lensing mass estimates are the most robust estimators of cluster mass for merging clusters since they are independent of the cluster state. Dynamical mass estimates are biased to merging galaxy clusters due to the disturbed nature of the galaxy velocities of these systems, which is used to calculate the dynamical mass.

The large mass and complex nature of ZwCl 2341 is either a result of multiple merger events between several galaxy groups/clusters or from the infall of multiple filaments at the node of the cosmic web that took place during the initial phase of the cluster formation process. ZwCl 2341 hosts a giant pair of widely separated (~ 2 Mpc) symmetric radio relics situated perpendicular to the merger axis at the periphery (Van Weeren et al., 2009b, hereafter V09). The relics are assumed to be caused by accelerated particles and amplification of magnetic fields as a result of outward travelling shocks originating in the cluster centre created from the cluster formation processes as mentioned above. We show multi-frequency MeerKAT radio, Chandra X-ray and Data release 9 (DR9) of DeCAM legacy survey (DECaLS) optical images in the top image of Figure 3.2; clearly showing the disturbed X-ray emitting ICM gas bracketed by the peripheral radio relics. We also show in Figure 3.3 optical data from DECaLS DR7 (Dey et al., 2019) centred on the same coordinates as Figure 3.2 and with a similar scale. The top image of ZwCl 2341 in Figure 3.3 clearly shows a trail of galaxies concentrated at the centre spanning this central region from the NW to SE direction. In Figure 3.2, we see that this region is bounded by the peripheral relics. Double radio relics are an important subclass of extended radio sources as they allows us to put additional constraints on the cluster merger scenario (Bonafede et al., 2017).

3.1.1.2 A2631

A2631 is the most massive galaxy cluster (at $z = 0.277$) located at the centre of the bound core of the *Saraswati* supercluster. It is a rich (Abell richness class $\mathcal{R} = 3$), massive $M_{500} \sim 10^{15}\ \mathrm{M}_{\odot}$ and hot ($T_X \sim 8$ keV) galaxy cluster (Monteiro-Oliveira et al., 2021). Chandra and XMM-Newton X-ray data of A2631 (Finoguenov et al., 2005) show an elongated ICM structure with relatively high central entropy suggesting that A2631 is in a late stage of a massive merging event. These X-ray observations also suggest the absence of a cool-core. Radio observations (Knowles et al., 2019) have not shown any sign of the presence of extended radio sources residing in A2631, which is puzzling considering halos and relics should be prominent signatures in massive merging clusters. The dynamical state of A2631 is therefore still unclear. Optical data from DECaLS shown at the bottom of Figure 3.3 show a dense concentration of optical galaxies at the core.

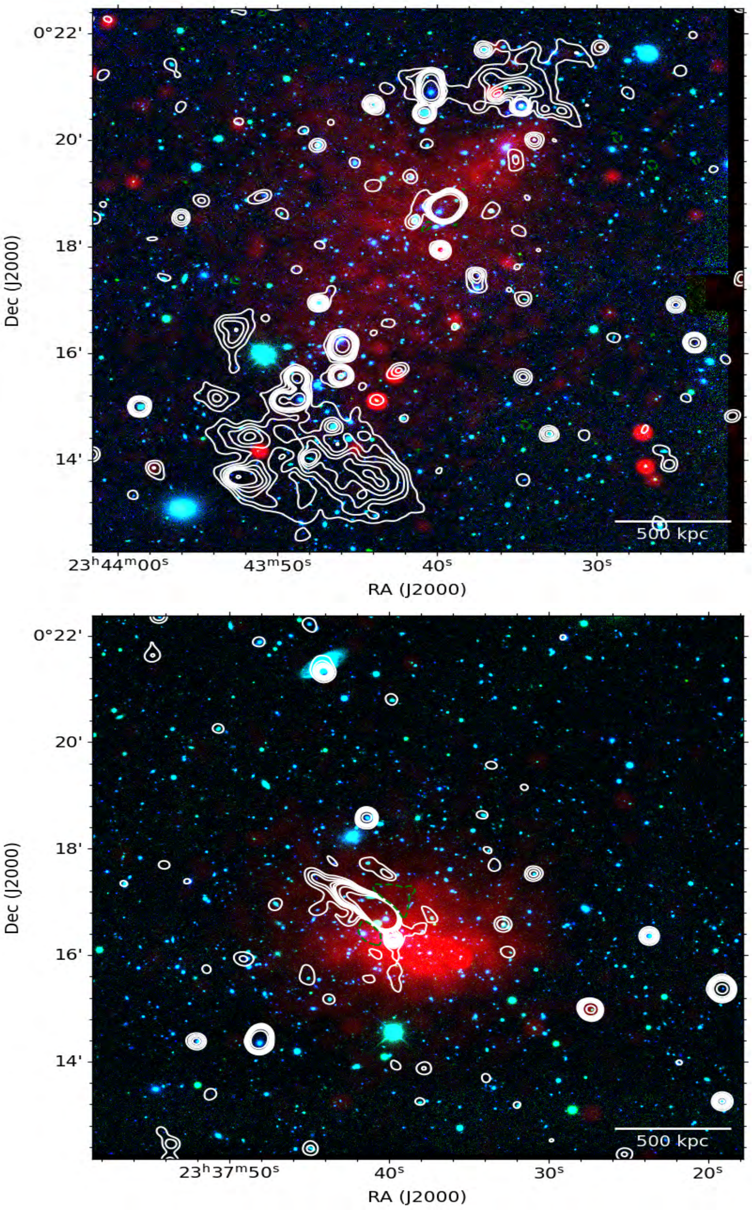

Figure 3.2: MeerKAT DI calibrated radio image overlayed on multi-colour red, green, blue (RGB) images of the two galaxy clusters, ZwCl 2341 and A2631, residing in the core of the *Saraswati* supercluster. Radio emission is shown by the white contours. The spatial scale is shown by the horizontal white line at the bottom right of each image. The Chandra X-ray emission is shown by red and DECaLS DR9 optical data as combinations of blue and green. The negative radio contours are shown by dashed green lines. *Top*: The second most massive galaxy cluster in *Saraswati*, ZwCl 2341, with radio contour levels spaced as: $[-1, 1, 3, 5, 9, 15, 20] \times 4\sigma_{\rm rms}$, where $\sigma_{\rm rms} \sim 11$ μJy beam^{-1}. This cluster hosts a pair of diffuse relics cluster at the periphery. *Bottom*: The most massive galaxy cluster in *Saraswati*, A2631, with radio contour levels spaced as: $[-1, 1, 3, 5, 9, 15, 20] \times 5\sigma_{\rm rms}$, where $\sigma_{\rm rms} \sim 9$ μJy beam^{-1}. This cluster hosts no large scale diffuse radio emission.

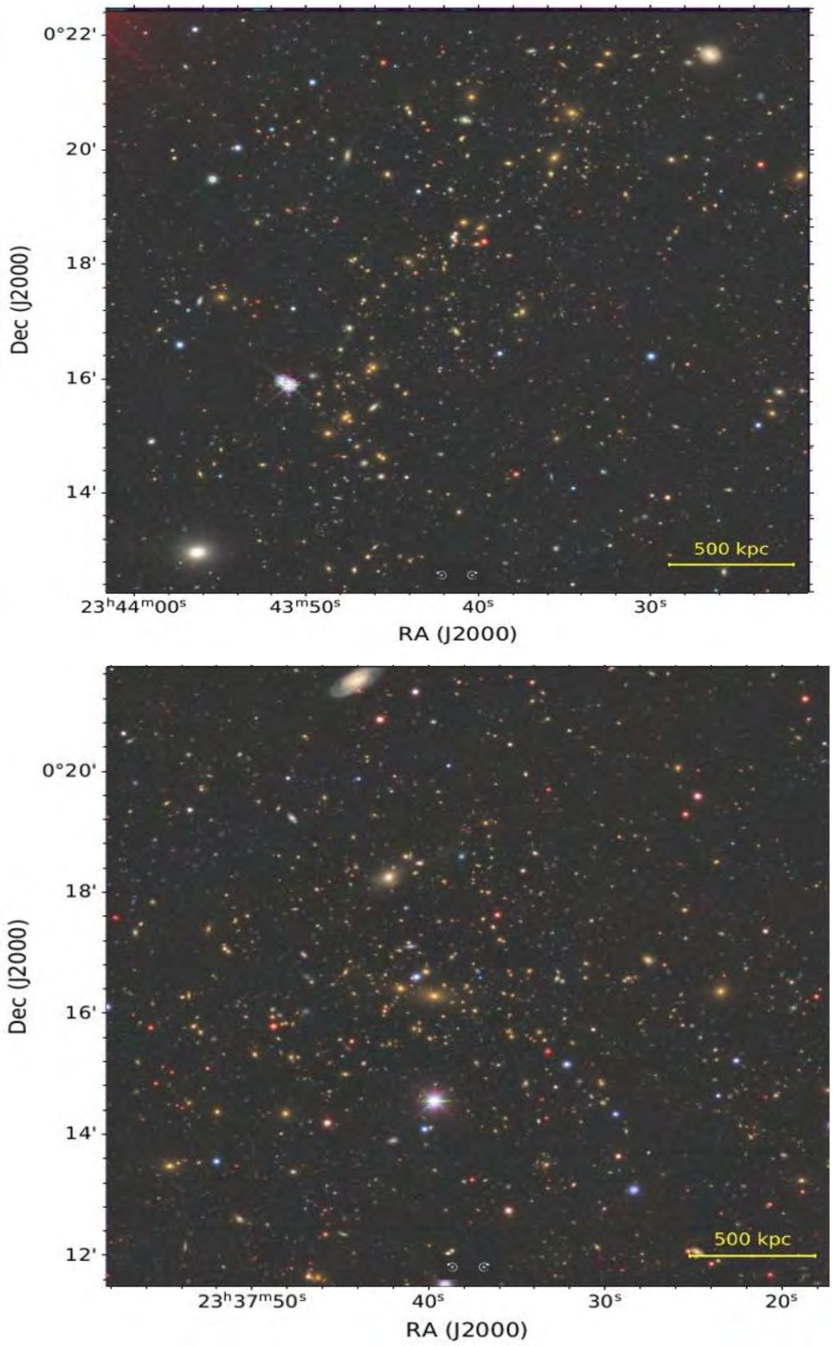

Figure 3.3: Optical images from DECaLS DR7 of the two most massive galaxy clusters in the *Saraswati* supercluster. *Top*: ZwCl 2341 optical image showing an optical filament of galaxies spanning the central region. *Bottom*: A2631 optical image showing a dense concentration of galaxies in the core region.

3.2 Previous observations of ZwCl 2341

The multi-Mpc scale filamentary network of galaxies in ZwCl 2341 was initially discovered in an ongoing program to search for large-scale diffuse radio emission originating in distant clusters of galaxies (Bagchi et al., 2002, hereafter B02). The primary aim of the program was to investigate the origin and evolution of high energy relativistic particles and magnetic fields in the IGM of large cosmic structures. To achieve this project aim, B02 searched for the presence of diffuse radio emission in the fields of several Abell (Abell, 1958) and Zwicky (Zwicky, 1937) clusters from archival data from the NRAO VLA sky survey (NVSS) (Condon et al., 1998). From this data, B02 found large-scale diffuse radio emission spanning a filamentary network of faint galaxies at the position R.A. $23^{\mathrm{h}}43^{\mathrm{m}}39^{\mathrm{s}}.7$, Dec. $+00^\circ16'39''$ corresponding to ZwCl 2341. These initial findings led to the motivation for further detailed radio observations.

3.2.1 Radio observations of ZwCl 2341

Initial observations by B02 were the first to give evidence of cosmic-ray particle acceleration taking place in the filaments of ZwCl 2341 from cosmic shocks on beyond ∼ Mpc scales. Due to sensitivity constraints, the radio emission could not be classified. Follow-up higher sensitive GMRT observations (V09), VLA observations (Giovannini et al., 2010, hereafter G10) and then JVLA (Benson et al., 2017, hereafter B17) were then able to classify the emission as a familiar class of a rare and extended source. We describe these previous observations in the subsections below, from oldest to most recent. Figure 3.4 shows the corresponding images involving these previous observations also from oldest (top left) to most recent (bottom right).

3.2.1.1 NVSS observation

Diffuse radio emission forming two radio components, a northern and southern component with a complex morphology, was initially discovered at 1.4 GHz from NVSS[†] archival data (B02). The NVSS survey uses the VLA's most compact D-array configuration. This initial data additionally

---

[†] `http://www.cv.nrao.edu/nvss/`

used archival X-ray ROSAT and optical SDSS survey data to further characterise the environment. The diffuse radio emission can be seen following the north-south galaxy distribution with a not so steep ($\alpha \sim -0.5$) spectral index. This analysis was the first evidence of particle acceleration taking place in the filaments of ZwCl 2341 from cosmic shocks in the IGM over a scale of ≥ 5 Mpc. However, due to poor sensitivity ($\sigma_{\rm rms} \sim 0.55$ mJy beam^{-1}) and angular resolution (beam size $\sim 108''$), the nature of the diffuse emission could not be classified. This low-resolution image is shown in the top left of Figure 3.4.

3.2.1.2 Low-frequency GMRT observation

After the initial NVSS VLA analysis of B02, high sensitive (narrow-band) radio observations were then carried out with GMRT at 610, 241 and 157 MHz (V09). This GMRT observation was the first to classify the diffuse sources as double radio relics. Their high-resolution 610 MHz image with a beam size of $6.9'' \times 4.3''$ gave the best result in terms of disentangling the northern and southern parts of the diffuse emission into two well-resolved regions located at the north-west (NW) and south-east (SE) region of the cluster centre. Both components are located at the periphery of the cluster with no direct connection to any of the radio galaxies (or compact point sources). V09 also combined Chandra and optical SDSS data with their radio observations. The radio emission is located outside the X-ray emission symmetrically on both sides, similar to other double relics such as A3376 (Chibueze et al., 2021), A2345 (Boschin et al., 2010) and A2140 (Bonafede et al., 2009a; Cho et al., 2022). An elongated structure of optical galaxies also follow the X-ray emission with orientation perpendicular to the symmetry axis of the double relics. V09 concluded that these properties all point towards the existence of double radio relics, a south relic (SR) and a north relic (NR). The relic structures differ from those of typical elongated relics. The SR consists of three different components labelled RS1, RS2 and RS3. The NR relic has a size of about $1.5' \times 1'$ (0.37×0.25 Mpc^2). The SR has a size of about $5' \times 2'$ (1.2×0.49 Mpc^2). The spectral index for the NR and SR is $\alpha_{NR} \sim -0.49$ and $\alpha_{SR} \sim -0.76$, respectively. The 610 MHz GMRT radio image of V09 with optical and X-ray data overlayed is shown at the top right of Figure 3.4.

3.2.1.3 VLA observation

After V09, the ZwCl 2341 region was then observed for 6 hours with the VLA at 1.4 GHz using the compact D configuration (G10). G10 produced both low-resolution (beam size $\sim 83'' \times 75''$) and higher-resolution images (beam size $\sim 50'' \times 43''$). For the low-resolution image, the radio morphology is similar to earlier observations of B02 in which large scale diffuse radio emission, forming a single component spanning the central region from north to south, was found along the whole optical filament. This emission also followed the distribution of optical galaxies and X-ray emission of V09. This diffuse emission was characterised as a low surface brightness source with surface brightness $\sim 7 \times 10^{-5}$ mJy arcsec^{-2} and total size of $\sim$ 2.2 Mpc. The radio emission is irregular and decreases from the two bright outer regions toward the cluster centre. From this low-resolution data, G10 produced polarisation angle and intensity maps and found a higher degree of polarisation in the southern region ($\sim$ 15%) as compared to the north ($\sim$ 8%). The central region had a polarisation of $\sim$ 11%. For the polarisation angle maps, the polarisation vectors exhibit a regular pattern orientated towards the NE-SW direction in going from the south to north region. The large-scale filamentary diffuse emission found in this low resolution observation spanning the cluster centre implies the presence of a potential radio halo or bridge source. This potential halo or bridge has been the main driver for further observations involving this system. This large-scale diffuse emission is shown in the top left of Figure 4.9 in §4.

For the higher resolution images, the extended diffuse emission at the centre was resolved out and the northern and southern components were separated into two well-defined elongated components, NW and SE that align with the NR and SR of V09. This data could not be used to estimate the spectral index values due to the different sensitives and *uv* coverage with V09. We show the higher-resolution image at the bottom left of Figure 3.4.

3.2.1.4 High-frequency JVLA observation

The most recent VLA analysis comes from (Benson et al., 2017, hereafter B17) who used high-frequency JVLA S-band (2-4 GHz) observations in C and D configuration. Their low-resolution images ($32'' \times 24''$) were able to separate out the relics to a NR and SR as with V09 and G10. The relics have a shape, size and morphology are also similar to previous observations of V09 and G10. They also derived polarisation maps as with G10 with similar polarisation vector orientations. They however, found polarisation intensity to be slightly lower as G10 for the northern ($\sim 5\%$) and southern (8%) regions, respectively. They computed spectral index values using the 610 MHz V09 measurements in combination with their own, and found index values of $\alpha_{NR} \sim -1.31$ and $\alpha_{SR} \sim -1.20$ for the NR and SR, respectively. We show the high-resolution image overlayed with low-resolution ($32'' \times 24''$) contours at the bottom right of Figure 3.4.

3.2.2 X-ray observations of ZwCl 2341

X-ray observations by Chandra and XMM-Newton satellites of ZwCl 2341 have been independently conducted (Böhringer et al., 2007; Raychaudhury et al., 2009) and authors such as V09 have combined this data with their radio analysis. These observations essentially showed X-ray emission spanning over ~ 3.3 Mpc in the north-south direction along the NE-SW merger axis, with a morphology indicative of a highly distorted ICM, a clear sign of a recent or ongoing merger (Van Weeren et al., 2010). Later observations by Chandra and XMM-Newton (Akamatsu & Kawahara, 2013; Ogrean et al., 2014) gave more details on this disturbed X-ray morphology showing the X-ray emission elongated along the NW-SE merger axis with structures including that of an out-bound bullet-like structure at the NW, a tail-like structure at the SE and excess emission perpendicular to the merger axis toward the E-NE direction (NE wing). These features are marked and shown on the left in Figure 3.5. They also reported a global temperatures and luminosities in the range of $kT_X \sim 4-5$ keV and $L_X \sim 0.3-0.8$ erg s^{-1}, respectively.

The most recent deep Chandra observations (Zhang et al., 2021) have conducted detailed X-ray analysis on the ZwCl 2341 system. They identified several new unique surface brightness features in the X-ray morphology. The NE bullet-like structure is actually a cone-shaped structure with linear surface brightness edges on both sides of the cone. This cone-shaped structure is subtended below by two wing structures stretching towards the NE and W directions. The tip of

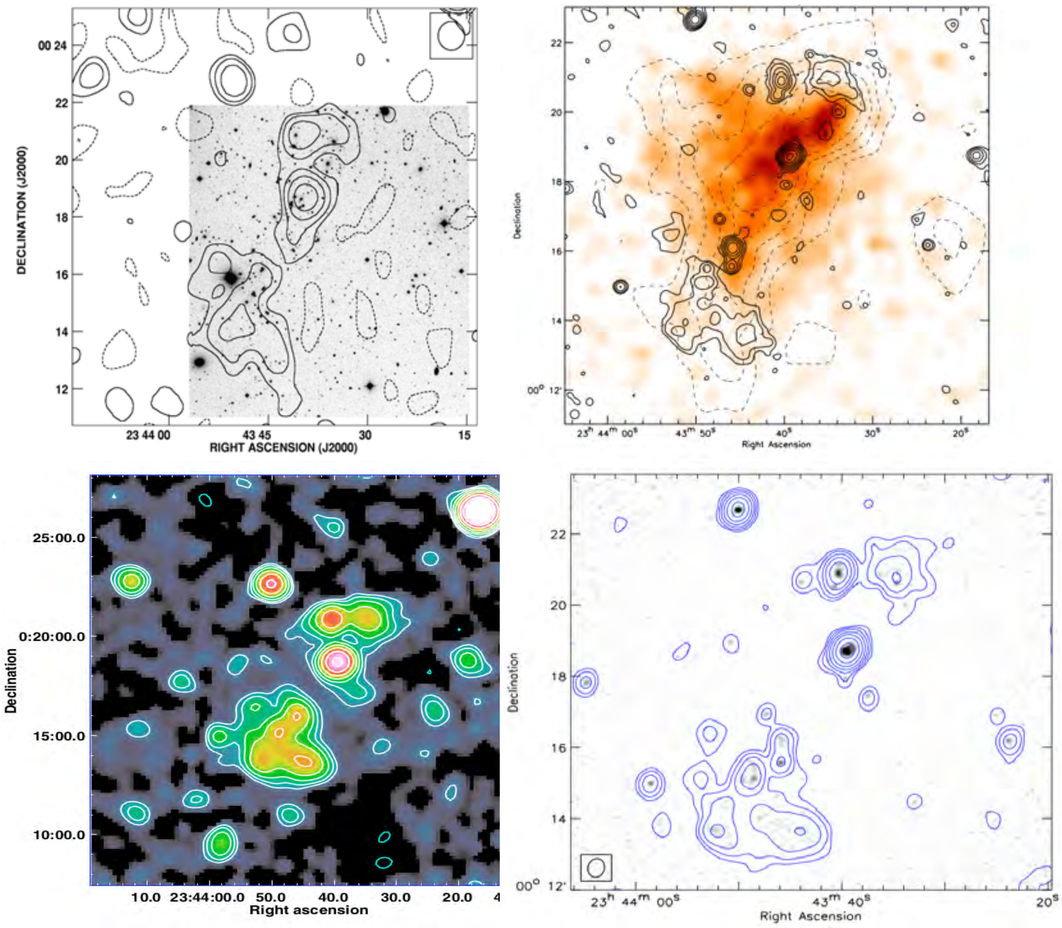

Figure 3.4: Radio observational history of ZwCl 2341. *Top left*: Initial NVSS 1.4 GHz observation that first reported the hint of diffuse radio emission in the ZwCl 2341 system. This image shows the VLA 1.4 GHz radio contours superposed on the optical R-band CCD image. The contour levels are $[-4, -2, -1, 1, 2, 4, 8, 16] \times 1.6\sigma_{\rm rms}$, where $1\sigma_{\rm rms} = 0.55$ mJy beam^{-1} and beam size $1'$ (shown at top right) (B02). *Top right*: Low-frequency GMRT point source subtracted radio emission (contours) at 610 MHz overlayed with Chandra X-ray emission (orange colour) in the 0.5-3.0 keV energy band and spectroscopic data (dashed contours) from SDSS. Radio contours are spaced as: $[1, 2, 4, 8, 16, 32] \times 3\sigma_{\rm rms}$, where $1\sigma_{\rm rms} = 0.22$ mJy beam^{-1}. The beam size is $6.9 \times 4.3'$ (shown at bottom left) (V09). *Bottom left*: Subsequent VLA observation. Colour and radio contours show the VLA-D configuration at 1.4 GHz. The contour levels are spaced as: $[1, 2, 4, 8, 16] \times 3\sigma_{\rm rms}$, where $1\sigma_{\rm rms} = 0.15$ mJy beam $^{-1}$. The beam size is $83'' \times 75''$ (not shown) (G10). *Bottom right*: High-frequency JVLA 2-4 GHz low-resolution radio emission shown as blue contours. The contour levels are spaced as: $[1, 2, 4, 8, 16] \times 4\sigma_{\rm rms}$, where $\sigma_{\rm rms} = 15$ μJy beam $^{-1}$. The beam size is $32'' \times 24''$ (shown bottom left) (B17).

the cone is connected to the NE wing via slim X-ray bridge. A linear surface brightness edge at the SE direction is present and believed to be associated with the SR. In the SW direction, two pockets of surface brightness deficit regions are present forming bays. These features are marked and shown on the right in Figure 3.5.

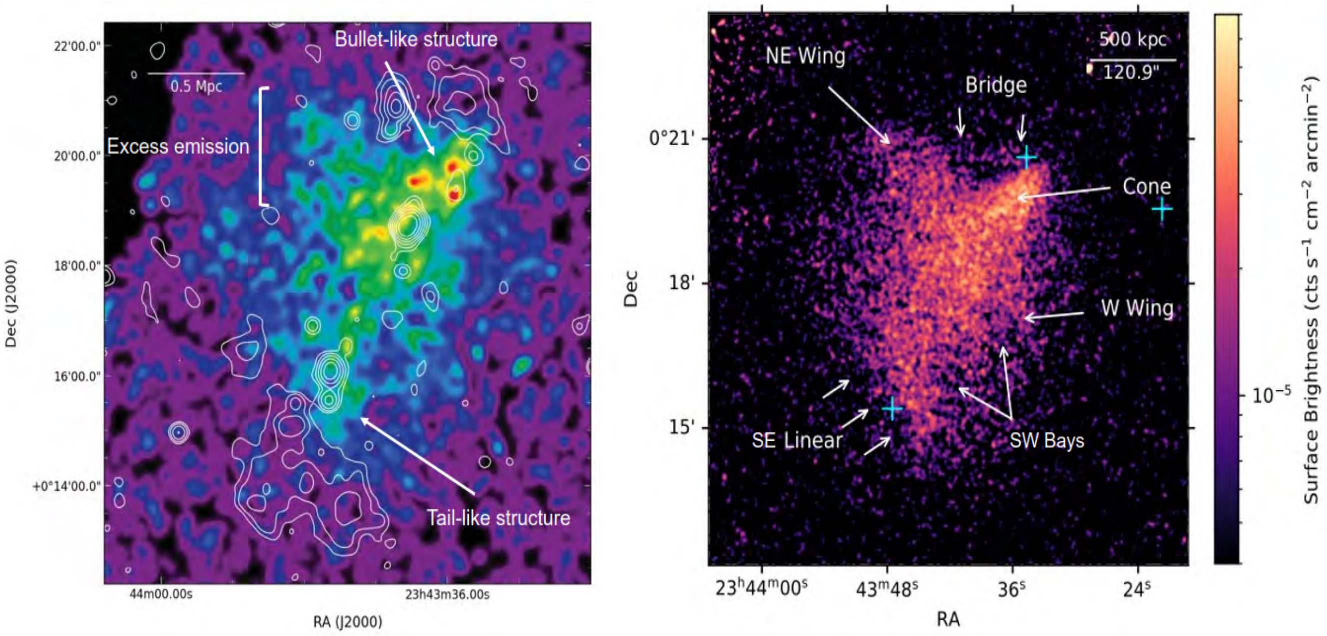

Figure 3.5: Recent X-ray observations of ZwCl 2341. *Left*: Chandra surface brightness map in the energy band 0.5 – 3.0 keV smoothed with a Gaussian kernel of 3 × 3 pixels (1 pixel = 1.97″) overlayed with the radio contours from V09. The spatial scale is shown at the top left (Ogrean et al., 2014). *Right*: Chandra surface brightness map in the energy band 0.5 – 2.0 keV band smoothed with a Gaussian kernel of 4 × 4 pixels (1 pixel = 1.97″). The main X-ray substructures are labelled with white arrows. The location of the three brightest cluster members are marked with cyan crosses. The spatial scale is shown at the top right (Zhang et al., 2021).

3.3 New MeerKAT and uGMRT observations

We have conducted pilot observations on the central part of the *Saraswati* supercluster which hosts the two massive galaxy clusters, A2631 and ZwCl 2341 with the MeerKAT telescope at 1283 MHz. We have then done a follow-up observation of ZwCl 2341 with uGMRT at 675 MHz. These newer and more sensitive observations have been able to build upon the existing knowledge gained from previous observations in terms of their radio environments. This is especially true for ZwCl 2341.

3.3.1 MeerKAT observation

We have used the MeerKAT telescope to observe the clusters ZwCl 2341 and A2631 at L-band (1283 MHz) (PI: Viral Parekh). These two massive galaxy clusters are situated near the core of *Saraswati*, separated by 1.5° and are surrounded by a filamentary network of galaxies. Each cluster was observed for 7 hours with 4k channels and 856 MHz bandwidth using 60 out of the total 64 MeerKAT antennas, with the standard MeerKAT primary and secondary calibrators. These included J1939-6342 as the primary calibrator for the bandpass and flux calibration and J2357-1125 as the secondary calibrator for the gain calibration. The observation information, including some of the calibrator properties, is shown in Table 3.1.

The absolute flux scale of J1939-6342 is 14.90 Jy at the rest frequency of 1.4 GHz. To confirm the flux density of the secondary calibrator we bootstrap from the primary calibrator. After bootstrapping the flux density scale from the flux calibrator (primary calibrator), the flux density of the secondary calibrator J2357–1125 was (2.07 ± 0.01) Jy at 1.28 GHz. We found the flux density of this calibrator source to be 1.80 Jy at 1.5 GHz on the VLA calibrator list[*]. If we assume $\alpha = -0.7$, then after extrapolation, the flux density at 1.28 GHz is $\sim$ 2.01 Jy.

The results from these pilot observations have recently been published under MOSS I: Double radio relics in the *Saraswati* supercluster (Parekh et al., 2021, hereafter P21). This is the first paper of the series: *MeerKAT Observations of the Saraswati supercluster (MOSS)*. This project

---

[*] `https://science.nrao.edu/facilities/vla/observing/callist`

is a three paper series which attempts to explore, map and study the radio environments existing within this rich, dense and peculiar supercluster environment. The remaining papers MOSS II and MOSS III will cover a range of topics within the *Saraswati* supercluster including merger shock properties, broadband spectral index studies of diffuse radio sources as well as radio source identification, their properties and catalogue. The details of these future projects are discussed in §6. The observation details for the two MeerKAT pointings on the two clusters ZwCl 2341 and A2631 are shown in Table 3.1. We show the *uv* distribution and *uv* vs amplitude plots for the MeerKAT observations of ZwCl 2341 and A2631 in Appendix §H.

3.3.2 uGMRT observation

ZwCl 2341 was then observed for 8 hours with uGMRT band-4 (550 – 850 MHz) using 4k channels for 8 hours (PI: Robert Kincaid, Project Code: 40-056). The main motivation behind this observation was to utilise the broad-bandwidth and low-frequency bands of the uGMRT to detect radio emission in between double radio relics in ZwCl 2341. The low-frequency nature of uGMRT (50 – 1450 MHz) combined with MeerKATs mid- to high-frequency coverage in L-band (900 – 1670 MHz) and the convenient band overlap makes it the perfect instrument for combined spectral studies with MeerKAT on extended sources, such as relics. Low-frequency observations are also advantageous for imaging relics since these sources are generally characterised by a steep spectrum that therefore appear more luminous at lower frequencies (Feretti et al., 2012). This observation made use of 28 of the total 30 GMRT antennas and utilised the standard primary and secondary calibrators used for GMRT/uGMRT observations. The primary calibrators included 3C48 and 3C147 for the bandpass and flux calibration, respectively. 2225-049 was used as the seconday calibrator for the gain calibration. The observation details for this single uGMRT pointing on ZwCl 2341 is shown in Table 3.2.

Our future plans for this data will be to combine it with our current MeerKAT L-band data in order to write a second follow-up paper to the MOSS series, MOSS II: Spectral analysis of double relics in *Saraswati* supercluster. We wish to conduct spectral analyses on the relics in ZwCl 2341 over a wide frequency range.

Table 3.1: MeerKAT observations of the *Saraswati* supercluster.

Observation date:	2019-06-15
Observation time:	00:41:27.8
Number of pointings:	2
Phase centre of A2631 (J2000):	RA: $23^{\rm h}37^{\rm m}40.60^{\rm s}$, DEC: $+00^\circ16'36.0''$
Phase centre of ZwCl 2341 (J2000):	RA: $23^{\rm h}43^{\rm m}39.70^{\rm s}$, DEC: $+00^\circ19'51.0''$
Number of antennas:	60
Total observation time:	14 hours
Central frequency:	1283 MHz
Total bandwidth:	900 MHz
Channel width:	208 kHz
Total number of channels:	4016
Dump time:	16s
Cross products:	XX, XY, YX, YY
Band pass and flux calibrator:	J1939-6342
J1939-6342 coordinates (J2000):	RA: $19^{\rm h}39^{\rm m}25.02^{\rm s}$, DEC: $-63^\circ42'45.62''$
J1939-6342 flux density at 1.4 GHz:	$\sim$ 14.90 Jy
Gain calibrator:	J2357-1125
J2357-1125 coordinates (J2000):	RA: $23^{\rm h}57^{\rm m}31.25^{\rm s}$, DEC: $-11^\circ25'38.90''$
J2357-1125 flux density at 1.4 GHz:	$\sim$ 1.80 Jy

Table 3.2: uGMRT observations of ZwCl 2341.

Observation date:	2021-05-23
Observation time:	04:00:0
Number of pointings:	1
Phase centre of ZwCl 2341	RA: $23^h43^m39.70^s$, DEC: $+00°19'51.0''$
Number of antennas:	28
Total observation time:	8 hours
Central frequency:	675 MHz
Total bandwidth:	400 MHz
Channel width:	97.65 kHz
Total number of channels:	4096
Dump time:	10.7s
Cross products:	LL, LR, RL, LL
Bandpass calibrator:	3C48
3C48 observation time:	15 minutes
3C48 coordinates (J2000):	RA: $01^h37^m41.2^s$, DEC: $+33°09'35.1''$
3C48 absolute flux density at 1.4 GHz:	16.50 Jy
Flux calibrator:	3C147
3C147 observation time:	15 minutes
3C147 coordinates (J2000):	RA: $05^h42^m36.10^s$, DEC: $+49°51'07.2''$
3C147 absolute flux density at 1.4 GHz:	22.5 Jy
Gain calibrator:	2225-049
2225-049:	5 minutes
2225-049 coordinates (J2000):	RA: $22^h25^m47.20^s$, DEC: $-04°57'01.30''$
2225-049 absolute flux density at 1.4 GHz:	6.42 Jy

Chapter 4

Results

The details for our new MeerKAT observations of A2631 and ZwCl 2341 including the follow-up uGMRT observations of ZwCl 2341 were discussed in §3.3. The `CARACal` and `SPAM` data-reduction pipelines (discussed in §2.5) were used to reduce our MeerKAT and uGMRT data, respectively. The raw data obtained from the MeerKAT observations were in MeerKAT Visibility Format version 4 (MVFv4)*. MVFv4 is the internal format used to store MeerKAT visibility data. MVFv4 was then converted into MS format via the `CASA` command `exportuvfits` for use in the `CARACal` pipeline. The total raw visibility MeerKAT data size for the A2631 and ZwCl 2341 observations was ~ 1.2 TB. After splitting the target sources and 10 channel averaging the size reduced to ~ 700 GB and ~ 450 GB for ZwCl 2341 and A2631, respectively. For uGMRT, we obtained our raw data in Long Term Accumulation (LTA) format, which was converted into UVFITS format through the `convert_lta_to_uvfits` option in `SPAM`, which is required for further processing. In both the `CARACal` and `SPAM` runs, we used `WSClean` to deconvovle and image the target fields with the multiscale and wideband deconvolution algorithms (`-join-channels` and `-channels-out`) enabled to allow better imaging of diffuse emission. We also used Briggs weighting of robust 0 (`-weight briggs 0`) to give equal sensitivity to imaging large and small scale structures.

For our `CARACal` run on MeerKAT data, imaging and deconvolution was performed after initial flagging and 1GC. We used an initial high mask of $30\sigma_{\rm rms}$ (using `-auto-mask`) to generate the artefact-free 1st order skymodel of the target field for the self-calibration process. Three rounds of phase-only self-calibration were performed. The masking threshold was iteratively reduced to a value of $3\sigma_{\rm rms}$ for generating the higher-order better skymodels during the self-calibration process. The highest-order skymodel (third round of self-cal) was derived from the `CARACal` final-calibrated DI (2GC) image. The time taken for flagging with `TriColour` was about ~ 20 minutes and the time taken to apply 1GC calibration was about ~ 30 minutes. The

---

*https://katdal.readthedocs.io/en/latest/mvf_v4.html time taken to generate the higher-order skymodels for each self-cal run with `WSClean` was about ~ 45 minutes.

For our `SPAM` run, the bulk of the data-reduction (flagging, 1GC, 2GC) were performed via the `process_wideband_to_target` command[†]. This took several days to complete. The end products consisted of six subbands of 2GC calibrated visiblities which were converted into an MS format for use in `WSClean` for the final wide-band and multiscale imaging. The number of subbands are related to the width of the frequency chunks which is automatically set to a sensible value by `SPAM`. The final imaging run combined these subband images producing the `SPAM` final-calibrated DI (2GC) image. The final-calibrated 2GC images from `CARACal` and `SPAM` are the subject of analysis for this results section.

4.1 3GC Calibration results

In this section, we show the 3GC calibration results of wide-band MeerKAT data through application of the two different methods of DD calibration, namely `CubiCal` and `killMS` on our `CARACal` final self-calibrated (2GC) MeerKAT visibilities of ZwCl 2341 and A2631, in order to improve image quality. These two 3GC software packages, `CubiCal` and `killMS`, were discussed in detail in §2.4.3 and §2.4.4, respectively.

The results after applying these 3GC methods to our 2GC calibrated images of ZwCl 2341 and A2631 are shown in Figures 4.1 and 4.2, respectively. The full-field images are shown in the left panel and zoomed-in regions on the right panel. The zoomed region for ZwCl 2341 on the right panel of Figure 4.1 attempts to highlight the improvement around source A (after DD calibration) which is situated in close proximity to the double radio relic system. For A2631, this system hosts no large scale diffuse emission and its zoomed region is included attempting to highlight source improvement of sources A and B (after DD calibration). In both figures, we initially display the `CARACal` DI calibrated images in the top panel and move down to the DD calibrated images for `CubiCal` (middle) and `killMS` (bottom), respectively. These images

---

[†] The full uGMRT wide-band data-reduction process, including all `SPAM` commands, are shown at: `http://www.intema.nl/doku.php?id=huibintemaspampipeline`.

illustrate the visual improvements of the DD calibration techniques implemented by the `CubiCal` and `killMS` software.

The improvement of each selected source was then statistically quantified using $8' \times 8'$ cutout regions of the DI and DD images around each source as shown in Figure 4.3 and Figure 4.4. A standard set of statistical parameters were used in our analysis for each cutout region and full-image and we show these results in Tables 4.2 and 4.3. These statistical parameters were discussed in §2.6.3. Trends in certain parameters exist directly relating to the artefact reduction causing significant image quality improvement. We have also included flux density comparisons of the compact radio sources residing in these two cluster fields before and after application of the DD methods which are shown in Figure 4.5.

4.1.1 Dynamic range improvements

After careful inspection of the `CARACal` DI calibrated full-field images of ZwCl 2341 and A2631 shown in the top left image of Figures 4.1 and 4.2, respectively; we identify several strong and problematic sources generating significant artefacts in a localised region surrounding their centres. Some of the sources are also affecting a large portion of the image, resulting in high RMS noise and poor image quality. The strongest sources were manually marked with a yellow square (top left images of Figures 4.1 and 4.2) and labelled according to their distances from their respective phase centres (near to far). We have selected five strong artefact-producing sources in the ZwCl 2341 labelled with A-E, and three for A2631, labelled with A-C. We have tabulated the positions and flux densities with errors of these selected sources in Table 4.1. Nearly all the flux density values of the sources selected in both fields are over 40 mJy. The three sources selected in A2631 were, on average, further from the phase centre than the sources selected in ZwCl 2341. We have applied 3GC calibration techniques through the `killMS` and `CubiCal` software and subsequent imaging with `DDFacet` in order to reduce the artefacts from these sources and improve overall image fidelity. The resultant images after the simultaneous peeling method of `CubiCal` applied to the `CARACal` DI calibrated images (top panel of Figures 4.1 and 4.2) for ZwCl 2341 and A2631, respectively; are shown in the middle panel of these figures. The facet-based calibration method of `killMS` applied to the same `CARACal` DI calibrated images is shown at the bottom panel of the same figures. All the DD calibrated images (middle and bottom images of Figures 4.1 and 4.2) show clear improvements evident by the visual reduction in artefacts. `killMS` took about 7-8 hours to apply the facet-based 3GC calibration and `CubiCal` took about 8-9 hours to apply 3GC peeling calibration technique. The final `DDFacet` imaging run on these 3GC corrected data took about 7-8 hours.

Table 4.1: Tabulated details for the selected sources in ZwCl 2341 and A2631. The ZwCl 2341 sources are labelled in the top left of Figure 4.1. The ones for A2631 are labelled in the top left of Figure 4.2.

Cluster	Source	RA	DEC	Flux density and error	Distance from phase centre
		H :M :S	D :M :S	mJy	arcmin
ZwCl 2341	A	23:59:42.4869	+00:00:27.59	84.74 ± 0.07	8.6
	B	23:59:43.2813	+00:00:32.46	39.87± 0.06	12.4
	C	23:59:43.3261	+00:00:47.31	84.44± 0.43	26.1
	D	23:59:42.2449	+00:00:51.93	151.17± 3.37	31.1
	E	23:59:40.2251	+00:00:19.43	460.56± 0.57	38.3
A2631	A	23:59:35.2787	+00:00:02.51	125.32± 0.74	24.2
	B	23:59:37.5032	+00:00:46.09	114.94± 0.30	30.7
	C	23:59:40.2246	+00:00:19.44	68.76± 0.27	51.4

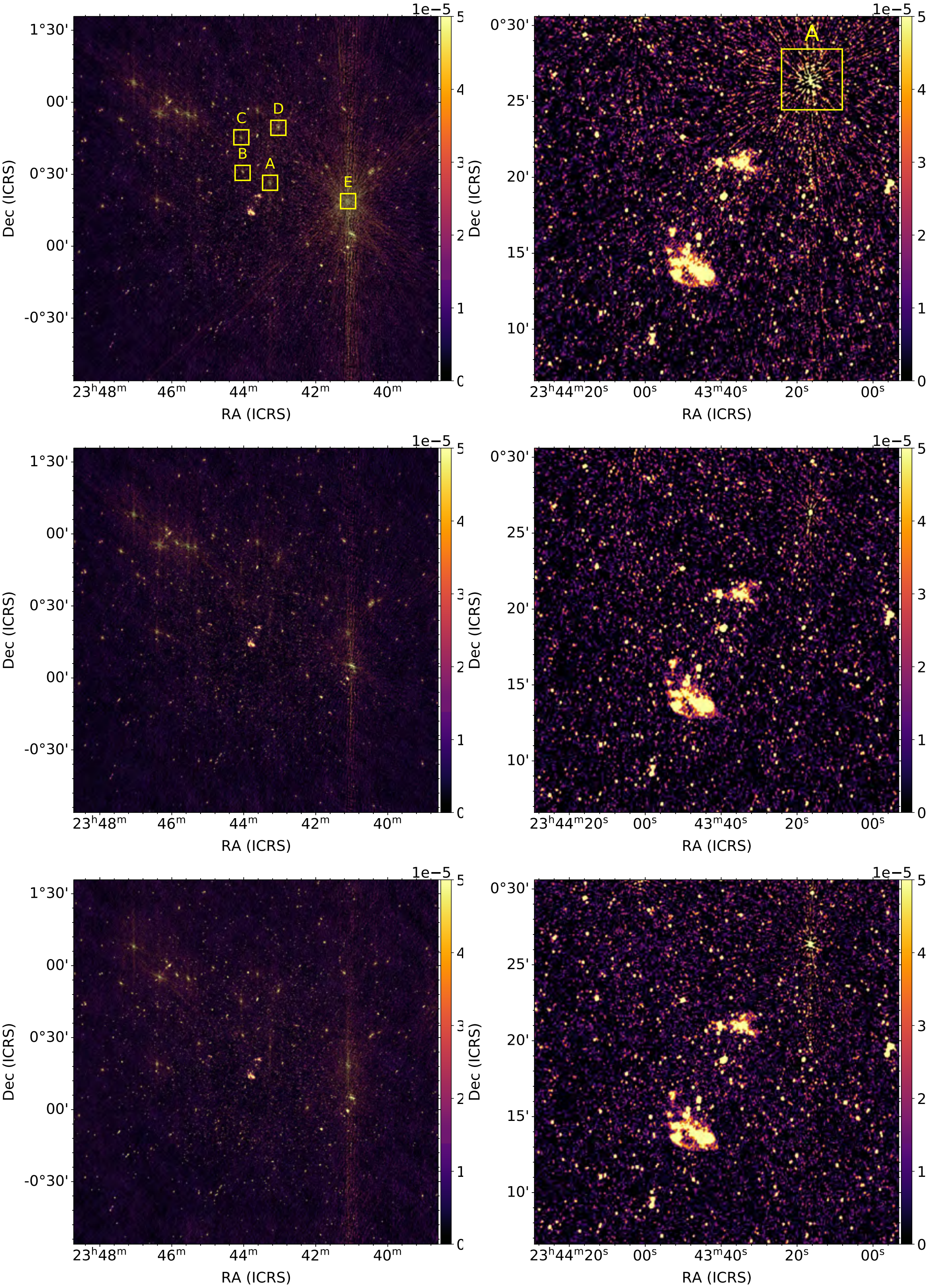

Figure 4.1: ZwCl 2341 before and after `CubiCal` and `killMS` DD calibration. *Top*: The left image shows the DI ZwCl 2341 full-field image with the prominent bright sources labelled using A-E alphabets. The right image is the 0.4° × 0.4° central zoomed image of the left. *Middle*: `CubiCal` generated DD full-field (left) and zoomed (right) images. *Bottom*: `killMS` generated DD full-field (left) and zoomed (right) image.

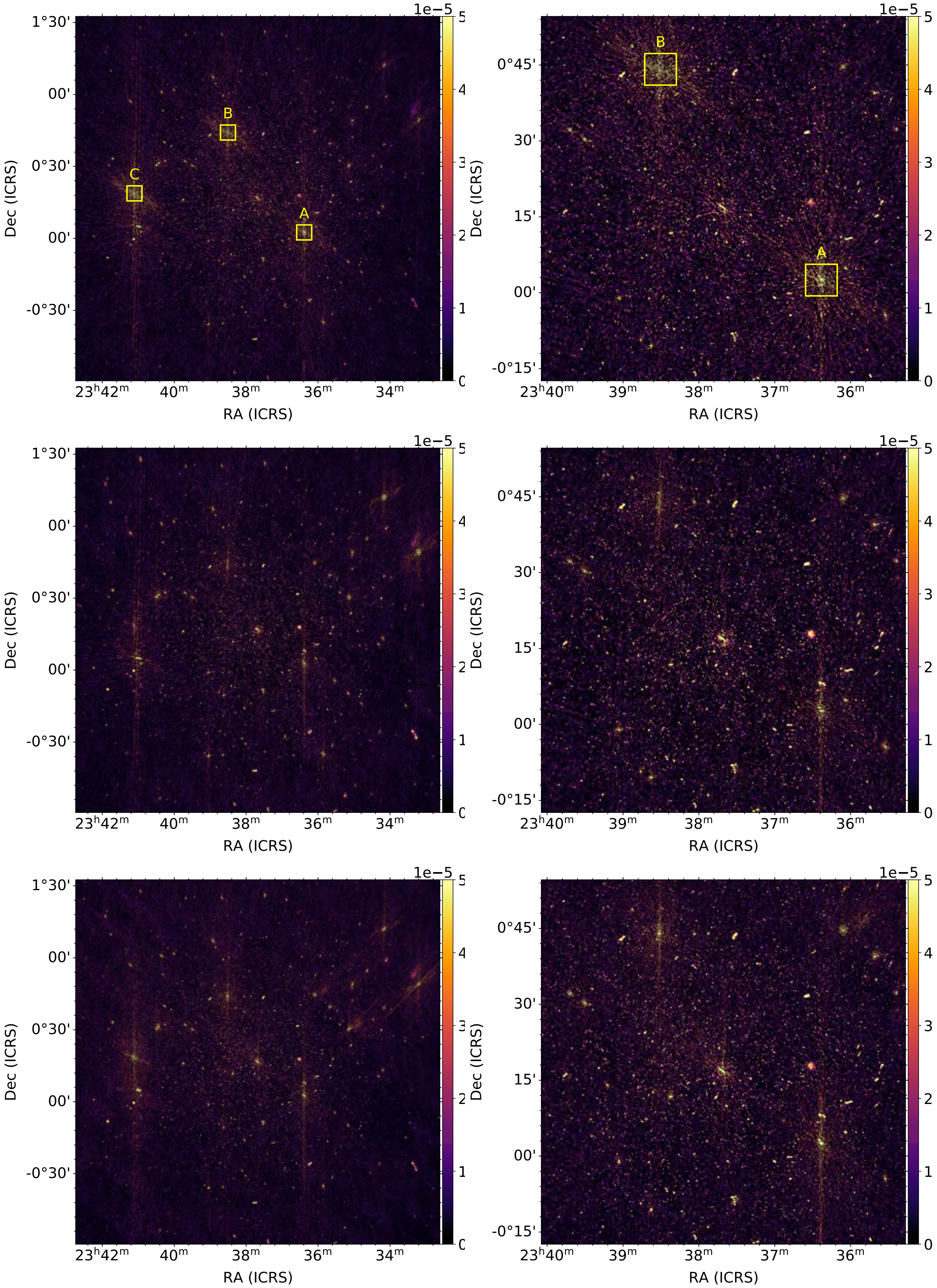

Figure 4.2: A2631 before and after `killMS` and `CubiCal` DD calibration. *Top*: The left image shows the DI A2631 full field image with the prominent bright sources labeled using A-C alphabets. The right image is the 1° × 1° central image of the left. `Middle`: `CubiCal` generated DD full-field (left) and zoomed (right) images. `Middle`: `killMS` generated DD full-field (left) and zoomed (right) image.

4.1.2 Statistical studies

In Figures 4.3 and 4.4, we show $8' \times 8'$ cutouts of the five strong sources identified in ZwCl 2341 (labelled A to E in the top left panel of Figure 4.1) and three strong sources identified in A2631 (labelled A to C in the top left panel of Figure 4.2), respectively. In Figures 4.3 and 4.4, from top to bottom row, the left column contains the square region cutouts for the `CARACal` generated DI images of the selected sources (top panel of Figure 4.1 and Figure 4.2); the middle column contains DD images generated with the `CubiCal` (middle panel of Figure 4.1 and Figure 4.2) and the right column contains DD corrected images generated with the `killMS` (bottom panel of Figure 4.1 and Figure 4.2). We calculated statistics (before and after applying DD calibration) in these $8' \times 8'$ square region cutouts of every marked source. We listed these statistical results in Tables 4.2 and 4.3 for both the cutout regions and full-field image (last row).

The chosen statistical parameters include RMS, MIN, sum of negative pixels (SUM NEG), MAD, SKEW, KURT and NORM, which were calculated from the residual images (mostly background noise component of the image). The MAX values were found from restored images since the restored images contain both the noise (background) and foreground components, where the latter contains the highest valued pixels. For the DR (see Equation 2.22), we have used this MAX value for the peak flux. In calculating the DR for `CubiCal` DD images, since `CubiCal` peels sources, hence reducing their peak flux densities in restored images; we therefore used the MAX value of corresponding DI image.

We have included the SUM NEG in our statistical analysis as a result of the positive-negative pattern manifested in imaging artefacts generated by calibration errors. This is a direct result of the positive-negative pattern of the PSF side-lobes. True astrophysical compact source emission is all positive, therefore we can use this parameter to directly measure the number of negative pixels representing the artefacts.

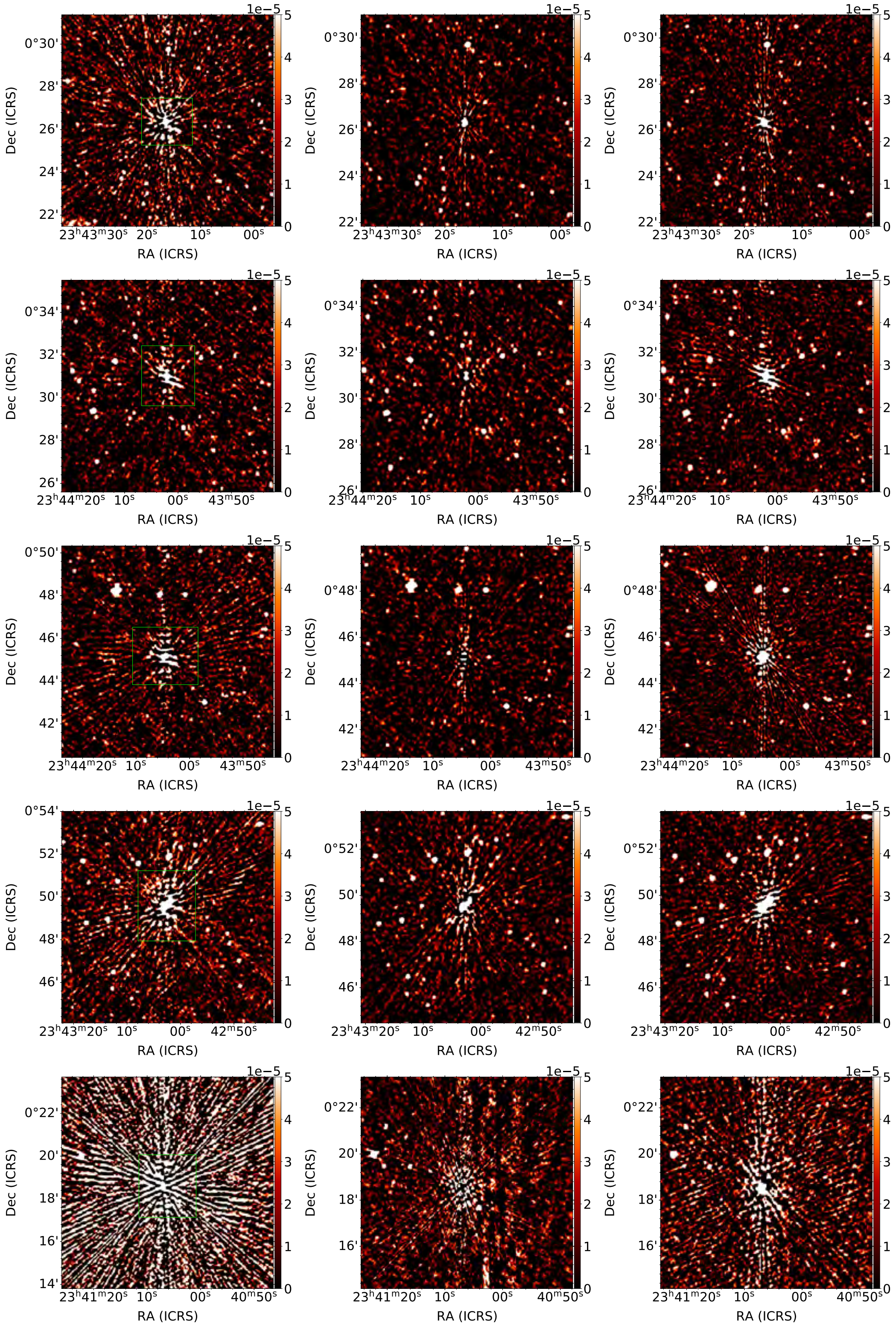

Figure 4.3: 8′ × 8′ square region cutouts of the five bright sources A, B, C, D and E from top to bottom, respectively, corresponding to the labeled sources in ZwCl 2341 at the top left image of Figure 4.1. The left panel contains the DI calibrated images and the middle and right panels contain the `CubiCal` and `killMS` DD calibrated images, respectively.

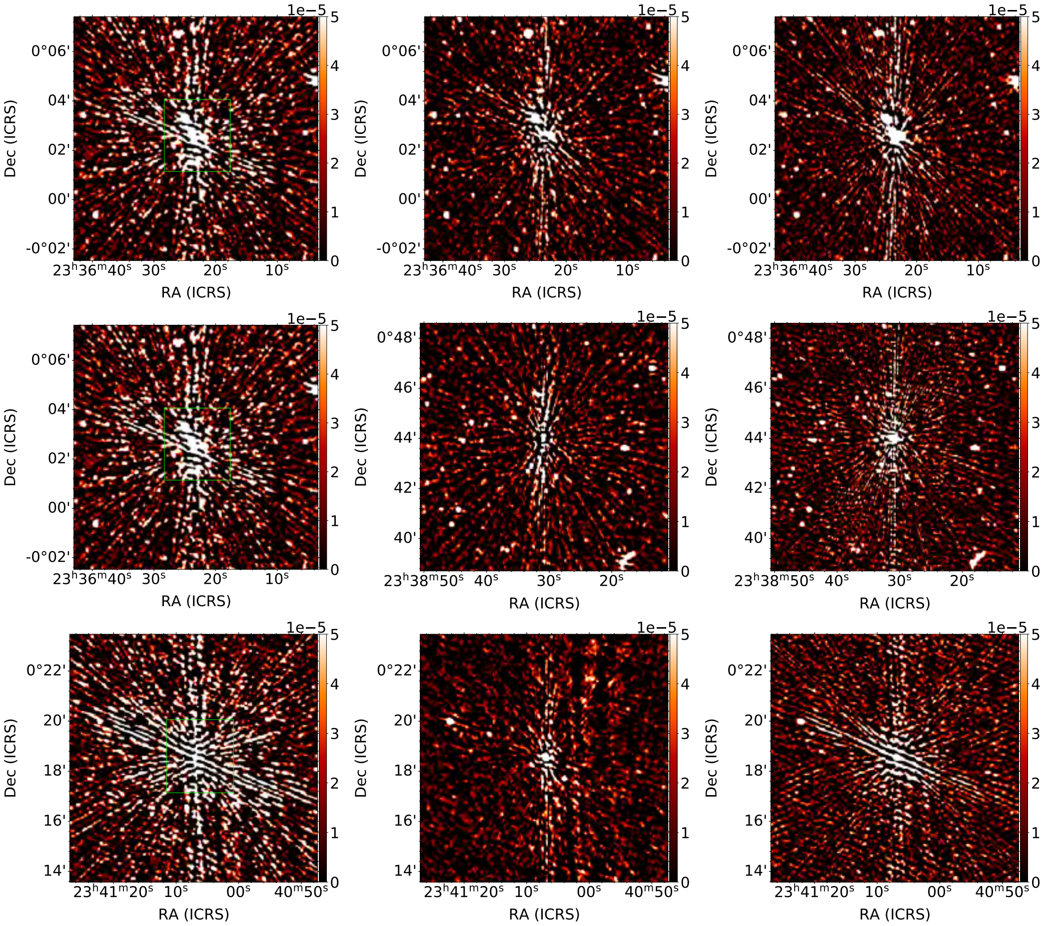

Figure 4.4: 8′×8′ square region cutouts of the three bright sources A, B and C from top to bottom, respectively, corresponding to the labelled sources in the top left image of Figure 4.2. The left panel contains the DI calibrated images and the middle and right panels contain the `CubiCal` and `killMS` DD calibrated images, respectively.

Table 4.2: Statistics calculated from residual and restored images, before and after `CubiCal` and `killMS` calibration, for the five $8' \times 8'$ square region cutouts of the bright sources A, B, C, D and E residing in ZwCl 2341 labelled in the top left image of Figure 4.1.

Source	RMS μJy beam^{-1}	DR1	DR2	DR3	MAD μJy beam^{-1}	MIN mJy beam^{-1}	MAX mJy beam^{-1}	SUM NEG mJy beam^{-1}	SKEW	KURT	NORM
A											
DI	37.0	2288.95	66.77	4282.69	15.0	-1.27	84.61	-1170.39	-6.59	175.62	132287.84
DD (CubiCal)	16.0	5384.67	521.17	6011.81	9.0	-0.16	1.93	-642.60	1.2	12.53	32982.4
DD (killMS)	18.0	4819.0	207.25	6728.32	8.0	-0.41	84.35	-648.68	-2.19	61.92	68730.32
B											
DI	23.0	1452.71	89.54	1703.88	11.0	-0.38	33.66	-780.03	1.26	41.87	48327.62
DD	17.0	1948.45	203.95	2391.82	9.0	-0.17	1.11	-640.55	1.53	13.83	40406.3
DD	19.0	1729.23	89.72	2616.98	8.0	-0.37	32.80	-525.23	0.78	63.84	43861.46
C											
DI	37.0	859.03	35.10	1587.62	12.0	-0.89	31.37	-974.88	2.47	161.56	81404.9
DD	18.0	1786.54	123.52	2228.62	9.0	-0.25	3.19	-683.07	0.56	23.3	29623.6
DD	23.0	1329.44	39.44	2416.91	9.0	-0.77	30.30	-647.93	-6.74	207.55	134959.27
D											
DI	38.0	823.34	39.83	1596.63	15.0	-0.79	31.54	-1009.09	-1.06	91.05	52000.85
DD	24.0	1335.30	57.60	2241.26	10.0	-0.55	2.09	-668.20	-3.96	86.19	97598.32
DD	23.0	1293.42	52.52	2414.77	9.0	-0.58	30.27	-672.90	-4.67	102.88	107886.23
E											
DI	201.0	903.81	31.46	9191.59	47.0	-5.77	181.59	-4077.27	-5.1	196.17	117774.02
DD	30.0	6097.83	237.53	12902.67	14.0	-0.76	2.60	-895.05	0.29	76.61	38640.5
DD	36.0	4446.85	233.40	12927.69	17.0	-0.69	162.08	-1178.32	-1.13	33.72	43613.94
Full image											
DI	20.0	-	31.46	9191.59	9.0	-5.77	181.59	-196953.75	-15.45	5995.31	75889133.95
DD	14.0	-	115.12	12902.67	7.0	-1.58	42.21	-154531.51	-1.59	636.36	26984110.13
DD	12.0	-	122.20	12927.69	7.0	-1.33	162.08	-154750.56	-4.86	531.9	43647231.04

Table 4.3: Statistics calculated from residual and restored images, before and after `CubiCal` and `killMS` calibration, for the three $8' \times 8'$ square region cutouts of the bright sources A, B and C residing in A2631 labelled in the top left image of Figure 4.2.

Source	RMS μJy beam^{-1}	DR1	DR2	DR3	MAD μJy beam^{-1}	MIN mJy beam^{-1}	MAX mJy beam^{-1}	SUM NEG mJy beam^{-1}	SKEW	KURT	NORM
A											
DI	113.00	1019.06	50.87	3386.88	26.00	-2.26	115.15	-2262.99	4.81	165.63	113300.30
DD (CubiCal)	41.00	2808.63	197.73	8225.29	13.00	-0.58	24.85	-1098.21	5.27	140.33	117121.63
DD (killMS)	49.00	2350.08	103.44	8858.00	13.00	-1.11	118.76	-1025.85	9.73	272.35	161638.64
B											
DI	147.00	635.17	20.34	2746.20	29.00	-4.59	93.37	-2723.74	-2.73	219.55	87705.30
DD	29.00	3219.68	145.28	6669.34	12.00	-0.64	3.27	-915.62	-3.46	76.43	89893.76
DD	38.00	2457.12	56.37	7182.36	14.00	-1.66	111.71	-999.97	-7.86	287.71	147099.15
C											
DI	183.00	364.42	15.19	1961.46	34.00	-4.39	66.69	-3413.99	-1.71	167.82	68757.28
DD	21.00	3175.70	186.61	4763.55	11.00	-0.36	17.57	-703.06	-0.22	19.27	23577.29
DD	52.00	1282.49	50.50	5129.98	16.00	-1.32	92.31	-1260.43	-6.14	131.90	125776.35
Full image											
DI	34.00	3386.88	25.09	3386.88	11.00	-4.59	115.15	-218989.44	66.93	17292.70	105893065.48
DD	14.00	8225.29	99.47	8225.29	7.00	-1.16	50.93	-132826.45	2.78	531.13	27684269.29
DD	13.00	8858.00	69.53	8858.00	7.00	-1.66	118.76	-130594.99	-0.90	532.10	18114006.19

4.1.3 Flux density comparison

We compared the flux densities of compact radio sources before and after DD calibration to study the effect of the different DD calibration methods implemented by the `killMS` and `CubiCal` software on these sources. We manually selected noticeable point-like sources covering the FoV of ZwCl 2341 and A2631 for the DI calibrated and DD calibrated apparent images (non-primary beam corrected image) using `CASA` viewer. We then used the `CASA` `imfit`[†] task to compute the flux densities. This task fits one or more elliptical Gaussian components to the selected regions to measure the flux and other properties.

In total, 425 sources were selected when combining the `CASA` selected regions for A2631 and ZwCl 2341. In Figure 4.5, we show the computed DI vs DD plots for `CubiCal` (top) and `killMS` (bottom) for the combined point sources of both ZwCl 2341 and A2631. Both plots show a strong relationship between the flux densities before and after DD calibration with most points following the correlation indicated by the solid black best-fit line. The point sources in the DI vs DD `CubiCal` calibrated plot fit the correlation very well whereas for the DI vs DD `killMS` plot, there is some scatter about this best fit correlation line. We have calculated the slope m and coefficient of determination R^2 value for the DI vs DD `CubiCal` and `killMS` plots. These values are printed on the top left of each plot in Figure 4.5. The R^2 value gives an indication of how well our points fit the correlation. For the DI vs DD `CubiCal` plot, $m = 0.99$ and $R^2 = 0.99$; these indicate an almost perfect fit of the data. For the DI vs DD `killMS` plot, $m = 0.90$ and $R^2 = 0.97$, the data points show some scatter about the correlation.

It is known that the flux density of point sources increase after applying DD calibration techniques due to added flux from calibrated related errors, including incomplete skymodel from unmodelled sources, short solution intervals, low-level RFI, and so forth, to the model of these sources. We calculated the Fractional Increase (FI) after DD calibration using: $FI = \left|\frac{DD-DI}{DI}\right| \times 100$ for both `killMS` and `CubiCal` images. For the DI vs DD `killMS` plot, we found a larger increase of $FI_{killMS} \sim 20\%$ as compared to `CubiCal`, $FI_{CubiCal} \sim 5\%$. We also calculated the Coefficient of Variation (CV) for our `CubiCal` and `killMS` DD calibrated images to find the

---

[†] https://casa.nrao.edu/docs/taskref/imfit-task.html

dispersion around the mean for the flux density of these point sources. This quantity is defined as the ratio of the standard deviation to mean: $CV = s/\hat{x}$. For `killMS`, we found a slightly larger value of $CV_{killMS} = 1.99$ as compared to `CubiCal`, $CV_{killMS} = 1.82$.

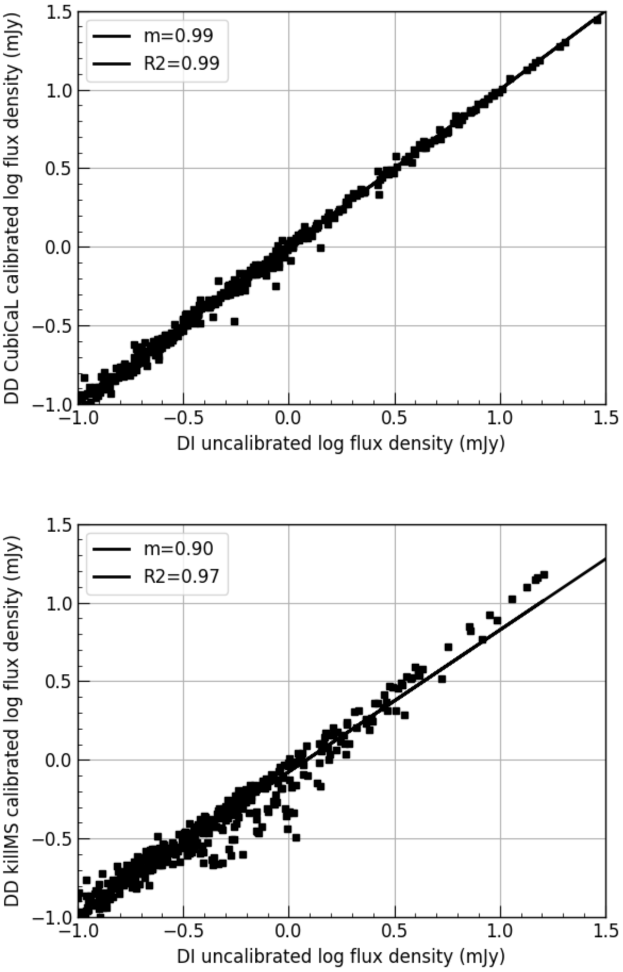

Figure 4.5: Flux density comparison plots for DI vs DD `CubiCal` (top) and DI vs DD `killMS` (bottom) for the combined point sources of the A2631 and ZwCl 2341 cluster fields. The slope m and regression R^2 value is shown in the top left of each plot.

4.2 Science results

As discussed in §3.4, double relics have already been discovered in ZwCl 2341 by V09, G10 and B17. These were further explored in the most recent publication of P21. In this section, we discuss our new MeerKAT and uGMRT observation and how it compares with the previous observations. We have used our new MeerKAT L-band (900–1670 MHz), uGMRT Band 4 (550-850 MHz) and archival legacy GMRT (325 MHz) to explore these double relics. We use their point source subtracted images to draw contours on optical and X-ray images shown in Figure 4.8.

We then use our new MeerKAT and uGMRT image to apply tapering to see whether we can recover the diffuse and faint radio source suspected to reside between the relics. We also see the effects of DD calibration for imaging of such faint and extended emission.

In the last section we explore in more detail the properties of the relics and central diffuse source by showing their 1D spectral index plot using MeerKAT data combined with uGMRT and finally derive the radio power.

4.2.1 Double radio relics of ZwCl 2341

Bright point sources around extended emission are notable for limiting the flux density of diffuse emission. We therefore, used point source subtracted (and DD calibrated for MeerKAT) images for our science analysis. We show our high-sensitive, point source subtracted MeerKAT (L-band, 900–1670 MHz), low-frequency uGMRT (Band 4, 550-850 MHz) and archival legacy GMRT (325 MHz) DI images in Figure 4.7. To obtain these images, we first produced a catalogue of sources using the `PyBDSF`[*] source finder software applied to our MeerKAT L-band data. `PyBDSF` decomposes an image into a set of Gaussian sources to identify point-like sources in an image and to calculate their properties. We used the default source finding properties of this software, which included an island threshold of $3\sigma_{\rm rms}$, pixel threshold of $5\sigma_{\rm rms}$ and a tolerance of $5''$. We labelled only the sources found by `PyBDSF` in a local region around the relics as shown at the

---

[*] https://www.astron.nl/citt/pybdsf/

top of Figure 4.6. Our selected sources total 28. These are the sources we used for subtraction. Similar point source subtraction was also performed in V09 and we show these sources on our MeerKAT 1283 MHz image at the bottom of Figure 4.6. Our selected point sources also include the ones from V09. We have listed the position and fluxes of our selected point sources in Table 4.4. These sources were then subtracted from our MeerKAT, uGMRT and GMRT visibilities using the `Crystalball` source subtraction technique discussed in §2.6.1. The input visibility used for MeerKAT was the `CubiCal` DD calibrated visibility. For uGMRT, we used the DI visibility subbands generated from `SPAM` and for the archival legacy GMRT data, we used the `CARACal` generated DI visibility, The subtracted visibilities after the `Crystalball` procedure were then all imaged with `WSClean`. We show these point source subtracted images in Figure 4.7. The MeerKAT, uGMRT and GMRT are shown at the top, bottom left and bottom right, respectively.

We have used the point source subtracted MeerKAT L-band image at the top of Figure 4.7 for the radio component to plot contours over multi-frequency optical and X-ray images of ZwCl 2341, shown at the top of Figure 4.8. The optical and X-ray components are displayed using a combination of red, green, blue (RGB) to represent the different frequency components. The Chandra smoothed X-ray data is shown in red and DECaLS DR9 optical data is shown using a combination of green and blue. The radio contours are shown in white. We have then used this same MeerKAT L-band image to plot the radio intensity in colour, which we then overlay with radio contours (shown in yellow) from the GMRT and uGMRT point source subtracted images. We show these images at the bottom left and right panels of Figure 4.8, respectively.

In the MeerKAT image at the top of Figure 4.8, the double relics of NR and SR, confirmed by the previous observations of V09, G10 and B17 are clearly evident. They are located perpendicular to the north-south merger axis. They encapsulate the bright X-ray ICM shown in red and lie at the periphery where this X-ray emission terminates. Both relics have a regular symmetric structure, slightly deviating from the usual elongated arc-like structure attributed to relics. For the MeerKAT colour radio image overlayed with radio contours of GMRT and uGMRT at the bottom of Figure point source subtracted images, the contours of both GMRT and uGMRT follow the MeerKAT radio image. The GMRT contours in the bottom left image of Figure 4.8 recover more emission for the eastern part of the SR, while the uGMRT contours for the bottom right image of Figure 4.8 recover more emission for the eastern part of the NR.

The radio contours in all three images show that the SR is larger and more elongated than the NR. The morphology of the SR is more round and smoother than the NR. Properties such as relic size, flux density, beam sizes and σ_{rms} for the GMRT (325 MHz), uGMRT (675 MHz) and MeerKAT (1283 MHz) observations for the radio images of Figure 4.7 are given in Table 4.6. From this table, the relic sizes and flux densities are slightly larger in the lower frequency GMRT 325 MHz data as compared to the higher frequency uGMRT 675 MHz and MeerKAT 1283 MHz data. A factor contributing to this slight increase in physical size and flux density is due to spectral steepening at lower frequencies (van Weeren et al., 2019).

Table 4.4: List of point sources subtracted from the ZwCl 2341 data as labelled in the image at the bottom of Figure 4.6.

Point source	RA H:M:S	Declination D:M:S	Flux density and error mJy	Peak flux mJy
A1	23:59:42.8872	+00:00:19.61	15.64 ± 1.11	4.68
A2	23:59:42.9204	+00:00:19.33	0.21 ± 0.04	0.16
A3	23:59:42.8914	+00:00:18.78	0.42 ± 0.02	0.36
A4	23:59:42.8524	+00:00:18.28	0.27 ± 0.02	0.28
A5	23:59:42.8009	+00:00:17.81	0.18 ± 0.01	0.16
A6	23:59:42.8008	+00:00:16.27	0.21 ± 0.01	0.19
A7	23:59:42.7724	+00:00:15.16	0.27 ± 0.02	0.24
A8	23:59:42.6137	+00:00:16.96	0.74 ± 0.02	0.69
A9	23:59:42.6346	+00:00:17.69	0.26 ± 0.02	0.27
A10	23:59:42.7895	+00:00:20.95	0.25 ± 0.01	0.20
A11	23:59:42.8036	+00:00:21.60	0.60 ± 0.02	0.55
A12	23:59:42.8312	+00:00:21.83	0.47 ± 0.05	0.23
A13	:23:59:42.8493	+00:00:21.60	0.16 ± 0.02	0.13
A14	23:59:42.8439	+00:00:22.72	0.26 ± 0.01	0.28
A15	23:59:42.9025	+00:00:21.88	4.55 ± 0.45	2.06
A16	23:59:42.9094	+00:00:21.47	0.85 ± 0.02	0.80
A17	23:59:42.9652	+00:00:21.63	0.41 ± 0.02	0.32
A18	23:59:43.0725	+00:00:23.75	7.14 ± 0.06	6.93
A19	23:59:43.1752	+00:00:19.42	0.25 ± 0.02	0.24
A20	23:59:43.2207	+00:00:15.70	1.01 ± 0.02	0.98
A21	23:59:43.0643	+00:00:15.82	1.00 ± 0.12	0.36
A22	23:59:43.0461	+00:00:15.85	0.96 ± 0.09	0.65
A23	23:59:43.0486	+00:00:16.26	1.01 ± 0.06	0.46
A24	23:59:43.0007	+00:00:16.31	1.27 ± 0.02	1.15
A25	23:59:42.9986	+00:00:16.90	2.92 ± 0.15	0.99
A26	23:59:43.0244	+00:00:17.7	0.40 ± 0.02	0.38
A27	23:59:42.9358	+00:00:16.43	0.21 ± 0.03	0.15
A28	23:59:43.0357	+00:00:14.68	0.48 ± 0.04	0.30

4.2.2 Potential diffuse halo present in ZwCl 2341

Low-resolution images from B02 and G10 have found large scale diffuse emission permeating the region between the two relics. In our high-resolution (`robust=0`), point source subtracted L-band MeerKAT and band-4 uGMRT observations of ZwCl 2341 with corresponding beam sizes of $8'' \times 6''$ and $4'' \times 3''$, respectively, we could not detect any large scale diffuse radio emission between two radio relics. We have applied a $50''$ uv-taper to the MeerKAT and uGMRT data to match the resolution of NVSS, where B02 and G10 have shown the possibility of an extended radio bridge between relics. A $50''$ Gaussian taper was applied to the point source subtracted DD calibrated (from `CubiCal`) MeerKAT image and DI calibrated (from `SPAM`) uGMRT image with `WSclean` using the option `-taper-gaussian`. These two $50''$ tapered images are shown at the bottom of Figure 4.9. For comparison, we have included the low-resolution images from B02 and G10. As one can see in the bottom images of Figure 4.9, there exists a marginal detection of a diffuse source, albeit only at the $2\sigma_{\rm rms}$ level. This extended emission resides between the two relics at a size of $\gtrsim 1$ Mpc in both the MeerKAT and uGMRT images.

In the MeerKAT observation, the emission is irregular and patchy in morphology. It almost forms into a single component between the relics. Its approximate size is $\sim 230'' \times 250''$ ($\sim 1 \times 1.1$ Mpc^2). In the uGMRT image, the diffuse emission does not easily assemble into one component as in the MeerKAT image but rather consists of two components; a central region and a tail as indicated in Figure 4.9. In the uGMRT image, the central emission joins the SR and its morphology is more patchy but not as irregular as compared to the MeerKAT image. Its approximate size (including tail component) is $\sim 222'' \times 273''$ ($\sim 1 \times 1.2$ Mpc^2). The tail component extends in a south-east direction with a size of $\sim 243''$. It is slightly smaller than the distance of $273''$ calculated between the relics in the uGMRT image, but comparable in size to $250''$, which is the distance between the relics in the MeerKAT image. The $\sigma_{\rm rms}$ for the MeerKAT and uGMRT images at the bottom of Figure 4.9 are $\sigma_{\rm rms} = 77\mu$ Jy beam^{-1} and $\sigma_{\rm rms} = 80\mu$ Jy beam^{-1}, respectively, which are slightly better than a factor of two for what was reported in the previous VLA 1.4 GHz observation of G10 and $5-7$ times larger than the VLA 325 MHz image of B02. However, G10 and B02 used different beam sizes of $83'' \times 75''$ and $108''$, respectively.

These earlier observations of B02 and G10 shown in the top panel of Figure 4.9 were not able to separate the emission from the northern and southern components due to their sensitivity constraints. There was also no such hint in the other higher-resolution images of V09, G10 and B17. Our high-resolution images of beam sizes $8'' \times 6''$, $10'' \times 7''$ and $4'' \times 3''$ for 1283 MHz MeerKAT, 325 MHz GMRT and 675 MHz uGMRT, respectively, also show no hint of diffuse emission between the relics. We also applied the same $50''$ tapering (not shown in this work) to the archival legacy GMRT 325 MHz image but no diffuse emission was detected at the $2\sigma_{\rm rms}$ level.

We have included a comparison between the $50''$ tapered MeerKAT DD and DI images to see the effects of DD calibration on imaging diffuse, faint and extended sources such as the one present in our low-resolution images. This comparison is shown in Figure 4.10. The top and bottom images show the low-resolution $50''$ tapered MeerKAT DI and DD images, respectively. The diffuse source in the DI image is sparse and disconnected, consisting of two components. After applying DD calibration, the two components connect almost forming a single component. This is a consequence of the $\sim 10\%$ improvement in $\sigma_{\rm rms}$ after DD calibration.

4.2.3 1-D Spectral index plots and 1.4 GHz radio power

We have used our 1283 MHz MeerKAT L-band, 675 MHz uGMRT Band-4 and archival legacy GMRT 325 MHz point source subtracted data (Figure 4.7) in conjunction with the measurement from V09 for the lower frequency 241 MHz component to derive a 1-D spectral index plot between the frequency ranges 241-1283 MHz, shown in Figure 4.11. We estimated the fluxes for our MeerKAT, uGMRT and GMRT data of the relics by manually drawing regions that trace the $3\sigma_{\rm rms}$ contours surrounding them. V09 has separated the south relic into three regions, namely RS-1, RS-2 and RS-3. The SR in our MeerKAT and uGMRT data encompass all three of these regions. As a result, we simply combined the RS-1, RS-2 and RS-3 flux density values of V09 when finding the flux density of the SR at 241 MHz.

After finding these flux densities, we had to match them to a common standard since our new observations used different standards for the flux calibrator as compared to V09. The MeerKAT, GMRT and uGMRT observations utilised the Perley & Butler (2017) (PB) and Scaife & Heald (2012) (SH) standards, respectively; while the lower frequency data of 241 MHz from V09 used Baars et al. (1977); hence we chose to scale our flux densities to the Baars standard by taking the ratio of Baars with PB and SH, and multiplying this ratio with our measured flux density values for MeerKAT, uGMRT and GMRT.

From our 1-D spectral index plot in Figure 4.11, we find a straight line fit for both relics. The NR has a better fit than the SR as all of its error bars make contact with the fitted line while only the first and last point make contact with the SR. The integrated spectral index for the NR is flatter $\alpha_{NR} = -0.70 \pm 0.08$ as compared to the SR, $\alpha_{SR} = -0.88 \pm 0.11$. We have tabulated the spectral index values and the frequency ranges from which were calculated from previous observations in Table 4.5, in order from oldest to new. Overall, our spectral index values are steeper than the earlier observations of B02 and V09 and flatter than the ones reported for G10, B17 and P21: $\alpha_{B17}, \alpha_{G10}, \alpha_{P21} < \alpha_{\rm Currentwork} < \alpha_{B02}, \alpha_{V09}$. In the recent analysis by P21, a break in the frequency was reported for the NR and we see no such evidence of this phenomenon in our analysis. The value reported in Table 4.5, therefore, uses the value they calculated assuming no break. In our plot, we have also included the spectra of the central diffuse source for the uGMRT

Table 4.5: Spectral index value compilation of double radio relics in ZwCl 2341 and their corresponding frequency ranges.

Frequency range	North relic (NR)	South Relic (SR)
B02 (320-1400 MHz)	−0.47	−0.50
V09 (241-610 MHz)	−0.49	−0.76
G10 (610-1.4 GHz)	−1.2	−1.2
B17 (2-3 GHz)	−1.31	−1.20
P21 (241-1283 MHz)	−0.98	−1.01
Current work (241-1283 MHz)	−0.70	−0.88

and MeerKAT low-resolution images at the bottom of Figure 4.9. Therefore, only two points were used in finding its slope. We see that the resulting slope of $\alpha = -0.33$ is unusually flat. Our spectral index is comparable to the value of $\alpha \sim -0.5$ found in the low-sensitive observations of B02 for the large scale diffuse emission spanning the galaxy distribution at the centre of ZwCl 2341. It is, however, inconsistent with the usual values reported for halos $\alpha \geq 1$ (Feretti et al., 2004; Ferrari et al., 2008; van Weeren et al., 2019). Its unusually flat spectrum combined with its large size $\gtrsim 1$ Mpc could be the properties of a new class of radio source called a radio bridge that connects the two relics (see §1.2.2.3).

Given these spectral index values, we additionally estimated the K-corrected (rest-frame) radio power at 1.4GHz ($P_{1.4\mathrm{GHz}}$) using the MeerKAT 1283 MHz data for the double radio relics and the central diffuse source in ZwCl 2341. We used the following formula:

$$P_{1.4\mathrm{GHz}} = \frac{4\pi D_{\mathrm{L}}^2 S_{1.4}}{(1+z)^{1+\alpha}} \,. \tag{4.1}$$

Where D_{L} is the source luminosity distance at $z = 0.27$, and $S_{1.4}$ is the source flux density extrapolated to 1.4 GHz. For the NR, using an extrapolated flux density of 0.82 mJy at 1.4 GHz and $\alpha = -0.70$, we obtain the power at 1.4 GHz to be $P_{1.4\mathrm{GHz}} = (1.87 \pm 0.37) \times 10^{23}$ W Hz^{-1}. For the SR, using an extrapolated flux density of 6.90 mJy at 1.4 GHz and α = -0.88, we obtain the power at 1.4 GHz to be $P_{1.4\mathrm{GHz}} = (1.63 \pm 0.30) \times 10^{23}$ W Hz^{-1}. We have done the same calculation for the central diffuse source and found $P_{1.4\mathrm{GHz}} = (0.69 \pm 0.05) \times 10^{23}$ W Hz^{-1}. These values are also shown at the bottom of Table 4.6.

In the estimates of the flux density and radio power we, have also shown the corresponding error associated with each value. There are generally three sources for these errors when calculating the flux density, (1) error due to the uncertainty involving unresolved sources used for calibration of the data, (2) error due to the extended nature of diffuse sources and (3) error due to point source subtraction. Since these three source of errors are unrelated, they are added in quadrature to estimate the final error ΔS of the flux densities for extended sources:

$$\Delta S = \sqrt{(\sigma_{\mathrm{amp}} \times S)^2 + \sigma_{\mathrm{ext}}^2 + \sigma_{sub}^2}\ . \tag{4.2}$$

Where S is the flux density, σ_{amp} is the flux calibration uncertainty. We have used a value of 10% for σ_{amp} in both MeerKAT and uGMRT flux density measurements. σ_{ext} is the error due to the extended nature of the source with $\sigma_{\mathrm{ext}} = (\sigma_{\mathrm{rms}} \times \sqrt{\frac{\text{source size}}{\text{beam size}}})$. σ_{sub} is the error associated with point source subtraction with $\sigma_{sub} = \sum_i (\sigma_{\mathrm{rms}} \sqrt{N_{\mathrm{beams,i}}})$. Where the sum is over all point sources i that were subtracted and N_{beams} is the number of beams covering the source.

Table 4.6: Properties of diffuse radio sources in ZwCl 2341.

Relics	Frequency (MHz)	325	675	1283
	Synthesised beam (″ × ″,°)	11 x 8, 79	4 × 3, 52	8 × 6, -3
	$\sigma_{\rm rms}$ (μJy beam^{-1})	31	8	11
	North relic flux (mJy)	18.0± 1.81	12.6 ± 1.20	6.67 ± 0.67
	South relic flux (mJy)	64.0 ± 6.42	28.4 ± 2.86	19.05 ± 1.91
	Northern relic size (″)	110 × 77	100 × 70	109 × 73
	Southern relic size (″)	146 × 180	123 × 156	133 × 170
	Northern relic size (kpc)	468 × 326	426 × 298	464 × 311
	Southern relic size (kpc)	622 × 767	524 × 664	566 × 724
North relic radio power at 1.4 GHz (W Hz^{-1} × 10^{24})		~ 1.87 ± 0.37		
South relic radio power at 1.4 GHz (W Hz^{-1} × 10^{24})		~ 1.63 ± 0.30		
Central diffuse source	Frequency (MHz)	343	675	1283
	Synthesised beam (″ × ″,°)	-	72 × 40, 121	51 × 50, 126
	$\sigma_{\rm rms}$ (μJy beam^{-1})	-	80	77
	Central diffuse source flux (mJy)	-	4.12 ± 0.56	3.31 ± 0.51
	Central diffuse source size (″)	-	222 × 273	220 × 250
	Central diffuse source size (kpc)	-	946 × 1163	937 × 1065
Central diffuse source radio power at 1.4 GHz (W Hz^{-1} × 10^{23})		~ 0.69 ± 0.05		

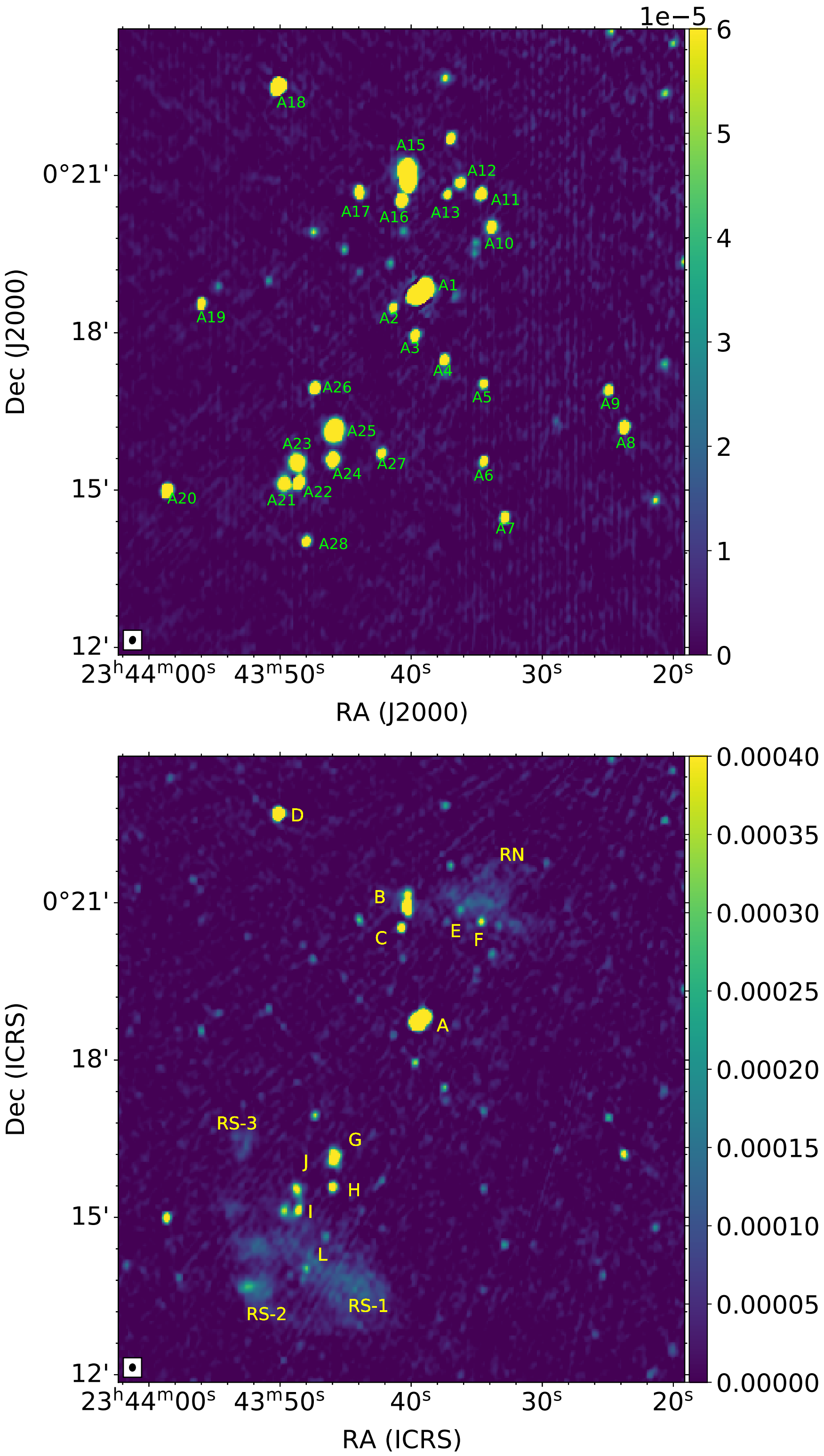

Figure 4.6: ZwCl 2341 point sources selected for subtraction. *Top*: MeerKAT DI image of ZwCl 2341 (`robust=0`) showing the same sources and labels of V09. *Bottom*: Point source model image that shows no extended sources only point sources. We have marked the sources we have subtracted from the visibility which include the ones from the top image of V09.

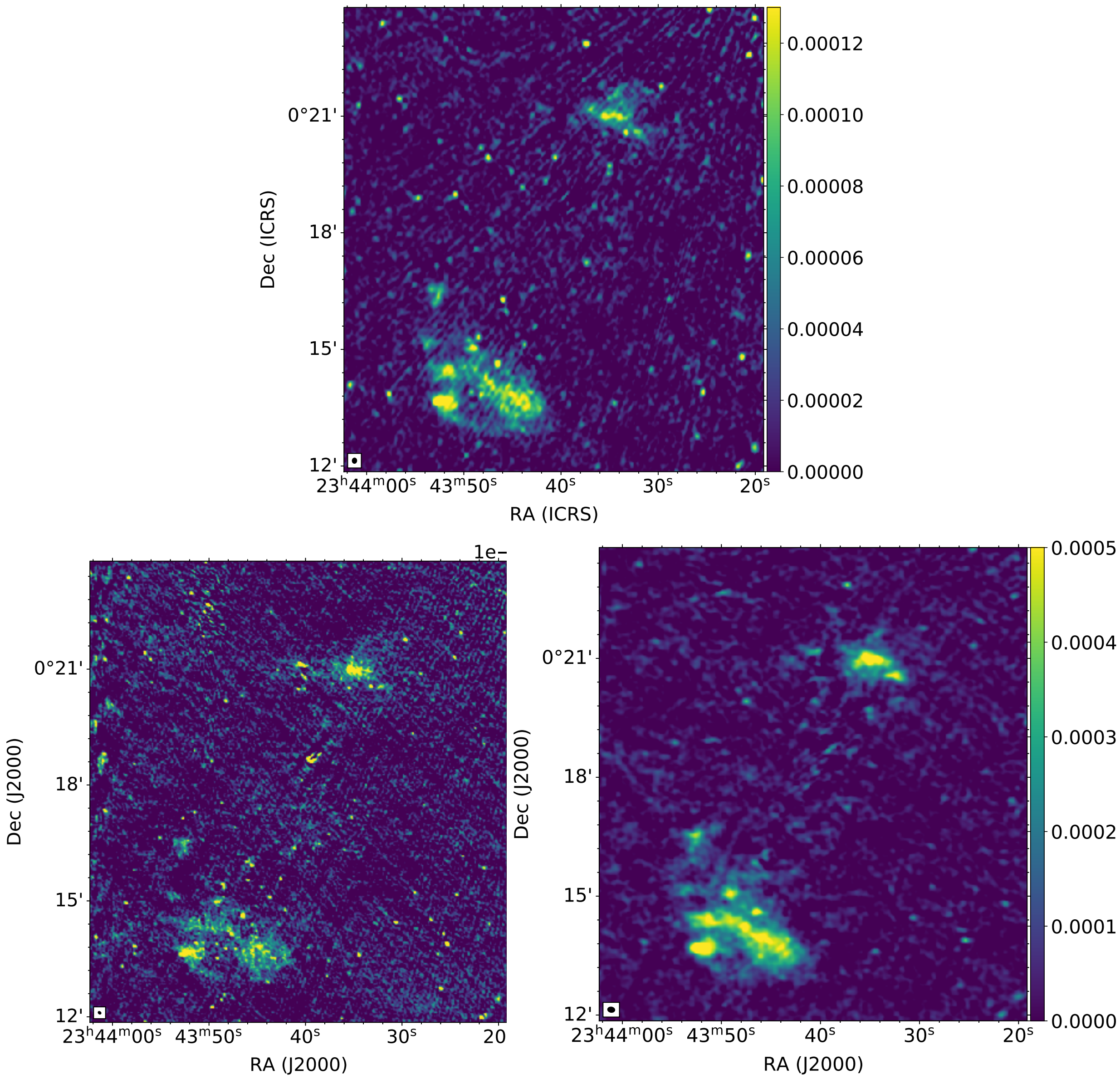

Figure 4.7: Source subtracted images of our new MeerKAT and uGMRT observation with archival legacy GMRT data. The beam sizes are shown at the bottom left of each image in black on a white square. *Top*: MeerKAT 1283 MHz DD image with beam size of $8'' \times 6''$ and $\sim \sigma_{\rm rms} = 11$ μJy beam^{-1}. *Bottom left*: uGMRT 675 MHz DI image with beam size of $4'' \times 3''$ and $\sim \sigma_{\rm rms} = 8$ μJy beam^{-1}. *Bottom right*: GMRT 325 MHz DI image with beam size of $10'' \times 7''$ and $\sim \sigma_{\rm rms} = 31$ μJy beam^{-1}.

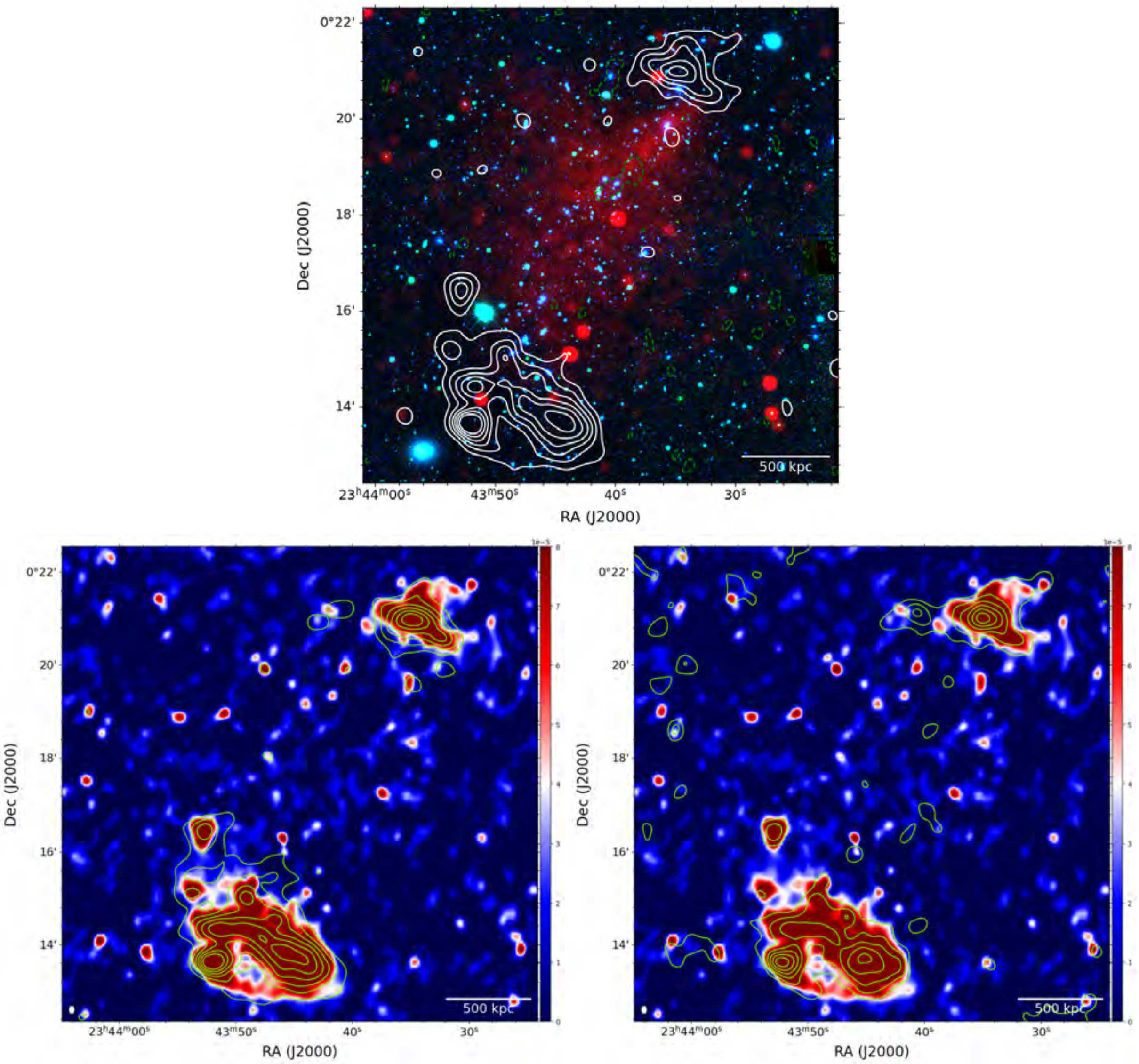

Figure 4.8: Different interpretations of the double relics in ZwCl 2341 using the MeerKAT 1283 MHz, uGMRT 675 MHz and archive legacy GMRT 325 MHz data. All images have been convolved to the largest beam size of $11'' \times 8''$ (of the GMRT 325 MHz image) shown at bottom left in white. The contour levels for all images are spaced as: $[1, 2, 3, 4, 5, 6, 10, 20] \times 3\sigma_{\rm rms}$. *Top*: Point source subtracted, DD calibrated MeerKAT 1283 MHz (with $\sigma_{\rm rms} = 9\ \mu$Jy beam^{-1}) radio contour overlayed on a multi-frequency RGB image. The radio emission is shown in white contours, Chandra smoothed X-ray is shown in red and the DECaLS optical components are shown using a combination of green and blue. *Bottom left*: Colour image of the MeerKAT 1283 MHz radio emission with GMRT 325 MHz green contours overlayed on it. The $\sigma_{\rm rms}$ of the uGMRT observation is $\sim 13\ \mu$Jy beam^{-1}. *Bottom right*: Colour image of the MeerKAT 1283 MHz radio emission with uGMRT 675 MHz green contours overlayed on it. The $\sigma_{\rm rms}$ of the GMRT observation is $\sim 23\ \mu$Jy beam^{-1}.

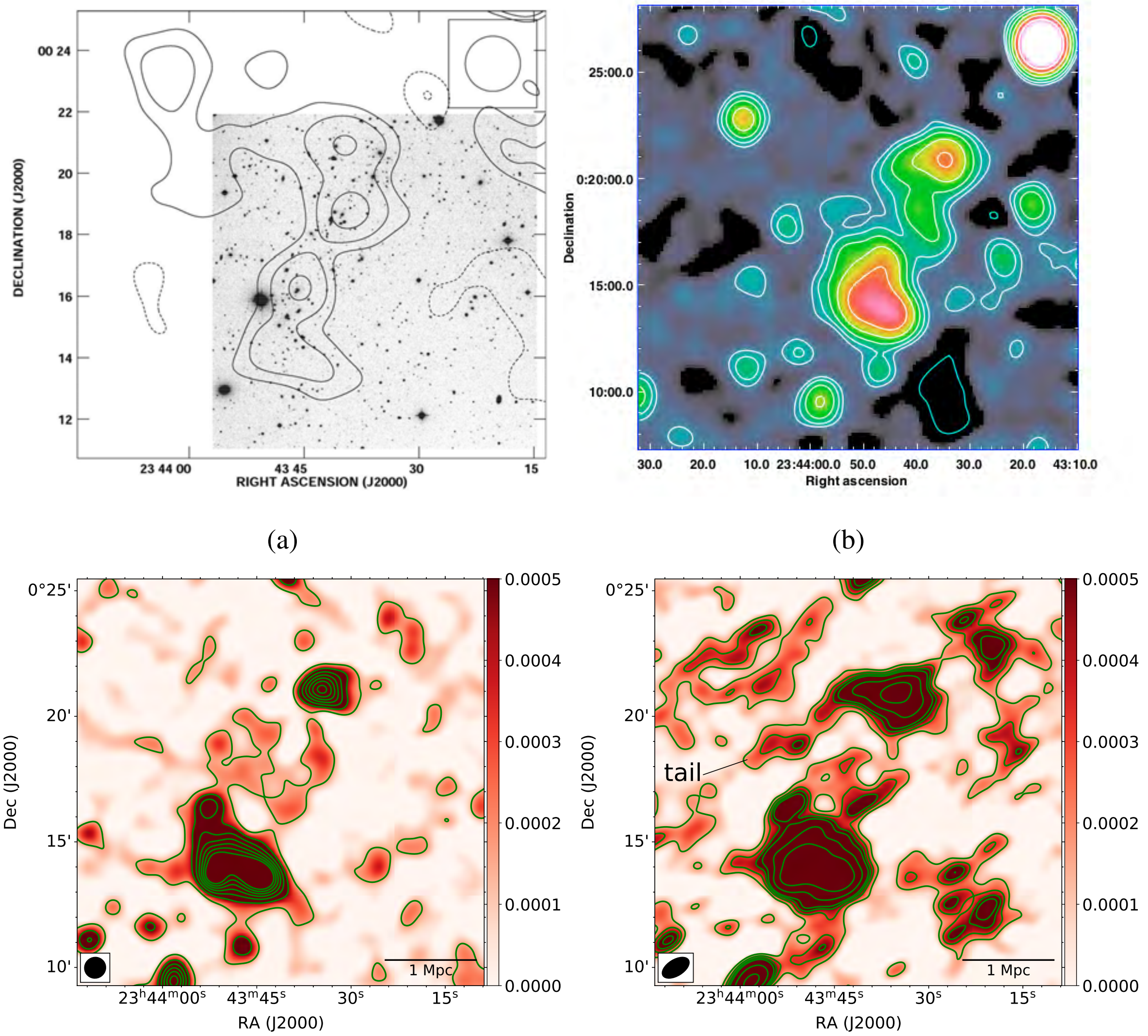

(a) (b)

(c) (d)

Figure 4.9: Observational history of low-resolution images of ZwCl 2341 combined with our new low-resolution images demonstrating the potential existence of diffuse faint emission spanning the large scale filamentary region between the relics. *(a)*: Low sensitive VLA 325 MHz radio data showing the first of such large-scale emission. The beam size is 108″ × 108″ and radio contour levels are spaced as: $[-4, -2, -1, 1, 2, 4, 8, 16] \times \sigma_{\rm rms}/1.6$, where $\sigma_{\rm rms} = 2.5$ mJy (B02). *(b)*: Follow up VLA 1.4 GHz observations that were the first to demonstrate the hint of diffuse emission connecting the two relics. In this observation, the beam was tapered to 83″ × 75″. Contour levels are spaced as: $[1, 2, 4, 8, 16] \times 3\sigma_{\rm rms}$, where $\sigma_{\rm rms} = 150$ μJy beam $^{-1}$ (G10). *(c)*: Point source subtracted 50″ tapered DD MeerKAT image with $\sigma_{\rm rms} = 77$ μJy beam^{-1}. The contour levels are spaced as: $[1, 3, 5, 7, 9, 11] \times 2\sigma_{\rm rms}$. *(d)*: Point source subtracted 50″ tapered DI uGMRT image with $\sigma_{\rm rms} = 80$ μJy beam^{-1}. Contour levels are spaced the same as the previous MeerKAT image.

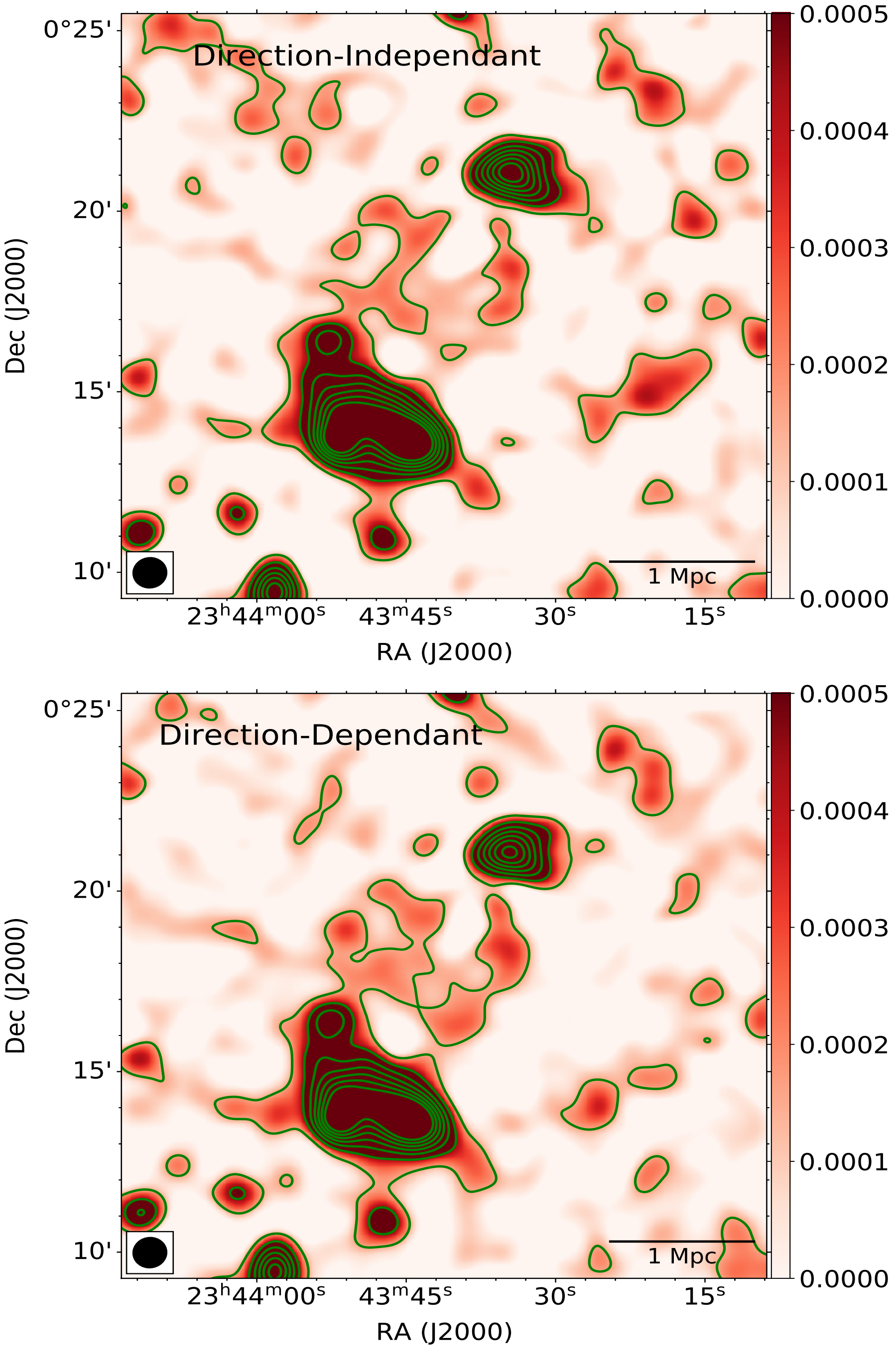

Figure 4.10: Large scale diffuse and faint emission detection between relics before and after DD calibration. *Top*: MeerKAT DI image of ZwCl 2341 tapered with 50″ beam size with $1\sigma_{\rm rms}$ = 86 μJy beam^{-1}. *Bottom*: The DD corrected image of the above image and $1\sigma_{\rm rms}$ = 77 μJy beam^{-1}.

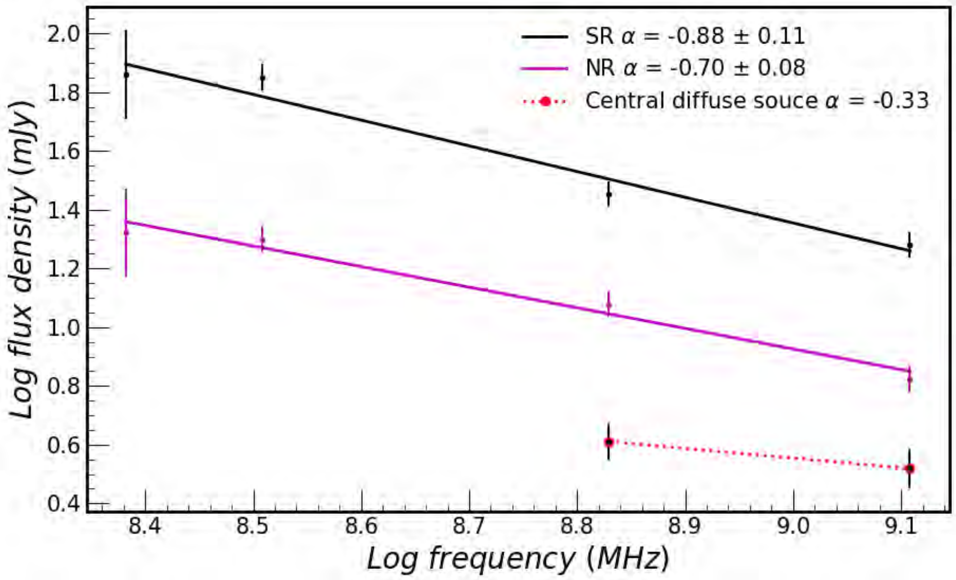

Figure 4.11: 1-D Spectral index plot for NR, SR and central diffuse source between the frequency range 241-1283 MHz. We used the V09 flux densities corresponding to the lower-frequency (241 MHz) point and the GMRT, uGMRT and MeerKAT images for the higher-frequency (325, 675 and 1283 MHz) points. The 241 MHz data has poor SNR and hence a large error bar associared with the flux density.

Chapter 5

Discussion

In this chapter, we will discuss our image improvements after applying DD calibration and the methods used to quantify them. We will also investigate the various trends observed in our chosen statistical parameters to gain a better understanding of these improvements. We then discuss our scientific results of double radio relic - its spectral index plot and diffuse central radio source located between the relics. We discuss the true nature of this source as either a radio halo or bridge and use the radio power vs mass relation to see how the relics and diffuse central source compare with other double relics and halos in literature. Lastly, we discuss interesting radio galaxies residing in ZwCl 2341.

5.1 Direction dependent effects

We have applied two different DD calibration software (`CubiCal` and `killMS`) on L-band MeerKAT data in order to improve the image quality and quantify it statistically. We have applied the software to the two galaxy clusters ZwCl 2341 and A2631 residing in the core part of the *Saraswati* supercluster and used the 11 statistical parameters of §4.1.2 to quantify the improvements.

5.1.1 Statistical trends

We have outlined the statistical parameter calculation procedures in §4.1.2 performed on the bright sources marked in the top left images of Figures 4.1 and 4.2 for the clusters ZwCl 2341 and A2631, respectively. The $8' \times 8'$ box images of these selected sources are shown in Figures 4.3 and 4.4. The statistical calculations were performed using both residual (which has background noise) and restored maps (noise plus deconvolved data) generated by `DDFacet`.

An important note to consider is that these DD improvements were not used to compare the two DD software (`CubiCal` and `killMS`), as both have different calibration techniques and algorithms. `CubiCal` calibrates using source-specific peeling while `killMS` uses a facet-based approach for the entire image. The software also perform differently and depend on their unique input parameter selections (see §2.4.3 and §2.4.4 for these parameters of `killMS` and `CubiCal`, respectively), underlying data qualities (depending on the level of background noise present in the data, both techniques apply calibration differently) and the purpose of the science case. Statistical and quantitative analysis of radio images is useful when studying image fidelity and DR. These two terms were discussed at length in §2.6.2; image fidelity is a measure of the correctness of an image and the DR is used to quantify this correctness.

Our 11 chosen statistical parameters are shown in Tables 4.2 and 4.3; these tables show decreasing trends of SUM NEG, MIN, RMS and MAD. The RMS and MAD measure the deviation from the mean value (they are both dispersion measures, see Table 2.2 of §2.6.3), and so in essence measure the same quantity. The definition of DR is given in Equation 2.22 of §2.6.2. These definitions show an inverse dependence on RMS (both locally and globally) and MIN values. The decreasing RMS and MIN value after DD calibration, therefore, translates to DR values (DR1, DR2 and DR3) that are higher in DD images as compared to DI, which implies clear improvements around the strong sources causing artefacts. For DR1 and DR2, due to the inverse dependence on the local RMS and MIN, we see these two values are better for `CubiCal`-generated DD images as compared to the `killMS`, while DR3 is better for `killMS` due to the inverse dependence on the global RMS and MIN. Furthermore, for the full images, the DR2 and DR3 are better for `killMS`. This is because the peeling method offered by `CubiCal` performs DD calibration for individual strong sources while the faceting on the entire FoV approach offered by `killMS` applies DD calibration in directions defined by the tessels spanning the entire FoV, thereby correcting the entire image. These results suggests, that the DD image improvement offered by `CubiCal` corresponds to an improvement in local region statistics measuring DD improvement, while `killMS` is better at improving these statistics for the global region.

5.1.2 Flux density comparison between calibrations

The flux density plots shown in §4.1.3 generally follow the linear correlation indicated by the solid black line. Visually, the DI vs DD `CubiCal` plot has an overall better fit than the DI vs DD `killMS` plot, as well as less scatter. The R^2 and m values for these plots also strongly agree with this visual observation. The DI vs DD `CubiCal` plot, showing almost perfect correlation, has its corresponding R^2 and m close to 1. The `killMS` plot shows some scatter particularly at the lower flux density region (faint sources). We calculated the statistical parameters FI and CV to quantify the scatter seen in the `killMS` plot. The FI of the flux density for `killMS` is about four times greater than for `CubiCal`: $FI_{\text{killMS}} \approx 4FI_{\text{CubiCal}}$. $\text{CV}_{\text{killMS}}$ is about $\approx 9\%$ larger than $\text{CV}_{\text{CubiCal}}$. These all support the scatter seen in `killMS`. Below we explain why this scatter is so prominent in our `killMS` image.

It is known that the flux density of sources are expected to change after applying DD calibration. When DD or DI solutions are computed in general, the errors in the data (real data subtracted from skymodel, see Equation 2.11 in §2.3.2) result from either a) low level RFI, b) low SNR (if solution intervals are not long enough) or c) unmodeled sources. These errors are absorbed into the solutions (gains). The resulting gains are not smooth but noisy. Calibration algorithms will always try to move these gains somewhere around the field. This effectively amplifies or suppresses the flux of certain sources.

Point sources are well-modelled sources and diffuse emission, due to their extended and complex nature, are difficult to model for calibration algorithms, and are therefore often unmodeled. The calibration algorithms generally therefore, during solving, transfer the missing flux from unmodeled sources to the well-modelled sources like point sources, thereby increasing their flux density. This is more significant in DD calibration as compared to DI calibration because we generally have good SNR for DI calibration because we use the entire sky as a model to perform the calibration. DD calibration is generally performed in directions defined by a few bright sources (or tessels for `killMS`) and as a result, to get sufficient SNR, the fluxes from these sources are emphasised in the solving.

We have mentioned the facet-based calibration scheme implemented by `killMS`, in which calibration is performed ‘globally’ in directions from the entire FoV. This is in contrast with `CubiCal`, which applies ‘local’ calibration through peeling of a select number of bright sources. This ‘global’ calibration could be the cause of the scatter in the DI vs DD plot for `killMS`. The `killMS` ‘global’ based calibration strategy picks up more unmodelled flux as the tessels are larger than the regions marked around the bright sources used for the peeling of `CubiCal`. This unmodelled emission forms part of the gain solutions which are transferred to the modelled point sources, increasing their flux density more as compared to `CubiCal`.

5.2 Diffuse radio sources in ZwCl 2341.1+0000

We discuss the resulting spectra for the double relics obtained using our new MeerKAT and uGMRT data and derive the $\mathcal{M}$ to see how they compare with previous observations. We then try deduce the true nature of the diffuse source between the double relics by using optical analyses from previous work to discuss the central halo/bridge between the double radio relic postulated to exist in ZwCl 2341. We then shift our attention to an interesting radio galaxy residing in ZwCl 2341 found to be well resolved in our new data as compared to previous data, and in close proximity to the SR.

5.2.1 Spectral analysis and Mach number

The presence of double relics in a galaxy cluster system is a particularly intriguing find, since the shape, morphology and properties of these extended structures strongly suggests a model of outward travelling shock waves originating from the cluster centre, travelling in opposite directions to the peripheral regions (Ensslin et al., 1997; Markevitch et al., 2002). Due to the short radiative lifetimes of the emitting relativistic electrons, radio emission is produced in a location close to the shock waves. The current widely accepted DSA model for the shock formation of relics (Ensslin et al., 1997; Kang & Ryu, 2015) tells us that the magnetic fields are aligned parallel with the shock front and the radio spectrum is flatter at the shock edge where the particles are re-accelerated.

We can use the radio spectral index as a tool to understand the underlying electron energy distribution and the properties of the surrounding magnetic fields in which they are located. Diffuse sources are typically classified into steep ($2 \geq |\alpha| > 0$) and flat ($1 \geq |\alpha| > 0$) spectrum sources (e.g. Ferrari et al. 2008; Feretti et al. 2012; van Weeren et al. 2019).

We have shown our 1-D spectral index map of the diffuse sources in ZwCl 2341 in Figure 4.11 of §4.2.3. We have utilised our new MeerKAT, uGMRT data and archival legacy GMRT data in plotting the flux density for the 1283 MHz, 675 MHz and 325 MHz components, respectively. We used the GMRT flux density listed in V09 for the 241 MHz component. The most recent analysis by P21 has also shown a spectral index plot but have included their own MeerKAT 1283 MHz and GMRT 323 MHz point in combination with the 241 MHz and 610 MHz GMRT points from V09.

The results presented in this work show that both relics exhibit flat spectra, with the SR slightly steeper ($\alpha_{SR} = -0.88$) than the NR ($\alpha_{NR} = -0.70$). Flat spectrum sources are constantly compensated with energy from ongoing shock or generated turbulence while they suffer from synchrotron losses visible as radio emission. The flatter NR source shows lower synchrotron losses and a less dynamically active region as compared to the slightly steeper SR. According to the DSA, the region of a flatter spectrum signifies the location of the shock front, where the particles are initially accelerated. Our results show no evidence of a spectral break in the NR that was reported in P21.

We have used these spectral index values to find the radio Mach number $\mathcal{M}$ for the NR and SR using Equation 1.2 of §1.1.4 to deduce more about the underlying physics. The $\mathcal{M}$ quantifies the strength of a shock. For the NR, using $\alpha_{NR} = -0.70$, we obtain $\mathcal{M}_{NR} \sim 3.31$. For the south relic of $\alpha_{SR} = -0.88$, we obtain $\mathcal{M}_{SR} \sim 2.50$. Our $\mathcal{M}$ lies in the moderate $\mathcal{M}$ number range of $\mathcal{M}$ numbers $2 \leq \mathcal{M} \leq 4$ (Bykov et al., 2008). Given the degree of variation of the spectral index values reported in Table 4.5 from previous observations, it is difficult to comment on the correctness of the $\mathcal{M}$ found in our analysis. The passage of these outward travelling shocks through the cluster central region between the relics could be responsible for the faint $2\sigma_{\rm rms}$ potential halo or bridge that was detected in the new MeerKAT and uGMRT images.

5.2.2 Radio halo or bridge?

The most interesting feature of the ZwCl 2341 system is the potential presence of a diffuse halo (or bridge) situated between the two peripheral relics. The presence of a halo between two relics is a rare occurrence and has been detected in a few clusters (Venturi et al., 2007; Giovannini et al., 2009; de Gasperin et al., 2021). The large size of $\gtrsim$ 1 Mpc for the potential radio halo is comparable to that of clusters like A2163 (Feretti et al., 2001; Thölken et al., 2018), CIZAJ2242.8+5301 (Van Weeren et al., 2010), RXC J1514.9-1523 (Giacintucci et al., 2011) and MACSJ0717.5+3745 (Bonafede et al., 2009b; Van Weeren et al., 2009a). A radio bridge source connecting peripheral relics at the cluster centre is also rare with only few detected (Carretti et al., 2013; De Gasperin et al., 2014; Lindner et al., 2014; de Gasperin et al., 2021). One possible explanation for a radio ridge between two relics is that it could be a diffuse halo situated between the double relics and due to sensitivity constraints, appear as a bridge.

This candidate radio halo/bridge in ZwCl 2341 was first suspected in NVSS of B02 and was not detected in the later low frequency high-resolution GMRT observation of V09. The follow-up VLA L-band observation of ZwCl 2341 by G10 found tentative diffuse emission in their low-resolution images connecting the relics but was not sensitive enough to separate this emission from the NR and SR (see Figure 4.8 of §4.2.3). Our new MeerKAT and uGMRT data provide the highest resolution and sensitivity compared to previous observations. We could not detect the candidate radio halo in our high-resolution ($8'' \times 6''$) MeerKAT and ($4'' \times 3''$) uGMRT images. However, we do see a tentative detection albeit at a $2\sigma_{\rm rms}$ level after tapering these images to a $50''$ beam size resulting in beam sizes of $51'' \times 46''$ and $72'' \times 39''$ for the MeerKAT and uGMRT images, respectively (see Figure 4.9 of §4.2.3). They show a large-scale $\gtrsim$ 1 Mpc diffuse and extended radio source permeating the central region between the two relics. In our MeerKAT DD image of Figure 4.9 (c), the double relic emission is almost separated from the emission at the centre. For the uGMRT image of Figure 4.9 (d), we could not clearly separate out the relics from the central diffuse source, instead, the central source shows two structures: 1) central diffuse structure connected to the SR, 2) an extended tail like diffuse structure connecting the NR separated from the central diffuse structure extending towards the SR. This uGMRT image is the

DI uncalibrated image from SPAM; we are currently working on the DD improvements of this uGMRT data to see whether we can recover more flux and possibly connect this tail component to the central region and separate the central emission from the relics, similar to what was done in the MeerKAT DD image of Figure 4.10.

Optical and X-ray observations of galaxy clusters have shown the presence of multiple substructures to be indicative of the active dynamical processes existing within the cluster. Figure 3.5 of §3.2.2 from Zhang et al. (2021) shows the multiple X-ray substructures in ZwCl 2341 resulting from the merging of several subclusters or groups. Cluster mergers are also known to leave evidence in the form of increased optical substructure among the member galaxies of the cluster (Girardi & Biviano, 2002).

Spectroscopic data of (Boschin et al., 2013, hereafter B13) and B17 support the existence of multiple substructures coinciding with the diffuse diffuse sources in ZwCl 2341 along the merging axis. Optical analysis by B13 involving a sample of 128 galaxies from Telescopio Nazionale Galileo (TNG) spectroscopic observations and data from SDSS have shown evidence of three to six dynamical substructures spanning the filament making up ZwCl 2341. For the three subcluster model, the north, south and central components coincide with the positions of the NR, SR and potential halo/ridge respectively. The left of Figure 5.1 shows the four substructures resulting from the smoothed number density maps for the spectroscopically confirmed cluster members. B13 used only red-sequence cluster members ($r' \leq 21$).

Later, optical analysis by B17 for a sample of 227 galaxies from Sabaru, DEIMOS (DEep Imaging Multi-Object Spectrograph) and SDSS (71 galaxies of this sample overlapping with the ones from B13) used the Gaussian Mixture Models (GMM) method to statistically group galaxies into substructures. They found that the three model substructure system can most economically describe the distribution of spectroscopically confirmed cluster galaxies. The right of Figure 5.1 shows this three substructure model for the smoothed number density map of red-sequence cluster members of $18 \leq r' \leq 21$.

Galaxy substructures coinciding with double relics have been reported in Abell 3667 (Roettiger et al., 1999a). These substructures combined with the disturbed X-ray morphological substructures presented in Ogrean et al. (2014) and Zhang et al. (2021) could be fuelling the diffuse radio sources in ZwCl 2341 as a result of turbulence (for the central halo/bridge) and shock waves (for the peripheral relics). If ZwCl 2341 hosts a central halo, then its global ICM temperature of $\mathrm{kT}_X \sim 4-5$ keV (Ogrean et al., 2014) is much lower than what is expected for the X-ray temperatures attributed to clusters hosting halos ($\sim 7-10$ keV). G10 also found polarization in the central region ($\sim 11\%$) which is uncharacteristic of halo sources since they are generally unpolarised.

The surface brightness of the suspected halo or bridge was calculated for the MeerKAT and uGMRT images by finding the ratio of the flux density to area of area enclosed by a rectangle region around the central region hosting the faint emission. For the MeerKAT and uGMRT images, we found a surface brightness of $\sim 5.4\times10^{-5}$ mJy arcsec^{-1} and $\sim 6.8\times10^{-5}$ mJy arcsec^{-2}, respectively. These measurements are both comparable to the value of $\sim 7.0\times10^{-5}$ mJy arcsec^{-2} reported by G10 in their low-resolution image for the diffuse emission spanning the central component between the relics. V09 did not detect any halo emission and instead quoted an upper limit of 1.5 μJy arcsec^{-2} to the surface brightness which is well above the values of G10 and the ones found in our new MeerKAT and uGMRT data; hence, why it was not detected in their data.

The definitions for radio bridge, halos and ridge are not concrete and contain many similarities. Classifying these sources is mostly a matter of interpretation of the data. Higher resolution and sensitive observations are therefore required to give firm conclusions on the true nature of this source since currently, from our analysis, the nature is still undetermined.

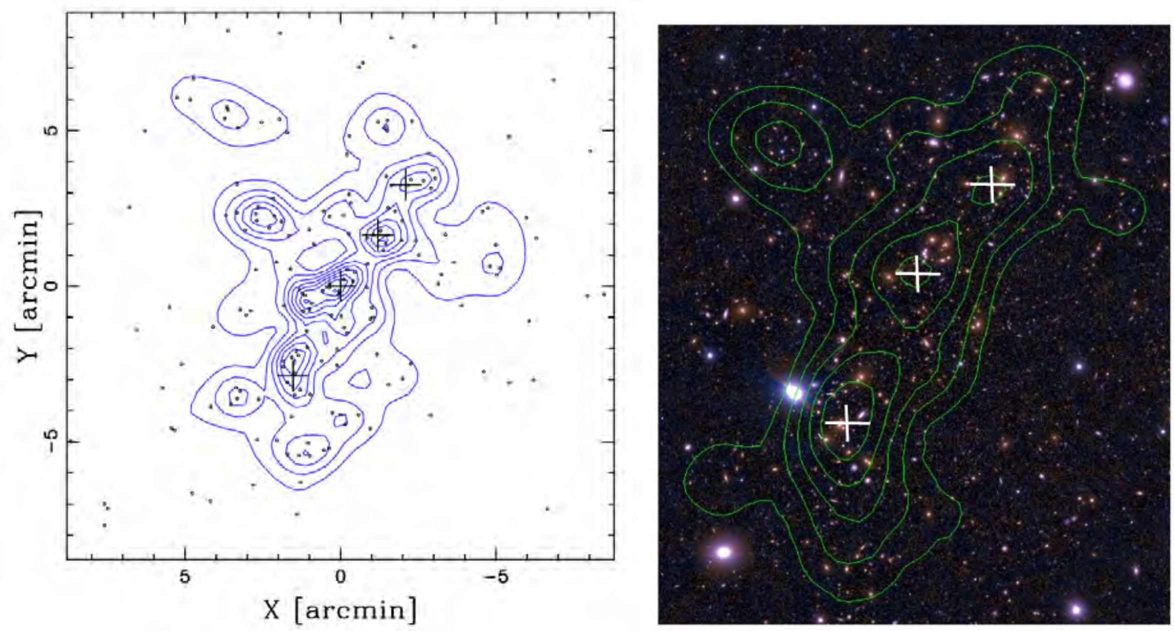

Figure 5.1: Isodensity contour maps for spectroscopic confirmed cluster members of ZwCl 2341 showing the existence of a few substructures. *Left*: Smoothed number density map of the photometric cluster members in a $18' \times 18'$ region centered on ZwCl 2341 showing four optical substructures indicated by black crosses at their centre. Photometric cluster members are red-sequenced cluster members with magnitude criteria, $r' \leq 21$ are shown in black dots and their relative isodensity is shown in blue contours (smoothed) (B13). *Right*: Subaru image of ZwCl 2341 with overlayed smoothed number density of red-sequenced selected galaxies of magnitude $18 \leq r' \leq 21$. The isodensity contours are shown in green and the white crosses indicated the three optical substructures (B17).

5.2.3 Radio power and mass relationship

We show the radio power at 1.4 GHz, $P_{1.4\mathrm{GHz}}$ vs cluster mass $\mathrm{M}_{\odot}$ and LLS plots in Figure 5.2 for the double relics and potential halo/bridge of ZwCl 2341. These plots allow us to understand how our diffuse sources compare with others in the literature. The top left, top right and bottom left and bottom right are directly from Kale et al. (2017), Feretti et al. (2012), Johnston-Hollitt & Pratley (2017) and Giovannini et al. (2009), respectively. The radio relic plots are shown at the top and potential halo/bridge plots are at the bottom of Figure 5.2. We have plotted each relic separately labeled 'ZwCl 2341 NR' and 'ZwCl 2341 SR' for the north and south relic, respectively. We have labelled the potential halo/bridge as 'ZwCl 2341 Halo'. The meaning of the symbols in each plot are described in the caption of Figure 5.2. The top left plot of Figure 5.2 shows that the ZwCl 2341 double relics are situated close to the best-fit $P_{1.4}$ vs $\mathrm{M}_{\odot}$ correlation line. The NR is located slightly below the fitted line and the SR is situated close to the line. Our radio relics are located around other double radio relic clusters. From the $P_{1.4GHz}$ vs LSS plot at the top right of Figure 5.2 we see that with regards to size, our cluster deviates from the $P_{1.4GHz}$ vs LLS correlation of other clusters. For our potential radio halo shown in the bottom panels of Figure 5.2, we see that generally, our halo/bridge follows the correlation.

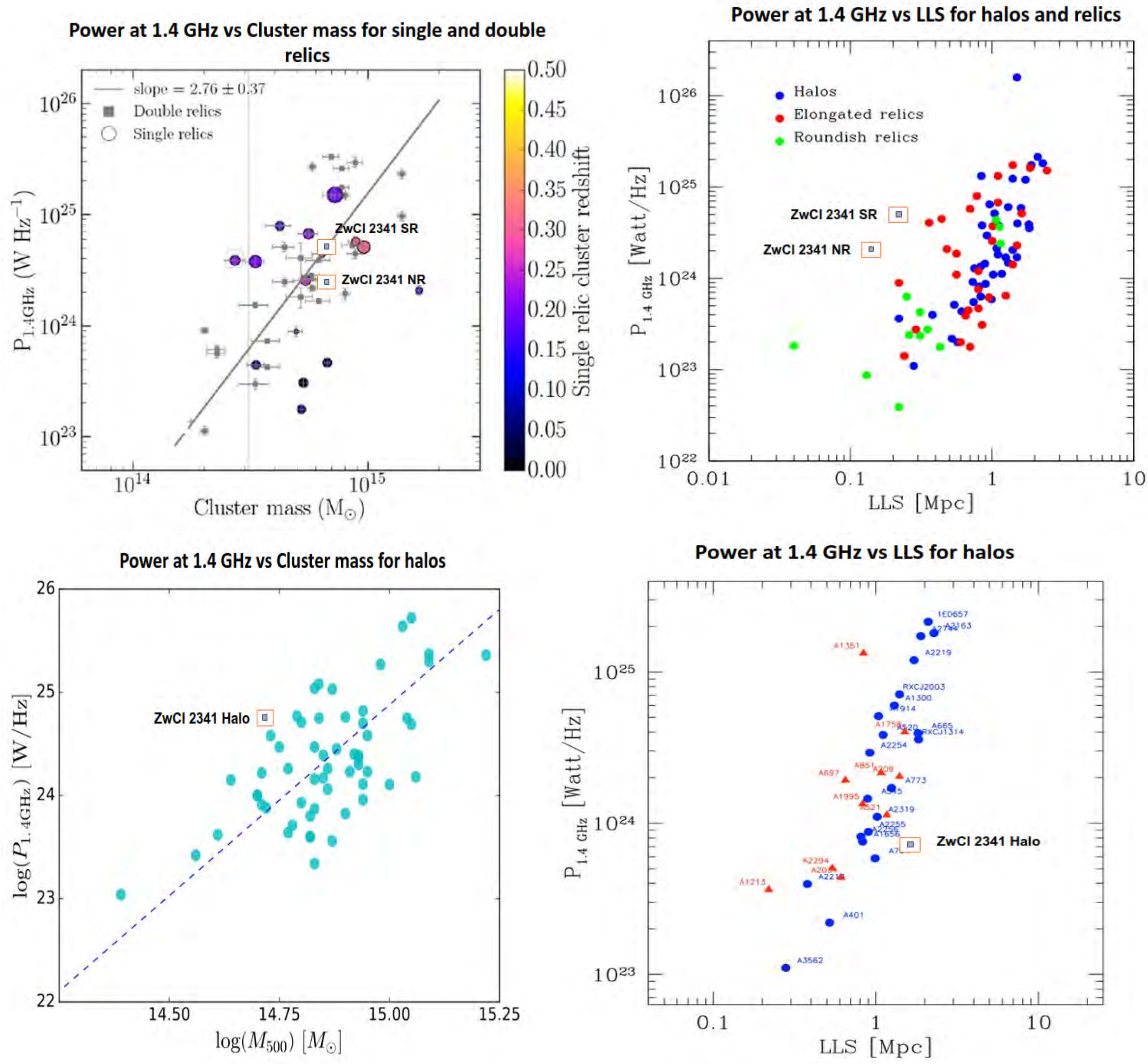

Figure 5.2: The location of ZwCl 2341 diffuse sources on the various scaling relation plots. Its position is marked with a square enclosed by a larger red-outlined square. *Top left*: $P_{1.4\mathrm{GHz}}$ vs $\mathrm{M}_\odot$ for various single relics shown as circles (scaled according to relic size and coloured according to the redshift shown in the color bar) and double relics shown as grey squares for the sample of relics from Kale et al. (2017). *Top right*: $P_{1.4\mathrm{GHz}}$ vs LLS for halos and single relics of different morphologies taken from the Feretti et al. (2012) sample. Halos, elongated relics and roundish relics are shown in green, red and blue, respectively. *Bottom left*: $P_{1.4\mathrm{GHz}}$ vs $\mathrm{M}_\odot$ for a sample of 57 halos from literature (aqua dots) (Johnston-Hollitt & Pratley, 2017). Dashed line is the correlation fit for a 25 sample of halos from Cassano et al. (2013). *Bottom right*: $P_{1.4\mathrm{GHz}}$ vs $\mathrm{M}_\odot$ for a sample of halos from literature (blue dots) and new VLA 1.4 GHz data (red dots) from Giovannini et al. (2009).

5.3 Interesting radio galaxies in ZwCl 2341

A couple of interesting radio galaxies reside in ZwCl 2341. The brightest radio source (labelled A1 in the bottom of Figure 4.6) at the central region of ZwCl 2341, is a 'tailed' radio galaxy that was already investigated by V09, G10 and B17. We have listed its radio properties in Table 4.4.

In our further investigation, we found a radio galaxy situated close ($\sim 10''$) to the SR. Our new high-resolution MeerKAT and uGMRT data were able to resolve this radio galaxy's structure into three separate components; two radio lobes and a compact core. These three components are labelled A21, A23 and A22 in the bottom of Figure 4.6, respectively. We used the NED* and SIMBAD† astronomical data acquisition services to find this source and its properties. The position of the core of this radio galaxy is J2000, RA: $23^{\mathrm{h}}43^{\mathrm{m}}48.53^{\mathrm{s}}$, DEC: $+00^{\circ}15'07.52''$. In the NVSS catalogue, this radio galaxy is listed as NVSS J234347.53+001524.0 (NVSS J2343 hereafter). The optical counterpart of NVSS J2343 is SDSS J234348.53+001507.5 with a spectroscopic redshift of $z = 0.27$, suggesting a member galaxy of ZwCl 2341.

The different components of NVSS J2343 were not resolved out in the previous low-resolution observations. We show NVSS J2343 in the inset of Figure 5.3. The lobes are diffuse in nature and nearly symmetrical extending in an arc-like/boomerang shape to the north-east side of the compact AGN at its centre. The upper-lobe (northern-extension) extends to about $\sim 33''$ while the lower lobe (eastern-extension) extends to $\sim 23''$ from compact core. Its compact core has a flux density of ~ 0.93 mJy ($P_{1.4\mathrm{GHz}} \sim 1.79 \times 10^{24}$ WHz $^{-1}$) and a total flux density including the lobes of ~ 2.97 mJy ($P_{1.4\mathrm{GHz}} \sim 5.39 \times 10^{24}$ WHz $^{-1}$). It is difficult to identify the morphology of this radio galaxy, the present data suggest that its morphology could be matched with the criteria of an FR II radio galaxy (Fanaroff & Riley, 1974). FR II Radio galaxies are lobe-dominated sources whose lobes extend further from the nucleus than with FRI. Their termination region produces hotspots of diffuse emission (Mo et al., 2010). The bottom left of Figure 5.3 shows a $1' \times 1'$ zoomed-in region centred on this source. NVSS J2343 could also be a bent-tail radio galaxy and we show an example of this type of galaxy (NGC 1265) at the bottom right of Figure

---

*https://ned.ipac.caltech.edu/

†http://simbad.cds.unistra.fr/simbad/

5.3. It is believed that as NGC 1265 travels through the ICM, intergalactic wind hits the radio galaxy causing the twin beams of plasma ejected from the AGN (jets) to bend into a ‘U’ shape as a result of the ram pressure bending (RPB) (Begelman & Rees, 1996).

In our case, the close proximity of NVSS J2343 to the SR of ZwCl 2341 is particularly interesting as these types of sources are suspected to be of vital importance in current theoretical models of relic formation (Kang & Ryu, 2011; Brunetti & Jones, 2014; Van Weeren et al., 2017). These models predict that the relics produced from low $\mathcal{M}$ shock-induced mergers do not contain enough energy to re-accelerate the low energy electrons residing in the thermal pool of the ICM to relativistic energies responsible for the radio luminosities observed in relics. It is therefore suspected that since AGN are natural seeds of relativistic electrons, they can provide the necessary supply of mildly relativistic electrons to the cluster outskirts well before the shock passage. Since this plasma is now much more energetic than the thermal gas of the ICM, it requires lower acceleration efficiency and the cluster shocks can easily re-accelerate these fossil electrons to power the relic to the currently observed luminosities. A similar scenario can be seen in the MeerKAT observation of the merging cluster A2384 (Parekh et al., 2020). In this system, the lobe of an FRI radio galaxy (LEDA 851827) is seen interacting with the SR in a similar fashion to NVSS J2343 interaction with the SR of ZwCl 2341.

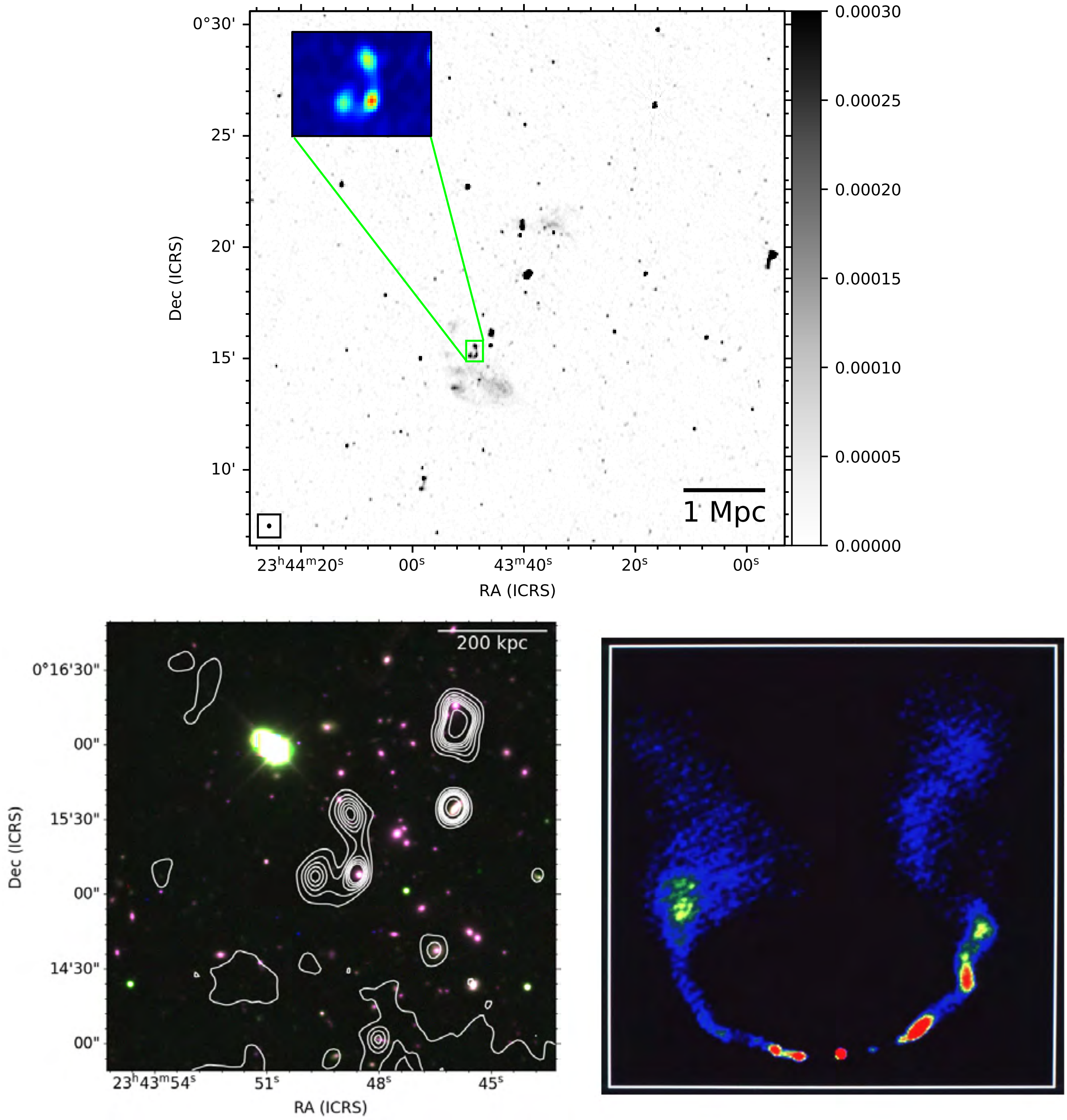

Figure 5.3: Radio galaxy NVSS J2343 found in ZwCl 2341 in close proximity to SR. *Top*: MeerKAT DD grey-scale colour radio image of ZwCl 2341. NVSS J2343 is situated about 10″ on the north side of the SR in ZwCl 2341. A zoomed-in region of this radio galaxy is shown inset at the top left. *Bottom left*: Zoomed-in MeerKAT image radio contour of NVSS J2343 superimposed over the RGB optical colour image. The optical subbands are taken from DECaLS DR9. The radio contour levels are spaced as: $[1, 2, 3, 4, 5, 6, 10, 20] \times 5\sigma_{\rm rms}$, where $\sigma_{\rm rms} = 10$ μJy beam $^{-1}$. *Bottom right*: Example of the NGC 1265 radio galaxy, which is classified as a typical narrow-angle bent-tail radio galaxy which could also be the classification of NVSS J2343. This galaxy moves through the ICM of the Perseus Cluster at a velocity of about 2000 km/s. Its interaction with the galactic wind causes the jets to bend into a ‘U’ shape (Begelman & Rees, 1996).

Chapter 6

Conclusion

In this work, we have shown the importance of the sensitivity, resolution and wide-field nature offered by the SKA precursor, MeerKAT in the imaging of complex diffuse radio emission in massive galaxy clusters such as ZwCl 2341. In our radio analysis of ZwCl 2341, including our new MeerKAT and uGMRT data combined with previous analysis from literature, shows that ZwCl 2341 is a complex merging galaxy cluster system hosting diffuse, faint ~ Mpc scale emission in the form of a double radio relic and a potential halo or bridge source between the relics. Previous optical analyses showed a striking affiliation of the optical filament of galaxies and unique substructures with the diffuse emission. X-ray analyses showed several unique morphological features and substructures all indicative of a complex dynamical system. ZwCl 2341 large mass and complex nature tells us that this region is experiencing LSS formation either from multiple mergers between several galaxy groups or as a node in the cosmic web from in-falling filaments.

We found that our new MeerKAT observation at L-band had the highest sensitivity as compared to previous L-band observations with VLA when imaging the diffuse sources present. Our new MeerKAT observation could almost separate all three diffuse radio sources, NR, SR and potential halo/bridge in its low-resolution tapered image in which previous observations failed to do. This potential halo or bridge however, was found only at a 2σ level.

We have also shown the importance of applying newer calibration and imaging techniques to MeerKAT data. These newer 3GC calibration techniques are employed through the `CubiCal` and `killMS` software in conjunction with the `DDFacet` imaging software. In both instances, we see significant improvement in the image quality and overall fidelity for the clusters ZwCl 2341 and A2631 of these wide-bandwidth and wide FoV observations. These types of improvements allow us to estimate the flux densities of diffuse radio sources more reliably after eliminating artefacts caused by off-axis strong sources, thereby laying down a firm foundation to more accurately study diffuse radio sources in these environments.

Several statistical parameters were also calculated to quantify the improvements after DD calibration. In our overall analysis, we saw that SUM NEG, MIN, RMS and MAD are all decreasing and the DR increasing in going from the DI to DD images. These trends are indicative of the visually clear improvements around the strong sources affected by artefacts.

We have performed simple 1-D spectral index plots for the two relics and central diffuse source in the ZwCl 2341 system using data from older observations of V09 combined with our new MeerKAT and uGMRT observations. Spectral studies are important for sources such as relics as they give us information on the particle acceleration mechanisms in these cluster outskirt regions thus providing information on the cluster formation history. We have found that our spectra results for the relics are flatter as compared to the more recent analyses of P21, G10 and B17, respectively, and slightly steeper than the older analyses of B02 and V09, respectively: $\alpha_{B17}, \alpha_{G10}, \alpha_{P21} < \alpha_{\mathrm{Currentwork}} < \alpha_{B02}, \alpha_{V09}$. However, in analyzing these previous observations, we can see no clear agreement on the actual values for the double relics. When compared to the most recent analysis by P21, we found no break in the spectra of the north relic between 235-1400 MHz and find our NR curve to fit well within the error bars.

6.1 Future work

The *Saraswati* supercluster contains several gravitationally bound clusters and groups making it an ideal object for radio studies of cluster mergers. Our work is based on the recently published *MOSS I: Double radio relics in the Saraswati supercluster* (P21). Future work will be in the form of *MOSS II: Spectral studies of diffuse radio sources in the Saraswati supercluster* and *MOSS III: Radio properties of galaxies in the core region of the Saraswati supercluster*. These future papers will cover a range of astrophysical topics within the *Saraswati* supercluster including cluster merger properties, magnetic field distributions across cluster volumes, broadband spectral analysis of diffuse radio sources, radio source identification with optical/IR counterparts, radio properties of galaxies and generating their catalogues. In the paper MOSS II, we wish to give a detailed analysis of the relics in ZwCl 2341 and the corresponding combined sub-band spectral index 2D map for both MeerKAT and uGMRT data (Kincaid et al .prep). For these spectral studies, we want to make use of the available JVLA S-band archival data for the high-frequency component of the spectra. We are also applying MeerKAT open time for UHF band (550 – 800 MHz) observations in the upcoming MeerKAT proposal call.

The MeerKAT Galaxy Cluster Legacy Survey (MGCLS) (Knowles et al., 2021) was a 2018 programme of long-track MeerKAT L-band (900–1670 MHz) observations of 115 galaxy clusters, observed for $\sim$ 6–10 hours each in full polarisation. The first legacy products data release (DR1) from this survey have been made public with the release of this paper. It includes MeerKAT raw visibilities and basic image products. Initial results have revealed a large number of interesting objects of potential scientific value in the area of cluster diffuse emission. Some of these fields contain a number of strong sources producing artefact's in much the same way as was seen in Figures 4.1 and 4.2 of this work. We have seen the applicability of the `CubiCal` and `killMS` calibration techniques in our work in reducing the artefacts of bright sources. As a test case, we are working with three MGCLS fields, J0943.4-7619, RXCJ0225.1-2928 and RXCJ1358.9-4750 that have poor image quality due to the presence of strong artefacts. We downloaded the raw visibility data of these three clusters and have applied our `CARACal` pipeline which will be followed by application of DD calibration software.

Appendix A

International system of units

PHYSICAL AND ASTRONOMICAL CONSTANTS

c	Speed of light in vacuo	2.998×10^8 m s^{-1}
H_0	Hubble constant	70 km s^{-1} Mpc
h_{70}	Dimensionless hubble parameter	70
$M_\odot$	Solar Mass	1.989×10^{30} kg
$L_\odot$	Solar Luminosity	3.83×10^{33} erg s^{-1}
1 Jy	Jansky	10^{26} W m^{-2} Hz^{-1}
1 pc	Parsec	3.086×10^{16} m
1 erg	erg	10^7J
1°	Degree	$\frac{\pi}{180}$ rad
1 ”	Arcsecond	$\frac{\pi}{180\times3600}$ rad
G	Gauss	10^{-4} kg A^{-1} s^{-2}
1 eV	Electronvolt	1.602×10^{-19} J

Appendix B

Symbols and notations

R_{500}	The radius within which the mean overdensity of the cluster is 500 times the critical density at the cluster redshift.
M_{500}	Mass within R_{500}
$P_{1.4GHz}$	Radio power at 1.4 GHz
L_X	X-ray luminosity
σ_{rms}	RMS sensitivity/thermal noise
A_e	Antenna collecting area
T_{sys}	System temperature
T_X	Cluster temperature
$\boldsymbol{J}$	arbitrary 2×2 Jones matrix
$\boldsymbol{G}$	direction-independant 2×2 Jones matrix
$\boldsymbol{E}$	direction-dependant 2×2 Jones matrix
$(\cdot)^H$	Hermitian transpose
$(\cdot)^*$	Complex conjugate
$\|\| \cdot \|\|$	Norm
$*$	Convolution operator
$\langle \cdot \rangle$	Averaging operator
B	Brightness matrix
X	Source coherency matrix
$V(u,v,w)$	Complex visibilities/source coherency function
uv	Visibilities domain
lm	Image domain
$I(l,m,n)$	Intensity distribution/Sky brightness/Spectral intensity function

I^D	Dirty image
$\mathcal{I}(l,m)$	True image
B	PSF or Dirty beam
δ	Dirac-delta function
$\mathcal{R}$	Abell richness group
s	Standard deviation
$\hat{x}$	Mean
z	Redshift
α	Spectral index
$\mathcal{M}$	Mach number

Appendix C

Abbreviations

Abbreviation	Full name
λCDM	λ Cold Dark Matter
1GC	1st generation calibration
2GC	2nd generation calibration
3GC	3rd generation calibration
AGN	Active Galactic Nuclei
AIPS	Astronomical Image Processing System
ASCA	Advanced Satellite for Cosmology and Astrophysics
CASA	Common Astronomy Software
CR	cosmic-ray
DD	direction-dependent
DDE	direction-dependent effects
DECaLS	DeCAM legacy survey
DI	direction-independent
DIE	direction-independent effects
DR	dynamic range
EM	electromagnetic waves
FAST	Five-hundred-meter Aperture Spherical Telescope
FFT	Fast Fourier Transform
FITS	Flexible Image Transport System
FoV	field of view
FT	Fourier Transform

Abbreviation	**Full name**
FWHM	full width at half maximum
GMRT	Giant Metrewave Radio Telescope
HERA	Hydrogen Epoch of Re-ionisation Array
IC	inverse-Compton
ICM	intra-cluster medium
IGM	inter-galactic medium
ISM	inter-stellar medium
JVLA	Upgraded Very Large Array
KAT-7	7 dish Karoo Array Telescope
KURT	Kurtosis
LLS	largest linear size
LOFAR	Low-Frequency Array
LoTSS	LOFAR Two-metre Sky Survey
LSS	large scale structure
LTA	Long Term Accumulation
MAD	Mean Absolute Deviation
MeerKAT	(Meer) Karoo Array Telescope
MFS	multi-frequency synthesis
MHD	magnetohydrodynamics
Mpc	Megaparsec
MS	Measurement Set
MWA	Murchison Widefield Array
MVFv4	MeerKAT Visibility Format version 4
NVSS	NRAO VLA sky survey
PSF	Point Spread Function
RFI	Radio Frequency Interference
RGB	red green blue

Abbreviation	**Full name**
ROSAT	ROentgen SATellite
RIME	Radio Interferometric Measurement Equation
RMS	root mean square
SDSS	Sloan Digital Sky Survey
SKEW	Skewness
SNR	Signal to Noise Ratio
SSD	Sub-Space Deconvolution
SUM	SUM of negative pixel values
uGMRT	upgraded Giant Metrewave Radio Telescope
vCZ	van Cittert–Zernike
VLA	Very Large Array
YAML	Yet Another Markup Language

Appendix D

Software

General radio astronomy software	
`AIPS`	The first software package containing a reliable and comprehensive set of algorithms for data-reduction for both interferometric and single dish radio data.
`CASA`	A set of tools built on the existing suite of C++ libraries developed by `AIPS` for the reduction and analysis of both interferometric and single dish radio data.
`Obit`	A group of software packages for handling radio astronomy data.
`SPAM`	A set of AIPS-based data reduction scripts that includes ionospheric calibration.
CARACal and DD Software	
`AOFlagger`	General-purpose automated RFI flagging tool developed originally for LOFAR.
`CARACal`	Fully automated MeerKAT data analysis pipeline.
`CubiCal`	Python-based software using the differential gains peeling method for DD calibration.
`DDFacet`	Python-based software for facet-based imaging.
`killMS`	Python-based software using a facet-based approach for DD calibration.
`MeqTrees`	A tool for rapid implementation of measurement equations to radio interferometric data for the purpose of simulations and calibration.
`Montage`	An astronomical imaging toolkit are used for assembling FITS images into custom mosaics.
`Ragavi`	An interactive tool for plotting interferometric visibilities.
`Radiopadre`	A jupyter notebook framework for quick and easy visualization of radio astronomical products from pipelines.
`RFinder`	A set of tools used for identifying the presence and visualisation of RFI in an observation.
`ShadeMS`	A fast tool for plotting interferometric visibilities from a MS.
`Stimela`	A platform independent radio interferometry based on Python scripting framework and containerisation technologies.
`SoFiA`	source finding pipeline for detecting and characterising galaxies in three-dimensional HI data cubes.
`Sunblocker`	A Python method to remove solar-like RFI from interferometric data.

Visualisation and other software	
`DS9`	An astronomical imaging and data visualisation software.
`CARTA`	Cube analysis and rendering data visualisation tool for astronomy.
`Tigger`	Local Sky Model (LSM) manager and FITS image viewer.
`CASA Viewer`	Stand-alone `CASA` data visualisation software tool.
`Parsel Tongue`	A software package that allows for the use of `AIPS` based functionality through a Python interface.
`surfvis`	Creates per-baseline time/frequency plots from a MS that is order of magnitudes faster than `CASA`.
Containerisation Software	
The three main containerisation software, `Docker`, `Podman` and `Singularity` used for building and restoring container images.	

Appendix E

Software links

General radio astronomy software	
`AIPS`	`http://www.aips.nrao.edu/index.shtml`
`CASA`	`https://casa.nrao.edu/`
`Obit`	`https://github.com/bill-cotton/Obit`
`SPAM`	`http://www.intema.nl/doku.php?id=huibintemaspam`
CARACal and DD software	
`Aimfast`	`https://github.com/Athanaseus/aimfast/`
`AOFlagger`	`https://github.com/pkgw/aoflagger`
`CARACal`	`https://github.com/caracal-pipeline/caracal`
`CrystalBall`	`https://github.com/paoloserra/crystalball/`
`CubiCal`	`https://github.com/ratt-ru/CubiCal`
`DDFacet`	`https://github.com/cyriltasse/DDFacet`
`killMS`	`https://github.com/cyriltasse/killMS`
`MeqTrees`	`http://meqtrees.net/`
`PyBDSF`	`https://github.com/lofar-astron/PyBDSF/`
`TRIColour`	`https://github.com/ska-sa/tricolour/`
`WSClean`	`https://sourceforge.net/projects/wsclean/`
Containerisation software	
`Docker`	`https://www.docker.com`
`Podman`	`https://podman.io`
`Singularity`	`https://sylabs.io/singularity/`

Visualisation and other software	
`CARTA`	https://cartavis.org/
`CASA Viewer`	https://casa.nrao.edu/
`DS9`	https://ds9.si.edu
`Software developed by RATT group`	https://github.com/ratt-ru
`surfvis`	https://github.com/ratt-ru/surfvis
`Tigger`	https://github.com/ska-sa/tigger

Appendix F

DDFacet, CubiCal and killMS parameter list

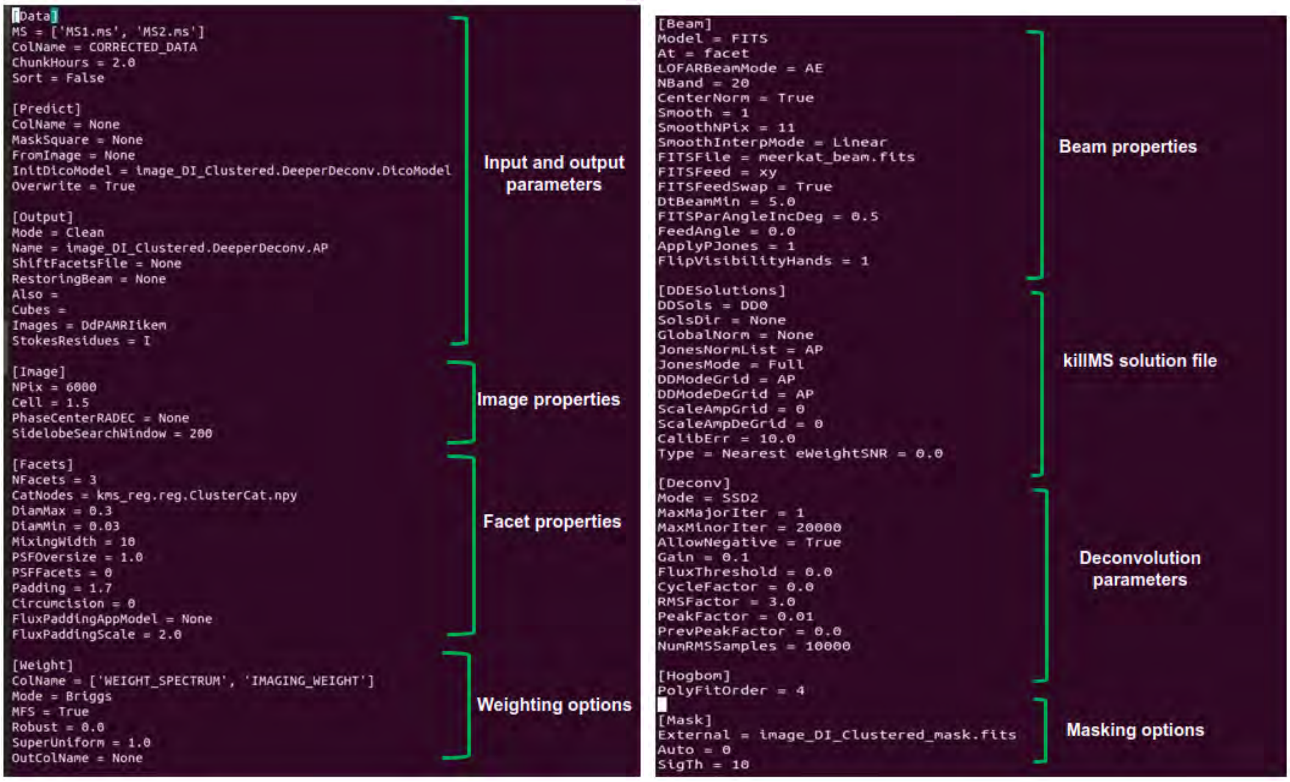

```
[Data]
MS = ['MS1.ms', 'MS2.ms']
ColName = CORRECTED_DATA
ChunkHours = 2.0
Sort = False

[Predict]
ColName = None
MaskSquare = None
FromImage = None
InitDicoModel = image_DI_Clustered.DeeperDeconv.DicoModel
Overwrite = True

[Output]
Mode = Clean
Name = image_DI_Clustered.DeeperDeconv.AP
ShiftFacetsFile = None
RestoringBeam = None
Also =
Cubes =
Images = DdPAMRIikem
StokesResidues = I

[Image]
NPix = 6000
Cell = 1.5
PhaseCenterRADEC = None
SidelobeSearchWindow = 200

[Facets]
NFacets = 3
CatNodes = kms_reg.reg.ClusterCat.npy
DiamMax = 0.3
DiamMin = 0.03
MixingWidth = 10
PSFOversize = 1.0
PSFFacets = 0
Padding = 1.7
Circumcision = 0
FluxPaddingAppModel = None
FluxPaddingScale = 2.0

[Weight]
ColName = ['WEIGHT_SPECTRUM', 'IMAGING_WEIGHT']
Mode = Briggs
MFS = True
Robust = 0.0
SuperUniform = 1.0
OutColName = None
```

```
[Beam]
Model = FITS
At = facet
LOFARBeamMode = AE
NBand = 20
CenterNorm = True
Smooth = 1
SmoothNPix = 11
SmoothInterpMode = Linear
FITSFile = meerkat_beam.fits
FITSFeed = xy
FITSFeedSwap = True
DtBeamMin = 5.0
FITSParAngleIncDeg = 0.5
FeedAngle = 0.0
ApplyPJones = 1
FlipVisibilityHands = 1

[DDESolutions]
DDSols = DD0
SolsDir = None
GlobalNorm = None
JonesNormList = AP
JonesMode = Full
DDModeGrid = AP
DDModeDeGrid = AP
ScaleAmpGrid = 0
ScaleAmpDeGrid = 0
CalibErr = 10.0
Type = Nearest eWeightSNR = 0.0

[Deconv]
Mode = SSD2
MaxMajorIter = 1
MaxMinorIter = 20000
AllowNegative = True
Gain = 0.1
FluxThreshold = 0.0
CycleFactor = 0.0
RMSFactor = 3.0
PeakFactor = 0.01
PrevPeakFactor = 0.0
NumRMSSamples = 10000

[Hogbom]
PolyFitOrder = 4

[Mask]
External = image_DI_Clustered_mask.fits
Auto = 0
SigTh = 10
```

Figure F.1: `DDFacet` example parset file including some parameters.

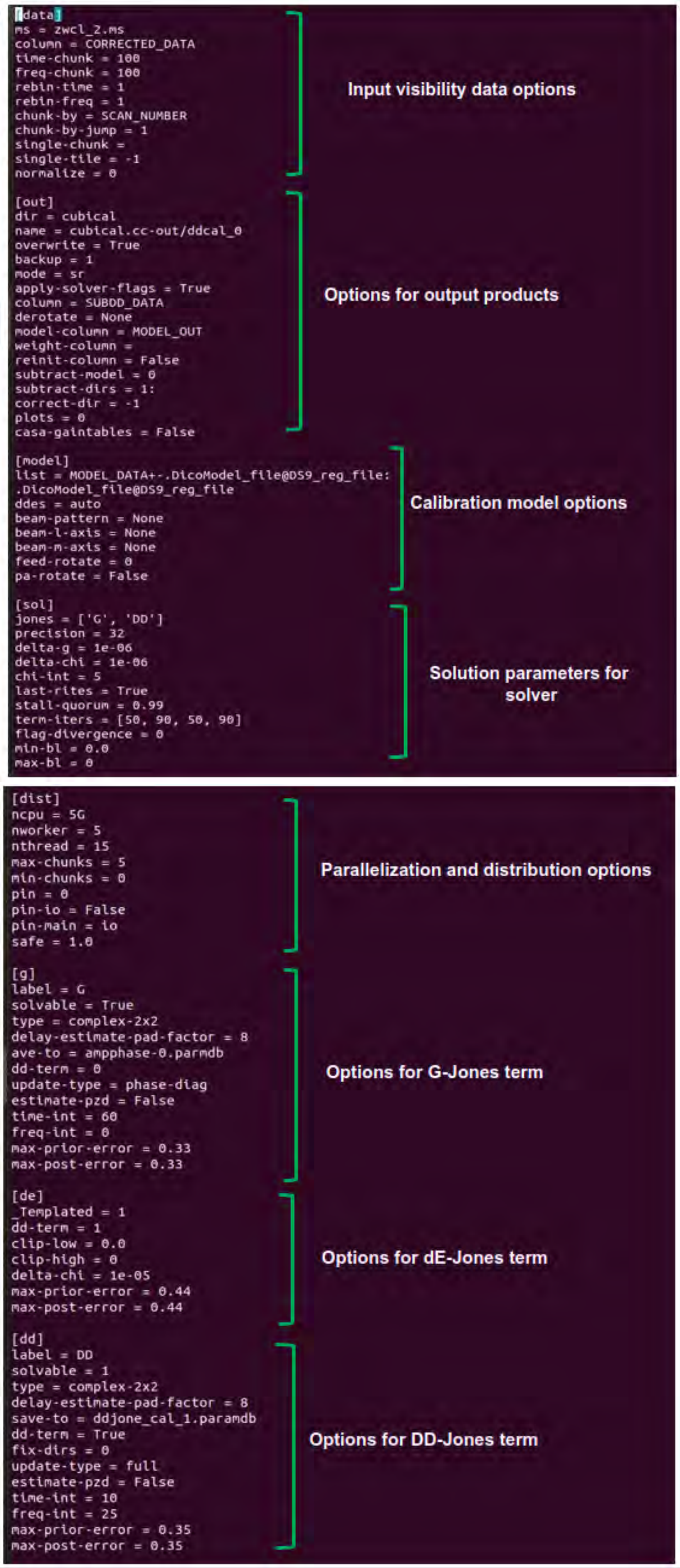

```
[data]
ms = zwcl_2.ms
column = CORRECTED_DATA
time-chunk = 100
freq-chunk = 100
rebin-time = 1
rebin-freq = 1
chunk-by = SCAN_NUMBER
chunk-by-jump = 1
single-chunk =
single-tile = -1
normalize = 0

[out]
dir = cubical
name = cubical.cc-out/ddcal_0
overwrite = True
backup = 1
mode = sr
apply-solver-flags = True
column = SUBDD_DATA
derotate = None
model-column = MODEL_OUT
weight-column =
reinit-column = False
subtract-model = 0
subtract-dirs = 1:
correct-dir = -1
plots = 0
casa-gaintables = False

[model]
list = MODEL_DATA+-.DicoModel_file@DS9_reg_file:
.DicoModel_file@DS9_reg_file
ddes = auto
beam-pattern = None
beam-l-axis = None
beam-m-axis = None
feed-rotate = 0
pa-rotate = False

[sol]
jones = ['G', 'DD']
precision = 32
delta-g = 1e-06
delta-chi = 1e-06
chi-int = 5
last-rites = True
stall-quorum = 0.99
term-iters = [50, 90, 50, 90]
flag-divergence = 0
min-bl = 0.0
max-bl = 0
```

```
[dist]
ncpu = 5G
nworker = 5
nthread = 15
max-chunks = 5
min-chunks = 0
pin = 0
pin-io = False
pin-main = io
safe = 1.0

[g]
label = G
solvable = True
type = complex-2x2
delay-estimate-pad-factor = 8
ave-to = ampphase-0.parmdb
dd-term = 0
update-type = phase-diag
estimate-pzd = False
time-int = 60
freq-int = 0
max-prior-error = 0.33
max-post-error = 0.33

[de]
_Templated = 1
dd-term = 1
clip-low = 0.0
clip-high = 0
delta-chi = 1e-05
max-prior-error = 0.44
max-post-error = 0.44

[dd]
label = DD
solvable = 1
type = complex-2x2
delay-estimate-pad-factor = 8
save-to = ddjone_cal_1.paramdb
dd-term = True
fix-dirs = 0
update-type = full
estimate-pzd = False
time-int = 10
freq-int = 25
max-prior-error = 0.35
max-post-error = 0.35
```

Figure F.2: `CubiCal` example parset file including some parameters.

```
 --MSName=VISDATA_MSNAME
                    Input MS to draw [no default]
  --TChunk=VISDATA_TCHUNK
                    Time Chunk in hours. Default is 15
  --InCol=VISDATA_INCOL
                    Column to work on. Default is CORRECTED_DATA_BACKUP
  --OutCol=VISDATA_OUTCOL
                    Column to write to. Default is CORRECTED_DATA
  --FreePredictColName=VISDATA_FREEPREDICTCOLNAME

*
  --BaseImageName=IMAGESKYMODEL_BASEIMAGENAME
                    Default
  --ImagePredictParset=IMAGESKYMODEL_IMAGEPREDICTPARSET
                    Default
  --DicoModel=IMAGESKYMODEL_DICOMODEL
                    Default none
  --MaxFacetSize=IMAGESKYMODEL_MAXFACETSIZE
                    Default none
  --MinFacetSize=IMAGESKYMODEL_MINFACETSIZE
                    Default none

*
  --BeamModel=BEAM_BEAMMODEL
                    Apply beam model, Can be set to: None/LOFAR. Default
                    is none
  --BeamAt=BEAM_BEAMAT
                    Where to apply beam model, Can be set to:
                    tessel/facet. Default is tessel
  --LOFARBeamMode=BEAM_LOFARBEAMMODE
                    LOFAR beam mode. "AE" sets the beam model to Array and
  --NChanBeamPerMS=BEAM_NCHANBEAMPERMS
                    Number of channel in the Beam Jones matrix. Default is
                    1
  --FITSParAngleIncDeg=BEAM_FITSPARANGLEINCDEG
                    Estimate the beam every this PA change [in deg].
                    Default is 5
  --FITSFile=BEAM_FITSFILE
                    FITS beam mode filename template. Default is none

*
  --DoPlot=ACTIONS_DOPLOT
                    Plot the solutions, for debugging. Default is 0
  --NCPU=ACTIONS_NCPU
                    Number of cores to use. Default is 1
  --NThread=ACTIONS_NTHREAD
                    Number of OMP/BLAS/etc. threads to use. Default is 1
  --UpdateWeights=ACTIONS_UPDATEWEIGHTS
                    Update imaging weights. Default is 1
  --DebugPdb=ACTIONS_DEBUGPDB
                    Drop into Pdb on error. Default is 1
```

```
*
  --ExtSols=SOLUTIONS_EXTSOLS
                    External solution file. If set, will not solve.
  --ApplyMode=SOLUTIONS_APPLYMODE
                    Subtract selected sources.
  --ClipMethod=SOLUTIONS_CLIPMETHOD
                    Clip data in the IMAGING_WEIGHT column. Can be set to
                    Resid, DDEResid or ResidAnt . Default is ['ResidAnt']
  --OutSolsName=SOLUTIONS_OUTSOLSNAME
                    If specified will save the estimated solutions in this
                    file. Default is
  --ApplyToDir=SOLUTIONS_APPLYTODIR
                    Apply direction averaged gains to residual data in the
                    mentioned direction.     If ApplyCal=-1 takes the mean
                    gain over directions. -2 if off. Default is -2
  --MergeBeamToAppliedSol=SOLUTIONS_MERGEBEAMTOAPPLIEDSOL
                    Use the beam in applied solution. Default is 0
  --SkipExistingSols=SOLUTIONS_SKIPEXISTINGSOLS
                    Skipping existing solutions if they exist. Default is
                    0
  --SolsDir=SOLUTIONS_SOLSDIR
                    Directory in which to save the solutions. Default is
                    none

*
   --SolverType=SOLVERS_SOLVERTYPE
                    Name of the solver to use (CohJones/KAFCA)
  --PrecisionDot=SOLVERS_PRECISIONDOT
                    Dot product Precision (S/D). Default is D.
  --PolMode=SOLVERS_POLMODE
                    Polarisation mode (Scalar/IFull). Default is Scalar
  --dt=SOLVERS_DT   Time interval for a solution [minutes]. Default is 30.
  --NChanSols=SOLVERS_NCHANSOLS
                    Number of solutions along frequency axis. Default is
                    1.

*
  --NIterLM=COHJONES_NITERLM
                     Number of iterations for the solve. Default is 7
  --LambdaLM=COHJONES_LAMBDALM
                     Lambda parameter for CohJones. Default is 1
  --LambdaTk=COHJONES_LAMBDATK
                     Tikhonov regularisation parameter. Default is 0.0

*
  --NIterKF=KAFCA_NITERKF
                     Number of iterations for the solve. Default is 6
  --LambdaKF=KAFCA_LAMBDAKF
                     Lambda parameter for KAFCA. Default is 0.5
  --InitLM=KAFCA_INITLM
                    Initialise Kalman filter with Levenberg Maquardt.
                    Default is 0
  --InitLMdt=KAFCA_INITLMDT
                    Time interval in minutes. Default is 5
```

Figure F.3: `killMS` help file including some parameters.

Appendix G

CaraCal .yml example script and workers

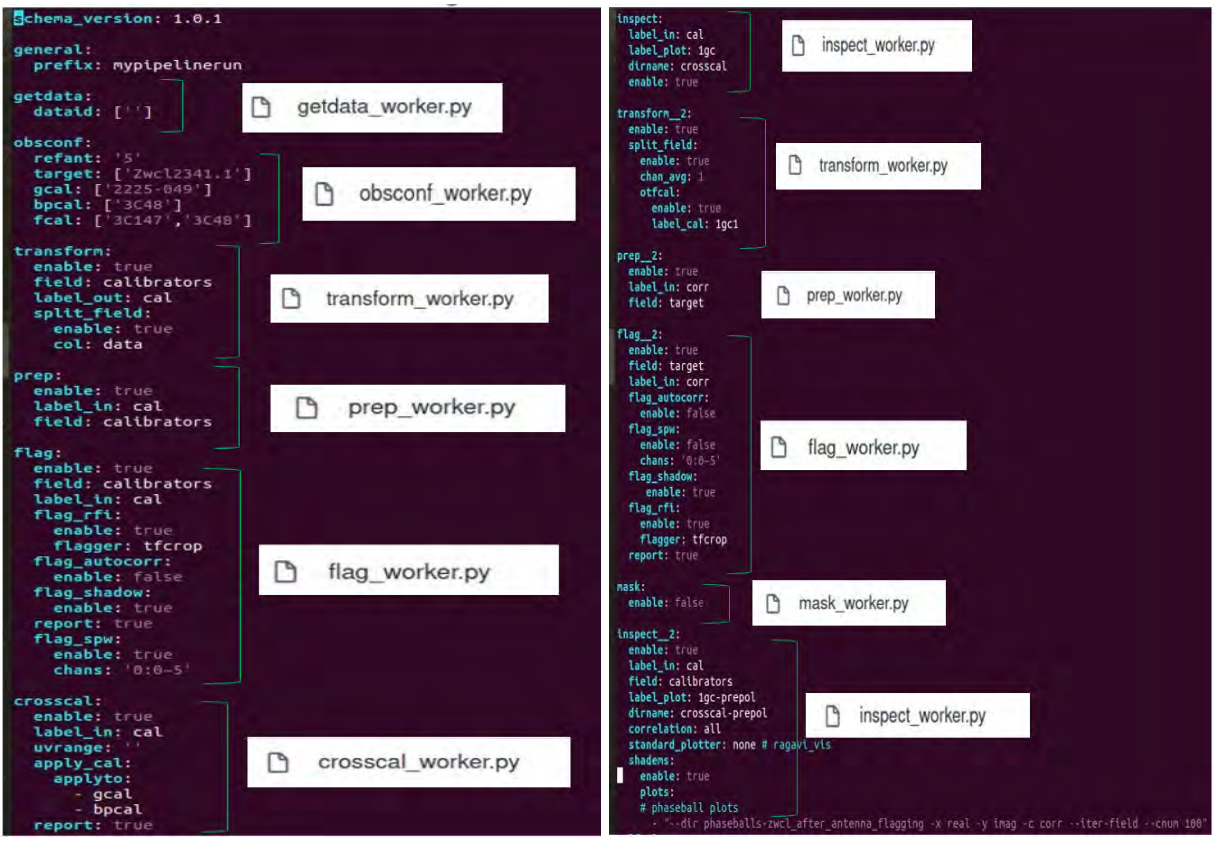

```
schema_version: 1.0.1

general:
  prefix: mypipelinerun

getdata:
  dataid: ['']

obsconf:
  refant: '5'
  target: ['Zwcl2341.1']
  gcal: ['2225-049']
  bpcal: ['3C48']
  fcal: ['3C147','3C48']

transform:
  enable: true
  field: calibrators
  label_out: cal
  split_field:
    enable: true
    col: data

prep:
  enable: true
  label_in: cal
  field: calibrators

flag:
  enable: true
  field: calibrators
  label_in: cal
  flag_rfi:
    enable: true
    flagger: tfcrop
  flag_autocorr:
    enable: false
  flag_shadow:
    enable: true
  report: true
  flag_spw:
    enable: true
    chans: '0:0~5'

crosscal:
  enable: true
  label_in: cal
  uvrange: ''
  apply_cal:
    applyto:
      - gcal
      - bpcal
  report: true
```

```
inspect:
  label_in: cal
  label_plot: 1gc
  dirname: crosscal
  enable: true

transform__2:
  enable: true
  split_field:
    enable: true
    chan_avg: 1
    otfcal:
      enable: true
      label_cal: 1gc1

prep__2:
  enable: true
  label_in: corr
  field: target

flag__2:
  enable: true
  field: target
  label_in: corr
  flag_autocorr:
    enable: false
  flag_spw:
    enable: false
    chans: '0:0~5'
  flag_shadow:
     enable: true
  flag_rfi:
    enable: true
    flagger: tfcrop
  report: true

mask:
  enable: false

inspect__2:
  enable: true
  label_in: cal
  field: calibrators
  label_plot: 1gc-prepol
  dirname: crosscal-prepol
  correlation: all
  standard_plotter: none # ragavi_vis
  shadems:
    enable: true
    plots:
    # phaseball plots
      - "--dir phaseballs-zwcl_after_antenna_flagging -x real -y imag -c corr --iter-field --cnum 100"
```

Figure G.1: `CARACal` example .yml file showing the workers on the left, each encapsulated by a green right bracket. The corresponding worker .py script is shown in the white box on the right of each worker. The tasks are indented to the right under each worker name. The parameters for each worker are shown in purple.

Appendix H

MeerKAT observation plots

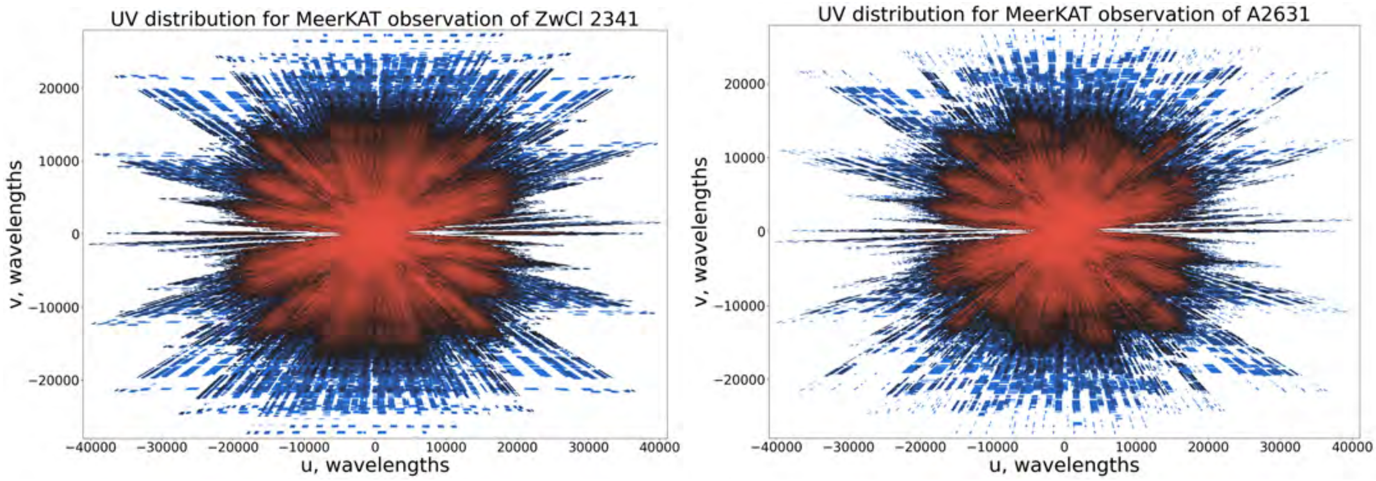

Figure H.1: *uv* distribution plots for the MeerKAT observations of ZwCl 2341 (*left*) and A2631 (*right*).

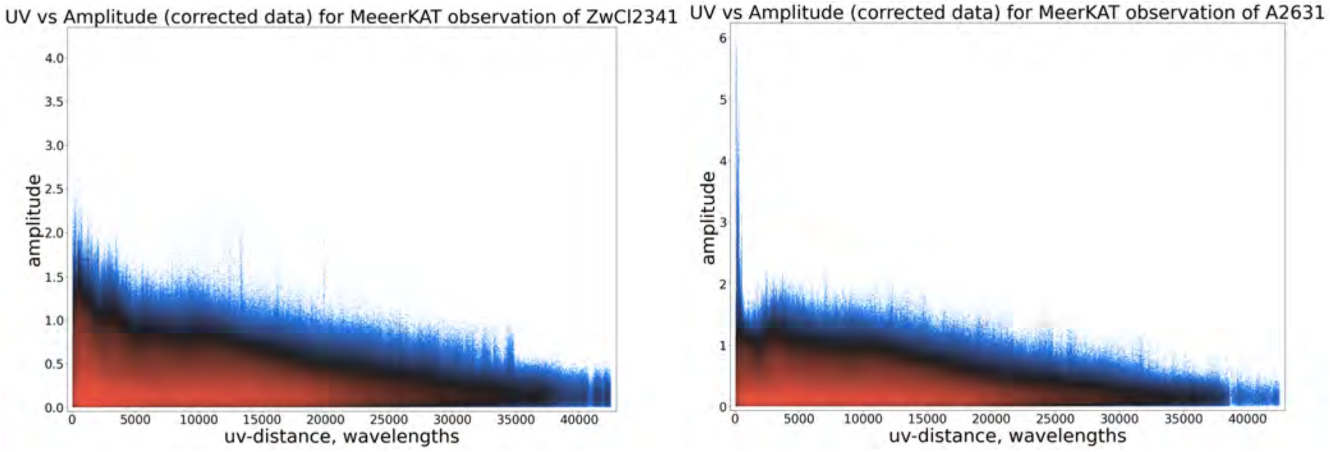

Figure H.2: *uv* vs amplitude plots for the MeerKAT observations of ZwCl 2341 (*left*) and A2631 (*right*).

Bibliography

Abazajian, K. N., Adelman-McCarthy, J. K., Agüeros, M. A., et al. 2009, The Astrophysical Journal Supplement Series, 182, 543

Abell, G. O. 1958, The Astrophysical Journal Supplement Series, 3, 211

Ade, P., Aghanim, N., Arnaud, M., et al. 2016, Astronomy & Astrophysics, 594, A24

Ade, P. A., Aghanim, N., Armitage-Caplan, C., et al. 2014, Astronomy & Astrophysics, 571, A29

Akamatsu, H., & Kawahara, H. 2013, Publications of the Astronomical Society of Japan, 65

Ananthakrishnan, S. 2005

Aragón-Calvo, M. A., van de Weygaert, R., Jones, B. J., & Van Der Hulst, J. 2007, The Astrophysical Journal Letters, 655, L5

Armel Mbou Sob, U., Landman Bester, H., Smirnov, O. M., Kenyon, J., & Russeeawon, C. 2021, arXiv e-prints, arXiv

Baars, J., Genzel, R., Pauliny-Toth, I., & Witzel, A. 1977, Astronomy and Astrophysics, 61, 99

Bagchi, J., Enßlin, T. A., Miniati, F., et al. 2002, New Astronomy, 7, 249

Bagchi, J., Sankhyayan, S., Sarkar, P., et al. 2017, The Astrophysical Journal, 844, 25

Bahcall, N. A. 1988, Annual review of astronomy and astrophysics, 26, 631

—. 1996, arXiv preprint astro-ph/9611148

—. 1999, Formation of Structure in the Universe, 4, 135

Bednarz, J., & Ostrowski, M. 1996, Monthly Notices of the Royal Astronomical Society, 283, 447

Begelman, M., & Rees, M. 1996, The Observatory, 116, 245

Ben-Kiki, O., Evans, C., & Ingerson, B. 2009, Working Draft 2008-05, 11

Benson, B., Wittman, D. M., Golovich, N., et al. 2017, The Astrophysical Journal, 841, 7

Bhukta, N., Pal, S., & Mondal, S. K. 2022, arXiv preprint arXiv:2201.12353

Biernaux, J., Magain, P., Sluse, D., & Chantry, V. 2016, Astronomy & Astrophysics, 585, A84

Blandford, R., & Eichler, D. 1987, Physics Reports, 154, 1

Blasi, P., & Colafrancesco, S. 1999, Astroparticle Physics, 12, 169

Böhringer, H., Schuecker, P., Pratt, G., et al. 2007, Astronomy & Astrophysics, 469, 363

Bonafede, A., Giovannini, G., Feretti, L., Govoni, F., & Murgia, M. 2009a, Astronomy & Astrophysics, 494, 429

Bonafede, A., Intema, H., Brüggen, M., et al. 2014, The Astrophysical Journal, 785, 1

Bonafede, A., Feretti, L., Giovannini, G., et al. 2009b, Astronomy & Astrophysics, 503, 707

Bonafede, A., Brüggen, M., van Weeren, R., et al. 2012, Monthly Notices of the Royal Astronomical Society, 426, 40

Bonafede, A., Cassano, R., Brüggen, M., et al. 2017, Monthly Notices of the Royal Astronomical Society, 470, 3465

Bonafede, A., Brunetti, G., Vazza, F., et al. 2021, The Astrophysical Journal, 907, 32

Bond, J. R., Kofman, L., & Pogosyan, D. 1996, , 380, 603

Booth, R., De Blok, W., Jonas, J., & Fanaroff, B. 2009, arXiv preprint arXiv:0910.2935

Booth, R., & Jonas, J. 2012, African Skies, 16, 101

Boschin, W., Barrena, R., & Girardi, M. 2010, Astronomy & Astrophysics, 521, A78

Boschin, W., Girardi, M., & Barrena, R. 2013, Monthly Notices of the Royal Astronomical Society, 434, 772

Botteon, A., Shimwell, T., Bonafede, A., et al. 2018, Monthly Notices of the Royal Astronomical Society, 478, 885

Botteon, A., Cassano, R., Eckert, D., et al. 2019, arXiv preprint arXiv:1908.07527

Botteon, A., van Weeren, R., Brunetti, G., et al. 2020, Monthly Notices of the Royal Astronomical Society: Letters, 499, L11

Braun, R. 2013, Astronomy & Astrophysics, 551, A91

Briggs, D. 1995a, in American Astronomical Society Meeting Abstracts, Vol. 187, 112–02

Briggs, D. S. 1995b, Ph. D. Thesis

Brown, S., Duesterhoeft, J., & Rudnick, L. 2011, The Astrophysical Journal Letters, 727, L25

Brown, S., & Rudnick, L. 2011, Monthly Notices of the Royal Astronomical Society, 412, 2

Brüggen, M., Reiprich, T., Bulbul, E., et al. 2021, Astronomy & Astrophysics, 647, A3

Brunetti, G., Blasi, P., Reimer, O., et al. 2012, Monthly Notices of the Royal Astronomical Society, 426, 956

Brunetti, G., Cassano, R., Dolag, K., & Setti, G. 2009, Astronomy & Astrophysics, 507, 661

Brunetti, G., & Jones, T. W. 2014, International Journal of Modern Physics D, 23, 1430007

Brunetti, G., Setti, G., Feretti, L., & Giovannini, G. 2001, Monthly Notices of the Royal Astronomical Society, 320, 365

Brunetti, G., & Vazza, F. 2020, Physical Review Letters, 124, 051101

Brunetti, G., Venturi, T., Dallacasa, D., et al. 2007, The Astrophysical Journal Letters, 670, L5

Buch, K. D., Gupta, Y., Bhatporia, S., et al. 2016, in 2016 Radio Frequency Interference (RFI), IEEE, 11–15

Bykov, A., Bloemen, H., & Uvarov, Y. A. 2000, Astronomy and Astrophysics, 362, 886

Bykov, A., Dolag, K., & Durret, F. 2008, Clusters of Galaxies, 119

Calzetta, E., & Hu, B. 1995, Physical Review D, 52, 6770

Carretti, E., Brown, S., Staveley-Smith, L., et al. 2013, Monthly Notices of the Royal Astronomical Society, 430, 1414

Cassano, R. 2009, arXiv preprint arXiv:0902.2971

Cassano, R., Ettori, S., Giacintucci, S., et al. 2010, The Astrophysical Journal Letters, 721, L82

Cassano, R., Ettori, S., Brunetti, G., et al. 2013, The Astrophysical Journal, 777, 141

Chibueze, J. O., Akamatsu, H., Parekh, V., et al. 2021

Cho, H., Jee, M. J., Smith, R., Finner, K., & Lee, W. 2022, The Astrophysical Journal, 925, 68

Clowe, D., Randall, S., & Markevitch, M. 2007, Nuclear Physics B-Proceedings Supplements, 173, 28

Condon, J. J., Cotton, W., Greisen, E., et al. 1998, The Astronomical Journal, 115, 1693

Cornwell, T. 2009, Astronomy & Astrophysics, 500, 65

Cornwell, T., & Braun, R. 1989, in Synthesis imaging in radio astronomy, Vol. 6, 167

Cornwell, T., & Perley, R. 1992, Astronomy and Astrophysics, 261, 353

Cornwell, T. J. 2008, IEEE Journal of selected topics in signal processing, 2, 793

Cornwell, T. J., Golap, K., & Bhatnagar, S. 2008, IEEE Journal of Selected Topics in Signal Processing, 2, 647

Cuciti, V., Cassano, R., Brunetti, G., et al. 2021, Astronomy & Astrophysics, 647, A50

De Gasperin, F., van Weeren, R., Brüggen, M., et al. 2014, Monthly Notices of the Royal Astronomical Society, 444, 3130 de Gasperin, F., Rudnick, L., Finoguenov, A., et al. 2021, arXiv preprint arXiv:2111.06940

DeBoer, D. R., Parsons, A. R., Aguirre, J. E., et al. 2017, Publications of the Astronomical Society of the Pacific, 129, 045001

Dennison, B. 1980, The Astrophysical Journal, 239, L93

Dey, A., Schlegel, D. J., Lang, D., et al. 2019, The Astronomical Journal, 157, 168

Duchesne, S., Johnston-Hollitt, M., & Wilber, A. 2021, Publications of the Astronomical Society of Australia, 38

Edge, A., Stewart, G., & Fabian, A. 1992, Monthly Notices of the Royal Astronomical Society, 258, 177

Enßlin, T., Pfrommer, C., Miniati, F., & Subramanian, K. 2011, Astronomy & Astrophysics, 527, A99

Ensslin, T. A., Biermann, P. L., Klein, U., & Kohle, S. 1997, arXiv preprint astro-ph/9712293

Evrard, A. E., Metzler, C. A., & Navarro, J. F. 1995, arXiv preprint astro-ph/9510058

Fabian, A. C. 1994, Annual Review of Astronomy and Astrophysics, 32, 277

—. 2012, Clusters and Superclusters of Galaxies, Vol. 366 (Springer Science & Business Media)

Fanaroff, B. L., & Riley, J. M. 1974, Monthly Notices of the Royal Astronomical Society, 167, 31P

Felten, J., Gould, R., Stein, W., & Woolf, N. 1966, The Astrophysical Journal, 146, 955

Feretti, L., Brunetti, G., Giovannini, G., Govoni, F., & Setti, G. 2000, arXiv preprint astro-ph/0009346

Feretti, L., Brunetti, G., Giovannini, G., et al. 2004, arXiv preprint astro-ph/0412424

Feretti, L., Fusco-Femiano, R., Giovannini, G., & Govoni, F. 2001, Astronomy & Astrophysics, 373, 106

Feretti, L., Giovannini, G., Govoni, F., & Murgia, M. 2012, The Astronomy and Astrophysics Review, 20, 54

Ferrari, C., Govoni, F., Schindler, S., Bykov, A., & Rephaeli, Y. 2008, in Clusters of Galaxies (Springer), 93–118

Finoguenov, A., Böhringer, H., & Zhang, Y.-Y. 2005, Astronomy & Astrophysics, 442, 827

Giacintucci, S., Dallacasa, D., Venturi, T., et al. 2011, Astronomy & Astrophysics, 534, A57

Giovannini, G., Bonafede, A., Feretti, L., Govoni, F., & Murgia, M. 2010, Astronomy & Astrophysics, 511, L5

Giovannini, G., Bonafede, A., Feretti, L., et al. 2009, Astronomy & Astrophysics, 507, 1257

Giovannini, G., & Feretti, L. 2002, in Merging Processes in Galaxy Clusters (Springer), 197–227

Giovannini, G., Feretti, L., Venturi, T., Kim, K.-T., & Kronberg, P. 1993, The Astrophysical Journal, 406, 399

Giovannini, G., Tordi, M., & Feretti, L. 1999, New Astronomy, 4, 141

Giovannini, G., Cau, M., Bonafede, A., et al. 2020, Astronomy & Astrophysics, 640, A108

Girardi, M., & Biviano, A. 2002, in Merging Processes in Galaxy Clusters (Springer), 39–77

Govoni, F., Feretti, L., Giovannini, G., et al. 2001, Astronomy & Astrophysics, 376, 803

Govoni, F., Orrù, E., Bonafede, A., et al. 2019, Science, 364, 981

Greisen, E. W. 2003, in Information Handling in Astronomy-Historical Vistas (Springer), 109–125

Gupta, Y., Ajithkumar, B., Kale, H., et al. 2017, Curr. Sci, 113, 707

Hall, P., Schillizzi, R., Dewdney, P., & Lazio, J. 2008, International Union of Radio Science URSI, 236, 4

Hamaker, J., Bregman, J., & Sault, R. 1996, Astronomy and Astrophysics Supplement Series, 117, 137

Hamaker, J. P. 2000, Astronomy and Astrophysics supplement series, 143, 515

Hogbom, J., & Brouw, W. 1974, Astronomy and Astrophysics, 33, 289

Iheanetu, K., Girard, J., Smirnov, O., et al. 2019, Monthly Notices of the Royal Astronomical Society, 485, 4107

Intema, H. 2014, arXiv preprint arXiv:1402.4889

Intema, H., Jagannathan, P., Mooley, K., & Frail, D. 2017, Astronomy & Astrophysics, 598, A78

Intema, H., Van der Tol, S., Cotton, W., et al. 2009, Astronomy & Astrophysics, 501, 1185

Jaffe, W., & Rudnick, L. 1979, The Astrophysical Journal, 233, 453

Johnston, S., Taylor, R., Bailes, M., et al. 2008, Experimental astronomy, 22, 151

Johnston-Hollitt, M., & Pratley, L. 2017, arXiv preprint arXiv:1706.04930

Jonas, J., & Team, M. 2016, MeerKAT Science: On the Pathway to the SKA, 1

—. 2018, Proceedings of MeerKAT Science: On the Pathway to the SKA, 25

Jonas, J. L. 2009, Proceedings of the IEEE, 97, 1522

Jones, R. C. 1941, Josa, 31, 488

Józsa, G. I., White, S. V., Thorat, K., et al. 2020, arXiv preprint arXiv:2006.02955

Kale, R., Dwarakanath, K., Bagchi, J., & Paul, S. 2012, Monthly Notices of the Royal Astronomical Society, 426, 1204

Kale, R., Wik, D. R., Giacintucci, S., et al. 2017, Monthly Notices of the Royal Astronomical Society, 472, 940

Kang, H., & Ryu, D. 2011, The Astrophysical Journal, 734, 18

—. 2015, The Astrophysical Journal, 809, 186

Kardashev, N. S. 1962, Soviet Astronomy, 6, 317

Kenyon, J., Smirnov, O., Grobler, T., & Perkins, S. 2018, Monthly Notices of the Royal Astronomical Society, 478, 2399

Kettenis, M., van Langevelde, H. J., Reynolds, C., & Cotton, B. 2006, in Astronomical data analysis software and systems XV, Vol. 351, 497

Kleiner, D., Serra, P., Maccagni, F., et al. 2021, Astronomy & Astrophysics, 648, A32

Knowles, K., Baker, A. J., Bond, J. R., et al. 2019, Monthly Notices of the Royal Astronomical Society, 486, 1332

Knowles, K., Cotton, W., Rudnick, L., et al. 2021, arXiv e-prints, arXiv

Landau, L., & Lifshitz, E. 1959, New York, 61

Lang, K. R., & Lang, K. R. 2013, Essential astrophysics (Springer)

Liang, H., Hunstead, R., Birkinshaw, M., & Andreani, P. 2000, The Astrophysical Journal, 544, 686

Lietzen, H., Tempel, E., Liivamägi, L., et al. 2016, Astronomy & Astrophysics, 588, L4

Liivamägi, L. J., Tempel, E., & Saar, E. 2012, Astronomy & Astrophysics, 539, A80

Lindner, R. R., Baker, A. J., Hughes, J. P., et al. 2014, The Astrophysical Journal, 786, 49

Lonsdale, C. 2005, in From Clark Lake to the Long Wavelength Array: Bill Erickson's Radio Science, Vol. 345, 399

Macario, G., Markevitch, M., Giacintucci, S., et al. 2011, The Astrophysical Journal, 728, 82

Makhathini, S. 2018

Mandel, L., & Wolf, E. 1995, Optical coherence and quantum optics (Cambridge university press)

Markevitch, M. 2005, arXiv preprint astro-ph/0511345

Markevitch, M. 2012, in The Twelfth Marcel Grossmann Meeting: On Recent Developments in Theoretical and Experimental General Relativity, Astrophysics and Relativistic Field Theories (In 3 Volumes), World Scientific, 397–410

Markevitch, M., Gonzalez, A., David, L., et al. 2002, The Astrophysical Journal Letters, 567, L27

Markevitch, M., & Vikhlinin, A. 2001, The Astrophysical Journal, 563, 95

Markevitch, M., & Wilson, A. 2006, ESA SP-604: The X-ray Universe 2005

Mauch, T., Cotton, W., Condon, J., et al. 2020, The Astrophysical Journal, 888, 61

Miniati, F., Jones, T., Kang, H., & Ryu, D. 2001, The Astrophysical Journal, 562, 233

Mo, H., Van den Bosch, F., & White, S. 2010, Galaxy formation and evolution (Cambridge University Press)

Monteiro-Oliveira, R., Soja, A., Ribeiro, A., et al. 2021, Monthly Notices of the Royal Astronomical Society, 501, 756

Murgia, M., Govoni, F., Feretti, L., & Giovannini, G. 2010, Astronomy & Astrophysics, 509, A86

Noordam, J. E. 2004, in Ground-based telescopes, Vol. 5489, International Society for Optics and Photonics, 817–825

Noordam, J. E., & Smirnov, O. M. 2010, Astronomy & Astrophysics, 524, A61

Nunhokee, C., Bernardi, G., Manti, S., et al. 2021, arXiv preprint arXiv:2102.02900

Offringa, A. 2010, Astrophysics Source Code Library, ascl

Offringa, A., De Bruyn, A., Biehl, M., et al. 2010, Monthly Notices of the Royal Astronomical Society, 405, 155

Offringa, A., & Smirnov, O. 2017, Monthly Notices of the Royal Astronomical Society, 471, 301

Offringa, A., Van De Gronde, J., & Roerdink, J. 2012, Astronomy & astrophysics, 539, A95

Offringa, A., McKinley, B., Hurley-Walker, N., et al. 2014, Monthly Notices of the Royal Astronomical Society, 444, 606

Ogrean, G., Brüggen, M., van Weeren, R., Burgmeier, A., & Simionescu, A. 2014, Monthly Notices of the Royal Astronomical Society, 443, 2463

Pankonin, V., & Price, R. M. 1981, IEEE Transactions on Electromagnetic Compatibility, 308

Parekh, V., Van Der Heyden, K., Ferrari, C., Angus, G., & Holwerda, B. 2015, Astronomy & Astrophysics, 575, A127

Parekh, V., Thorat, K., Kale, R., et al. 2020, arXiv preprint arXiv:2009.02724

Parekh, V., Kincaid, R., Thorat, K., et al. 2021, arXiv preprint arXiv:2110.07713

Pearson, T., & Readhead, A. 1984, Annual review of astronomy and astrophysics, 22, 97

Peebles, P. J. E. 1980, The large-scale structure of the universe, Vol. 98 (Princeton university press)

Perley, R. A., & Butler, B. J. 2017, The Astrophysical Journal Supplement Series, 230, 7

Perley, R. A., Schwab, F. R., & Bridle, A. H. 1989, Synthesis imaging in radio astronomy: a collection of lectures from the third NRAO synthesis imaging summer school, Vol. 6

Petrosian, V. 2001, The Astrophysical Journal, 557, 560

Ramatsoku, M., Murgia, M., Vacca, V., et al. 2020, Astronomy & Astrophysics, 636, L1

Rau, U., Bhatnagar, S., Voronkov, M. A., & Cornwell, T. J. 2009, Proceedings of the IEEE, 97, 1472

Rau, U., & Cornwell, T. J. 2011, Astronomy & Astrophysics, 532, A71

Raychaudhury, S., T. R. F., et al. 2009

Roettiger, K., Burns, J. O., & Stone, J. M. 1999a, The Astrophysical Journal, 518, 603

Roettiger, K., Stone, J. M., & Burns, J. O. 1999b, The Astrophysical Journal, 518, 594

Ryu, D., Kang, H., Hallman, E., & Jones, T. 2003, The Astrophysical Journal, 593, 599

Sarazin, C. L. 1986, Reviews of Modern Physics, 58, 1

—. 2002, in Merging Processes in Galaxy Clusters (Springer), 1–38

—. 2003, Physics of Plasmas, 10, 1992

Scaife, A. M., & Heald, G. H. 2012, Monthly Notices of the Royal Astronomical Society: Letters, 423, L30

Schwab, F. 1984, The Astronomical Journal, 89, 1076

Selina, R. J., Murphy, E. J., McKinnon, M., et al. 2018, in Ground-based and Airborne Telescopes VII, Vol. 10700, International Society for Optics and Photonics, 107001O

Shapley, H., & Ames, A. 1930, Harvard College Observatory Bulletin, 880, 1

Shimwell, T., Röttgering, H., Best, P. N., et al. 2017, Astronomy & Astrophysics, 598, A104

Shimwell, T., Tasse, C., Hardcastle, M., et al. 2019, Astronomy & Astrophysics, 622, A1

Shimwell, T. W., Markevitch, M., Brown, S., et al. 2015, Monthly Notices of the Royal Astronomical Society, 449, 1486

Shurcliff, W. A. 2013, Polarized light: production and use (Harvard University Press)

Smirnov, O., & de Bruyn, A. 2011, in 2011 XXXth URSI General Assembly and Scientific Symposium, IEEE, 1–4

Smirnov, O., & Tasse, C. 2015, Monthly Notices of the Royal Astronomical Society, 449, 2668

Smirnov, O. M. 2011, Astronomy & Astrophysics, 527, A106

Sparke, L. S., & Gallagher III, J. S. 2007, Galaxies in the universe: an introduction (Cambridge University Press)

Springel, V., White, S. D., Jenkins, A., et al. 2005, nature, 435, 629

Swarup, G., Ananthakrishnan, S., Subrahmanya, C., et al. 1997, High-Sensitivity Radio Astronomy, 217

Tasse, C. 2014, arXiv preprint arXiv:1410.8706

Tasse, C., Hugo, B., Mirmont, M., et al. 2018, Astronomy & Astrophysics, 611, A87

Tasse, C., Shimwell, T., Hardcastle, M., et al. 2021, Astronomy & Astrophysics, 648, A1

Taylor, G. B., Carilli, C. L., & Perley, R. A. 1999, Synthesis Imaging in Radio Astronomy II, 180

Thierbach, M., Klein, U., & Wielebinski, R. 2003, Astronomy & Astrophysics, 397, 53

Thölken, S., Reiprich, T. H., Sommer, M. W., & Ota, N. 2018, Astronomy & Astrophysics, 619, A68

Thompson, A. R., Moran, J. M., & Swenson, G. J. 2004, Interferometry and Image Synthesis in Radio Astronomy

Thompson, A. R., Moran, J. M., & Swenson, G. W. 2017, Interferometry and synthesis in radio astronomy (Springer Nature)

Thompson, A. R., Moran, J. M., & Swenson Jr, G. W. 2008, Interferometry and synthesis in radio astronomy (John Wiley & Sons)

Tingay, S. J., Goeke, R., Bowman, J. D., et al. 2013, Publications of the Astronomical Society of Australia, 30

van Haarlem, M. P., Wise, M. W., Gunst, A., et al. 2013, Astronomy & astrophysics, 556, A2

van Hateren, T. 2019, PhD thesis, Universiteit van Amsterdam

van Weeren, R., de Gasperin, F., Akamatsu, H., et al. 2019, Space Science Reviews, 215, 16

van Weeren, R., Hoeft, M., Röttgering, H., et al. 2011, Astronomy & Astrophysics, 528, A38

Van Weeren, R., Röttgering, H., Brüggen, M., & Cohen, A. 2009a, Astronomy & Astrophysics, 505, 991

Van Weeren, R., Röttgering, H., Intema, H., et al. 2012, Astronomy & Astrophysics, 546, A124

Van Weeren, R., Röttgering, H., Bagchi, J., et al. 2009b, Astronomy & Astrophysics, 506, 1083

Van Weeren, R., Williams, W., Hardcastle, M., et al. 2016, The Astrophysical Journal Supplement Series, 223, 2

van Weeren, R., Shimwell, T., Botteon, A., et al. 2020, arXiv preprint arXiv:2011.02387

van Weeren, R. J. 2015, Proceedings of" The many facets of extragalactic radio surveys: towards new scientific challenges"(EXTRA-RADSUR2015). 20-23 October 2015. Bologna, 38

Van Weeren, R. J., Röttgering, H. J., Brüggen, M., & Hoeft, M. 2010, Science, 330, 347

Van Weeren, R. J., Andrade-Santos, F., Dawson, W. A., et al. 2017, Nature Astronomy, 1, 1

Venturi, T., Bardelli, S., Dallacasa, D., et al. 2017, Galaxies, 5, 16

Venturi, T., Giacintucci, S., Brunetti, G., et al. 2007, Astronomy & Astrophysics, 463, 937

Venturi, T., Giacintucci, S., Dallacasa, D., et al. 2008, Astronomy & Astrophysics, 484, 327

Venturi, T., Giacintucci, S., Merluzzi, P., et al. 2022, arXiv preprint arXiv:2201.04887

Watt, M., Ponman, T., Bertram, D., et al. 1992, Monthly Notices of the Royal Astronomical Society, 258, 738

White, D., & Fabian, A. 1995, Monthly Notices of the Royal Astronomical Society, 273, 72

Ye, H. 2019, Ph. D. Thesis

Yuan, Z., Han, J., & Wen, Z. 2015, The Astrophysical Journal, 813, 77

Zhang, L., Xu, L., & Zhang, M. 2020, Publications of the Astronomical Society of the Pacific, 132, 041001

Zhang, X., Simionescu, A., Stuardi, C., et al. 2021, arXiv preprint arXiv:2110.02094

ZuHone, J., & Su, Y. 2022, arXiv preprint arXiv:2202.06712

Zwicky, F. 1937, The Astrophysical Journal, 86, 217